UC San Diego

UC San Diego Electronic Theses and Dissertations

Title

Properties of carbon overcoats and perfluoro-polyether lubricants in hard disk drives

Permalink

https://escholarship.org/uc/item/24w0q2v0

Author

Brunner, Ralf

Publication Date

2009

Peer reviewed|Thesis/dissertation

UNIVERSITY OF CALIFORNIA, SAN DIEGO

Properties of Carbon Overcoats and Perfluoro-Polyether Lubricants in Hard Disk Drives

A dissertation submitted in partial satisfaction of the
requirements for the degree
Doctor of Philosophy

in

Engineering Sciences (Mechanical Engineering)

by

Ralf Brunner

Committee in charge:

Professor Frank E. Talke, Chair
Professor Eric E. Fullerton
Professor Sungho Jin
Professor Marc A. Meyers
Professor Jack K. Wolf

2009

The Dissertation of Ralf Brunner is approved, and it is acceptable

in quality and form for publication on microfilm and electronically:

_____

_____

_____

_____

_____

Chair

University of California, San Diego

2009

Dedication

to my parents Jürgen and Christa Brunner

Table of Contents

List of Abbreviations

ABS	Air Bearing Surface	GW	Greenwood and Williamson
a-C	Amorphous Carbon	HAMR	Heat Assisted Magnetic Recording
a-DLC	Amorphous Diamond-Like Carbon		
AE	Acoustic Emission	HDD	Hard Disk Drive
AES	Auger Electron Spectroscopy	HDI	Head Disk Interface
		HGST	Hitachi Global Storage Technology
AFM	Atomic Force Microscopy		
AFC	Anti-Ferromagnetic Coupling	IBD	Ion Beam Deposition
		ID	Inner Diameter
BPI	Bits Per Inch	IMF	Inter-Molecular Forces
BPM	Bit Pattern Media	INSIC	Information Storage Industry Consortium
CAGR	Compound Annual Growth Rate		
		IR	Infrared
CCD	Charged Coupled Device	JKR	Johnson-Kendall-Roberts
CH_x	Hydrogenated Carbon	LDV	Laser Doppler Vibrometry
CN_x	Nitrogenated Carbon	LFM	Lateral Force Microscopy
CN_xH_y	Nitrogenated-Hydrogenated Amorphous Carbon	LISD	Linear Ion Source Deposition
CMRR	Center for Magnetic Recording Research	LMR	Longitudinal Magnetic Recording
COC	Carbon Overcoats	MD	Middle Diameter
CSS	Contact Start Stop	MD	Mauguis-Dugdale
DLC	Diamond-Like Carbon	MFM	Magnetic Force Microscopy
DMT	Derjaguin-Müller-Toporov		
DTR	Discrete Track Recording	MIG	Metal in Gap
EMF	Electrostatic Force Microscopy	MR	Magneto Resistive
		MSD	Magnetron Sputtering Deposition
F-DLC	Fluorinated Diamond-Like Carbon		
		MW	Molecular Weight
FH	Flying Height	NMR	Nuclear Magnetic Resonance
GMR	Giant Magneto Resistive		

OD	Outer Diameter		RH	Relative Humidity
PDA	Personal Digital Assistant		Rms	Root Mean Square
PDI	Polydispersity Index		RPM	Revolutions Per Minute
PIID	Plasma Immersion Ion Deposition		SATA	Serial Advanced Technology Attachment
PECVD	Plasma Enhanced Chemical Vapor Deposition		SNR	Signal to Noise Ratio
PFPE	Per-Fluoro Poly-Ether		SRA	Scanning Reflectance Analyzer
PLD	Pulsed Laser Deposition		SUL	Soft-magnetic Under Layer
PMR	Perpendicular Magnetic Recording		ta-C	Tetrahedral-Amorphous Carbon
PZT	Piezoelectric Transducer		TFC	Thermal Flying-height Control
R_{SK}	Skewness		TMR	Tunneling Magneto Resistive
R_{KU}	Kurtosis			
Ra	Roughness Average		VCM	Voice Coil Motor
RAMAC	Random Access Method of Accounting and Control		XPS	X-ray Photoelectron Spectroscopy
RF	Radio Frequency			

List of Symbols

p	Pressure	M_s	Saturation magnetization
d	Spacing	V	Grain volume
μ	Air Viscosity	k_B	Boltzman's constant
U	Slider velocity in x direction		$(k_B = 1.38\mathrm{E}^{-23}\mathrm{J/K})$
V	Slider velocity in y direction	T	Temperature
t	Time	ΔFH	Flying height loss
K_n	Knudsen number	d_g	Groove depth
λ	Mean free path	w_g	Groove width
d_0	Minimum fluid film thickness	p_g	Groove pitch
E	Read-back signal	H_C	Coercivity
$\bar{x}$	Distance	(T_C)	Curie temperature
C	Material constant related to the head/disk interface	ϕ	Workfunction
k	Wave number of the write pattern	E_b	Binding energy
d_m	Magnetic spacing	E_{kin}	Kinetic energy
δ	Thickness of magnetic medium	A, B	Hamaker constants
g	Gap length between the poles	ε_i	Permittivity of material i
λ_x	Wavelength along the down-track direction x	n_i	Refractive index of material i
λ_y	Wavelength along the cross-track direction y	ν_e	Ionization frequency
b	Bit length	h	Planck's constant
w_{read}	Read width of the head	$z(x)$	Profile value of the roughness profile
D	Diameter of a magnetic grain	L	Profile length
σ	Normalized grain size distribution width	z_{mean}	Mean value of the profile
a	Transition parameter	N	Number of peaks
K_u	Magnetic anisotropy	R_{SK}	Skewness
		R_{KU}	Kurtosis

ω	Interference	ρ	Lubricant density
a	Contact radius	$\Pi(h)$	Disjoining pressure
R	Radius of the sphere	h	Lubricant film thickness
N	Normal load	γ_{SG}	Free energy of the surface
E^*	Reduced Young's modulus	γ_{SL}	Solid-liquid interfacial energy
υ	Poisson's ratio	γ_{LG}	Free surface energy of the reference liquid
W_{adh}	Work of Adhesion		
H	Hardness	θ_C	Contact angle
$A(h_c)$	Indentation area	γ^p	Dispersive component of surface energy
ψ_P	Plasticity index		
R_{cond}	Condensation mass flux	γ^p	Polar component of surface energy
P_0	Bulk vapor pressure		
M_n	Molecular weight of the PFPE	G	Gibbs free energy
R	Gas constant		

List of Figures

List of Tables

Acknowledgements

I have to thank a lot of people who contributed to my accademic work in many different ways during my years at the CMRR and helped me to achieve my goal of becoming a PhD in mechanical engineering. I would like to express my highest appreciation towards my advisor Professor Frank E. Talke. Without his advice and support this dissertation would not have been possible. He always formed a balanced environment for my research throughout my graduate student career and helped tirelessly on research papers and presentations. Throughout my studies his expertise in the field of hard disk drives was of great help. Through him, I had the great opportunity to interact with industry partners that influenced my research path.

I would like to thank the members of Prof. Talke's group, current and former, who helped me throughout my graduate studies and contributed to a wonderful work environment. In particular, I would like to thank Izhak Etsion from the Technion in Haifa, Israel for his support in my research and on several papers. In addition, I am grateful for my colleagues at the Talklab, Drs. Bart Raeymaekers, Mike Duwensee, John Xu, Andrey Ovcharenko, Melanie Gauvin and the current Ph.D. students Hao Zheng, Paul Yoon and Uwe Boettcher.

I am grateful to my co-workers from my summer internships at Hysitron Inc. and Samsung Information Systems America Inc.. I would like to thank Dr. Oden Warren, Mr. Thomas Wyrobek, Mr. Lance Kuhn, and Mr. Michael G. Berg for their support at Hysitron Inc.. I like to thank my collegues from Samsung Information

Systems America Inc., Dr. George W. Tyndall (now Western Digital Corp.), who has been very important in helping me at every stage of my Ph.D., as well as Drs. Andrey Khurshudov (now Seagate Technology), Brian Strom (now Apple Inc.), Mike Sullivan (now Western Digital Corp.), and Mike Suk. In addition, my regards go to Mr. Robert Waltman from Hitachi GST and Drs. Judy Lin and Shoji Suzuki from Western Digital for their support.

This is a great opportunity to express my respect to the CMRR staff and students that helped me in technical discussions and supported me in every possible way. I would like to especially mention my gratitude to Marcia Levitt, Betty Manoulian, Iris Villanueva, Ray Descoteaux, and all the current and former members of the CMRR.

Acknowledgement for published work:

The text of chapter 5 is a partial reprint of material as it appears in: "Long time spreading of a micro-droplet on a smooth solid surface", by Ralf Brunner, Izhak Etsion, and Frank E. Talke, submitted for publication to Langmuir (2009).

The dissertation author was the primary researcher and author and the co-authors listed in this publication directed and supervised the research which forms the basis for chapter 5.

The text of chapter 6 is a partial reprint of material as it appears in: "Adhesion between surfaces separated by molecularly-thin perfluoropolyether films", by R.

Brunner, G.W. Tyndall, R.J. Waltman, F.E. Talke, submitted for publication to Tribology Letters (2009).

The dissertation author was the primary researcher and author and the co-authors listed in this publication directed and supervised the research which forms the basis for chapter 6.

The text of chapter 7 is a partial reprint of material as it appears in: "A simple AFM calibration method for direct measurement of surface energy on nano-structured surfaces covered with molecularly-thin liquid films", by Ralf Brunner, Izhak Etsion, and Frank E. Talke, in Review of Scientific Instruments, 80(5) 055109 (2009).

The dissertation author was the primary researcher and author and the co-authors listed in this publication directed and supervised the research which forms the basis for chapter 7.

Vita

07/2001-09/2001	Engineering Intern, EOS - Electro Optical Systems, Munich, Germany
07/2002-09/2002	Engineering Intern, BAM - Federal Institute for Materials Research and Testing, Berlin, Germany
03/2003-02/2004	Visiting student, Center for Magnetic Recording Research, University of California, San Diego, USA
08/2004	Diplom Engineer (MSc), Technical Physics, University of Ilmenau, Germany
06/2005	M.S. in Mechanical Engineering, University of California, San Diego, USA
07/2005-08/2005	Research position, Hysitron Inc., Minneapolis, Minnesota, USA
2006-present	Research and Teaching Assistant, Center for Magnetic Recording Research and Department of Mechanical and Aerospace Engineering, University of California, San Diego, USA
07/2006-09/2006	Research position, Samsung Information Systems America, San Jose, California, USA
07/2009	Ph. D., University of California, San Diego, USA

Papers and Publications

1. Y. Matsuda, Y. Yoon, R. Brunner, A. Daugela, O. L. Warren, F. E. Talke, *"Nano-hardness testing with ultrasonic excitation"*, Wear 259 (2005) 1497–1501.

2. R. Brunner, I. Etsion, F.E. Talke, *"A simple AFM calibration method for direct measurement of surface energy on nano-structured surfaces covered with molecularly-thin liquid films"*, Rev. Sci. Instrum. 80 (2009) 055109.

3. A.Y.M. Lin, R. Brunner, P.Y. Chen, F.E. Talke, M.A. Meyers, "*The Abalone Foot, Underwater Adhesion through van der Waals and Capillary Forces*" Acta Materialia, online (2009).

4. R. Brunner, I. Etsion, F.E. Talke, "*Long time spreading of a pico-droplet on a smooth solid surface*", in preparation.

5. R. Brunner, G.W. Tyndall, R.J. Waltman, F.E. Talke, *"Adhesion between surfaces separated by molecularly-thin perfluoropolyether films"*, in preparation.

6. R. Brunner, A. Khurshudov, G. W. Tyndall, F. E. Talke, *"Spectroscopic and mechanical characterization of Ultra-Thin Carbon Overcoats in Magnetic Recording Disks and Sliders"*, in preparation

7. R. Brunner, R.J. Waltman, F.E. Talke, *"Meniscus between surfaces separated by molecularly-thin perfluoropolyether films"*, in preparation

ABSTRACT OF THE DISSERTATION

Properties of Carbon Overcoats and Perfluoro-Polyether Lubricants in Hard Disk Drives

by

Ralf Brunner

Doctor of Philosophy in Engineering Sciences (Mechanical Engineering)

University of California, San Diego, 2009

Professor Frank E. Talke, Chair

The interaction of lubricant with the carbon overcoats of magnetic hard disks was studied experimentally and analytically. The spreading behavior of lubricants on a disk was investigated and a theoretical model for the final film thickness of molecularly thin films was developed using volume conservation and principle of minimum energy. The adhesion and friction of surfaces separated by a molecularly-thin liquid film was studied and the relationship between friction and surface energy of lubricated surfaces was investigated. The experimental results indicate that the adhesive and frictional forces between macroscopic bodies separated by molecularly-thin liquid films are linearly proportional to the excess surface energy of the film.

An AFM calibration method for a direct measurement of surface energy on nanostructures covered with molecularly thin liquid films is proposed using the relationship between surface energy and adhesion. Surface energy measurements on the nano-structure of discrete track recording media were performed. Differences in surface energy between the groove and land area were found and explained by changes in carbon overcoat and lubricant film thickness.

1 Introduction

1.1 Hard Disk Drive Evolution

In 1956, the IBM Random Access Method of Accounting and Control (RAMAC) was presented as the first magnetic hard disk drive [1], [2]. Figure 1.1 shows an image of the RAMAC. The hard disk drive consisted of fifty 610 mm (24 inch) aluminum disks coated with an epoxy phenolic resin comprising iron oxide as the magnetic material to provide the capacity to store 5 Mbyte. The data rate of the RAMAC was 12.5 kbit/s and the data storage density was 2 kbit/inch^2. The flying height of the slider with implemented read/write element above the disk was about 25 μm. The slider and its read/write element had to be able to record or retrieve data that was spread over 240 square feet of surface area in less than a second. The first computer designed around the RAMAC 350 disk drive was called the RAMAC 305 system [3].

In the past, hard disk drives (HDD) were used for special applications such as accounting, supercomputing and military operations. Today, HDDs are utilized in a multitude of applications in a wide range of consumer electronics. The hard disk drive industry sells over 450 million drives each year. In 2009, HDDs are sold for less than $100 with a capacity of one terabyte (10^6 megabyte!!!).
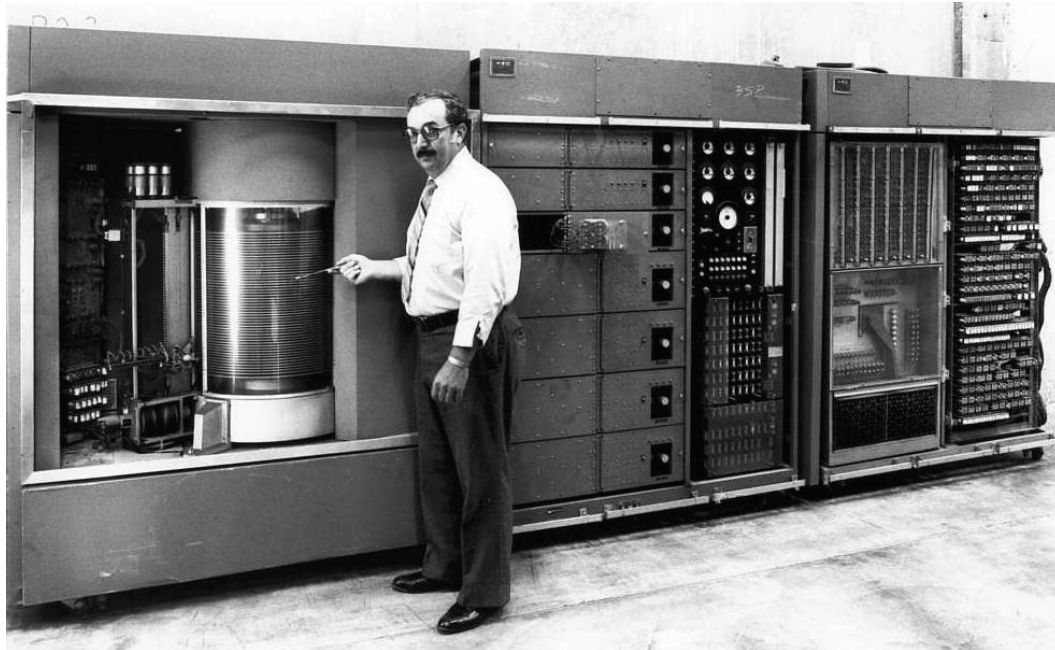
Figure 1.1: The first disk drive and the first computer: Random Access Method of

Accounting and Control (RAMAC) (Source: IBM archive)

Hard disk drives come in different form factors, depending on their application. As shown in Figure 1.1, the RAMAC 350 filled an entire room. Today the most common sizes for HDDs are 3.5 inch (88.9 mm) diameter drives for desktop computers and 2.5 inch (63.5 mm) diameter drives for laptop computers. In addition, smaller form factors such as 1.8 inch (45.7 mm) or 1 inch (25.4 mm) hard drives are utilized in MP3 players, iPods™ , personal digital assistants (PDA), digital cameras, camcorders and navigation systems, to mention a few. However, these smaller form factor drives experience fierce competition from solid state memory.

In 1965, Gordon E. Moore predicted that the number of transistors in an integrated circuit chip increases exponentially, doubling approximately every year [4]. Moore later refined the period to two years. This rate of growth has also been observed for processing speed and memory capacity. Figure 1.2 shows the evolution of data storage density of hard disk drives as a function of time [5], [6], [7]. It shows the compound annual growth rate (CAGR) of areal density over the past 53 years. The different slopes in the growth rate are based on developments in the read/write element, the magnetic layer and improvements of the head/disk interface. The continuous decrease in magnetic spacing due to thinning of the protective carbon overcoat, smoother disk surfaces and improvements in lubrication have tremendously improved the storage density of hard disk drives. Furthermore, the use of thin film heads and giant magneto resistance (GMR) read elements improved the read/write performance in hard drives [8], [9]. The magnetic media was enhanced by anti-ferromagnetic coupling (AFC) [10]. In 2006, a further increase in data storage density was provided with the change from longitudinal magnetic recording (LMR), where the magnetization in the bits is directed circumferentially along the track direction, to perpendicular magnetic recording (PMR) [11], where the magnetization of each bit points up or down perpendicular to the disk surface. Details of these developments are described in upcoming sections of this chapter.

State of the art hard disk drives consist of one to four magnetic disks and can store up to two terabyte (Tbyte) of data (1 Tbyte = 10^{12} bytes, with 1byte = 8bits). In the past 53 years, the areal density in consumer hard disk drives has increased from 2 kbit/inch^2 to over 400 Gbit/inch^2, a 200-million fold increase! In August 2008, Hitachi

Global Storage Technology demonstrated in their laboratory a recording density of about 610 Gbit/inch^2 by making several improvements to the existing magnetic recording technology [12].

hard disk drive storage density evolution
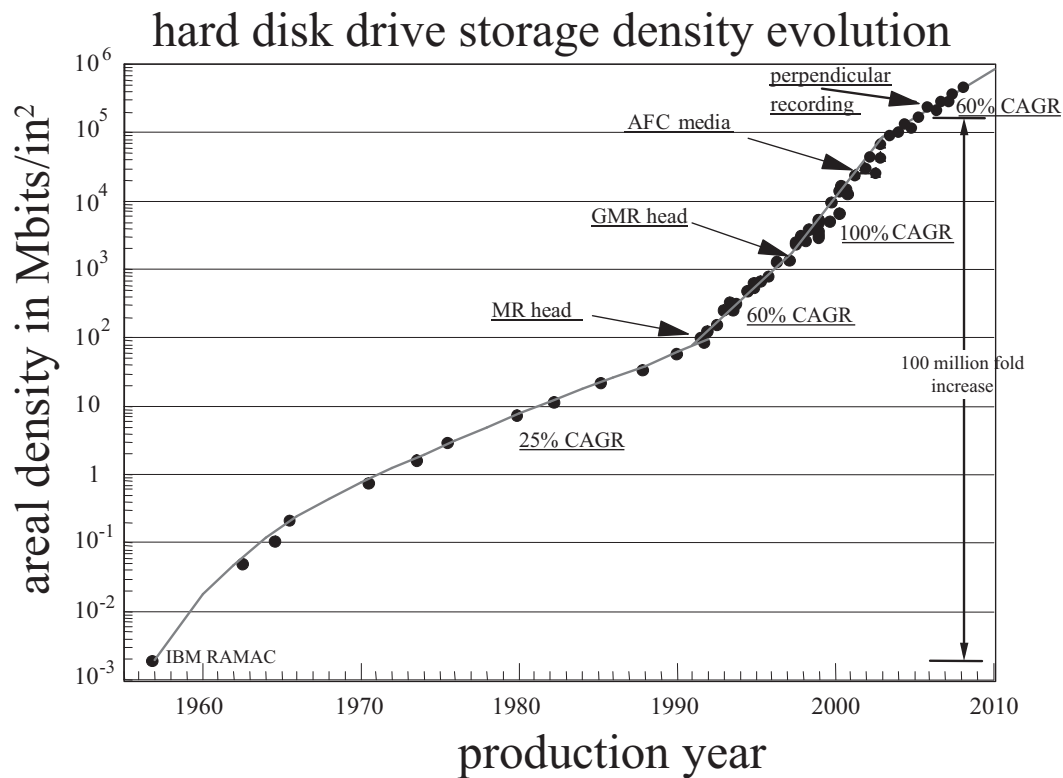
Figure 1.2: Evolution of data storage density (based on [5], [6])

1.2   Hard Disk Drive Components

Figure 1.3 shows the components of a hard disk drive. The magnetic hard disks are mounted on a spindle motor and rotate at speeds between 5,000 RPM and 15,000 RPM. The data is stored as bits on concentric tracks on a stack of one to four magnetic hard disks. The information on the disks is accessed by a read/write element positioned at the trailing edge of the slider. The slider "flies" on an air-bearing over the disk surface. It is mounted on a suspension that is attached to the voice coil motor (VCM) through the actuator arm. The voice coil motor is controlled by a servo loop and positions the slider over a specific data track. The tracks are divided into data sectors and servo sectors. The servo sectors are used for the storage of control data such as track addresses and tracking servo patterns for seek control and track following of the read/write head. The servo processor uses the position data to provide servo current command signals to control the VCM. The stator of the voice coil motor is mounted on the same base case on which the spindle is placed. The base case is enclosed with a cover and seal assembly to ensure that no external airborne contaminants can enter. An internal filtration system ensures that small wear particles and contaminants generated inside the hard disk drive are captured.

A magnification of the suspension including the slider is shown in Figure 1.4. The slider body is attached to the suspension by the gimbal spring. The slider is attached to the gimbal by an adhesion layer. The slider/gimbal assembly presses against the dimple that is stamped into the suspension as schematically shown in

Figure 1.5 [13]. The slider can move in five degrees of freedom around the dimple in the x, y, and z directions, and execute pitch, and roll motions [14], [15] .

Suspension with slider

Load/unload ramp

Voice coil actuator

Actuator arm

Base case

Magnetic hard disk

Spindle motor

Power connector

Filter

SATA interface connector
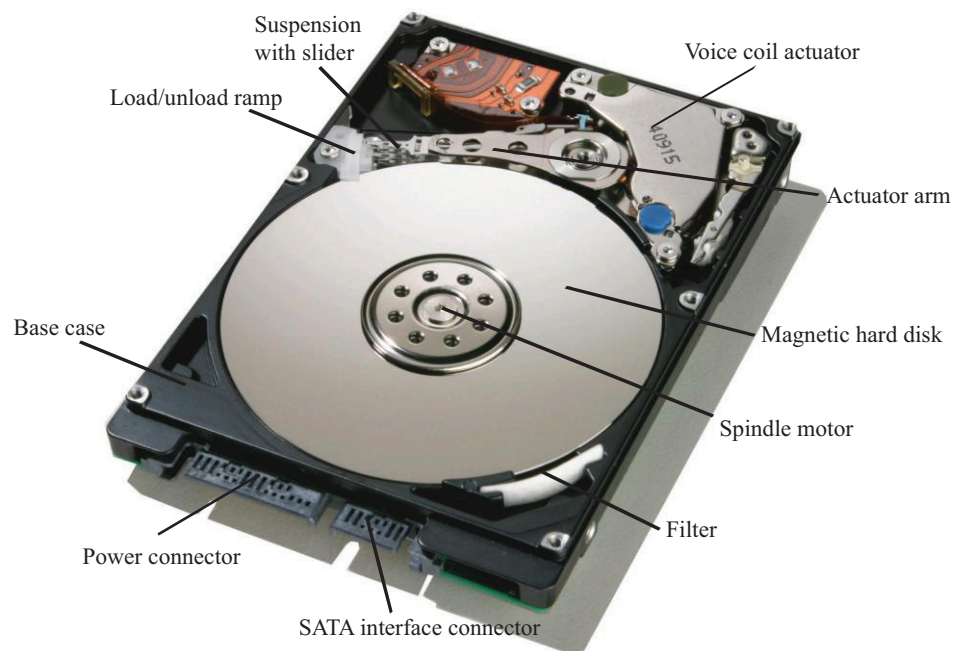
Figure 1.3: Components of a modern hard disk drive (HDD image: HGST)

The suspension positions the slider body onto the disk, and applies a preload. This preload counteracts the air bearing pressure, which is generated by the converging channel between the slider and the spinning disk. An air bearing surface (ABS) at the bottom of the slider develops high and low pressure regions for stable flying of the slider over the disk [16], [17].
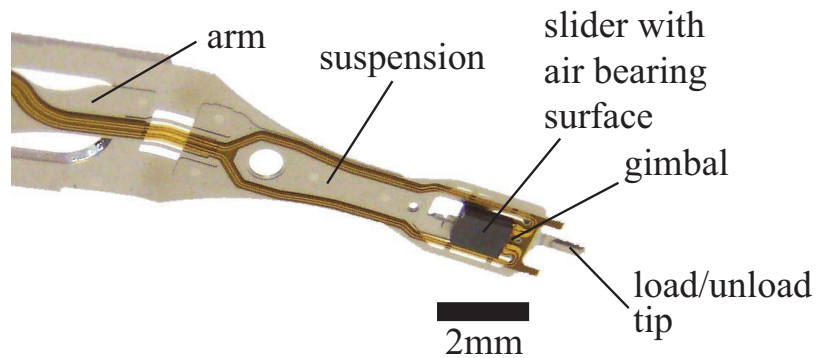
Figure 1.4: Suspension with slider

The load/unload tip lifts the suspension from the disk onto the load/unload ramp (see Figure 1.3), to prevent damage of the slider or disk caused by mechanical shocks during non-operation of the hard drive.
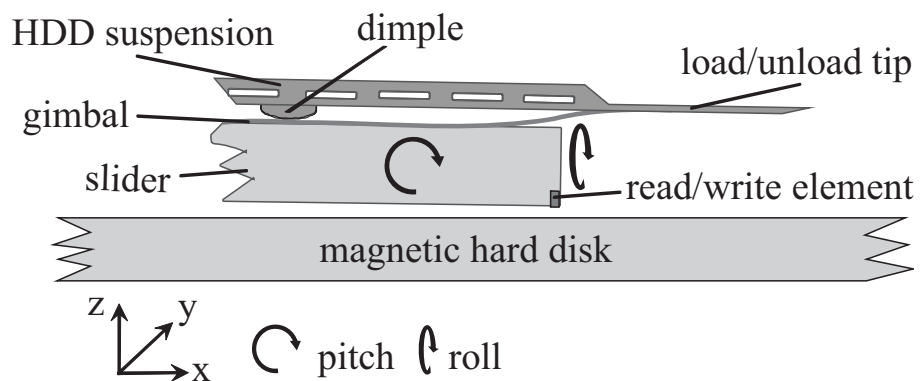
Figure 1.5: Slider/gimbal assembly

1.3   The Head/Disk Interface

One of the biggest challenges for hard disk drive manufacturer, from a tribological point of view, is to maintain a very small spacing between the read/write head and the disk [18]. State of the art disk drives operate at a head/disk separation, the so-called "flying height" of 5 nm [19], [20]. Thus, the head/disk interface is crucial for the functionality of the hard disk drive and is subject to constant improvement.

The cross section of a typical head/disk interface (HDI) is shown schematically in Figure 1.6. The disk substrate is either made of an alumina-magnesium alloy (Al_2O_3) for most desktop drives, or glass which is mostly used in laptop and mobile applications due to the higher stiffness and shock tolerance. The thickness of the substrate is between 0.4 mm and 2 mm.

After the substrates are cleaned from particles and chemical contaminants, an adhesion under-layer, which is typically a 10 μm thick film of nickel-phosphorous, is deposited on the substrate to improve the adhesion of the magnetic layer. Then, a seed layer (for example, chromium) is applied which helps to control orientation and grain size of the magnetic layer. The magnetic layer consists in general of cobalt (Co) alloys with platinum (Pt) [2], [21]. Most of these layers are deposited by sputter processes. A general schematic of the head/disk interface is shown in Figure 1.6. A protective carbon overcoat is deposited on both the magnetic disk and the slider (layer thickness of 2-3 nm) to protect against wear and corrosion [22]. Finally, the disk is coated with a thin lubricant film (1-2 nm film thickness) to reduce wear and improve

the reliability of the head/disk interface [23]. A "state of the art" magnetic disk has an average surface roughness (Ra) of nominally 0.2-0.4 nm.

The slider in a hard disk drive is typically made of alumina titanium carbide (Al_3O_2-TiC) and features the read/write head at its trailing edge [24]. The slider has an air-bearing surface (ABS) at its bottom side facing the disk surface. The air bearing surface is designed to create low and high pressure regions when the slider flies over the disk. The flying height of the slider is designed to be independent of its radial position and the spinning speed of the disk medium. The pitch angle of the slider is typically on the order of 100 mrad to create a converging channel for the pressure generation.
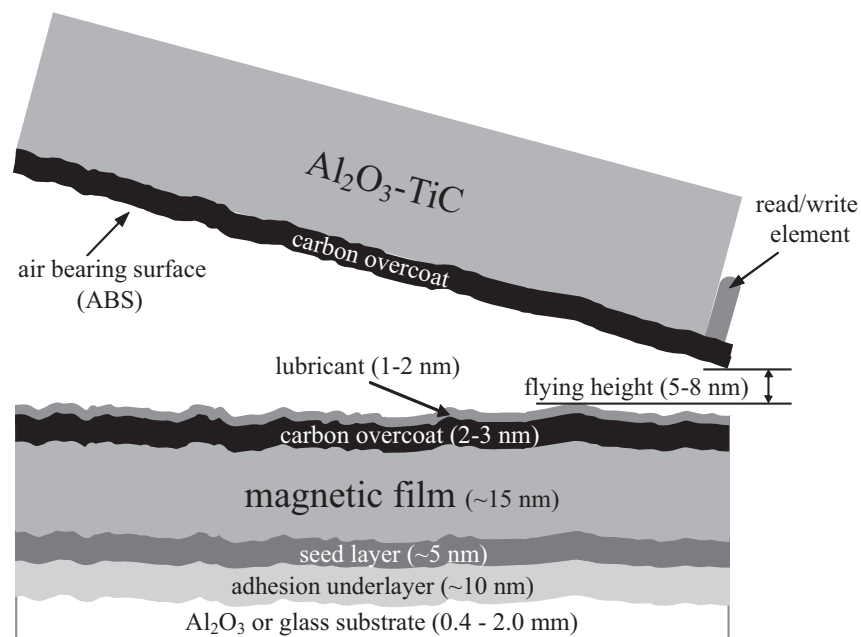
Figure 1.6: Head/disk interface in a hard disk drive

For the description of the air flow between the head and the disk, the compressible Reynolds equation [25] is commonly used. The Reynolds equation is a second order partial differential equation that is derived from the Navier-Stokes equations of motion. The two dimensional Reynolds equation for compressible gases is given as follows

$$\frac{\partial}{\partial x}\left[pd^3\frac{\partial p}{\partial x}\right]+\frac{\partial}{\partial y}\left[pd^3\frac{\partial p}{\partial y}\right]=6\mu\left(U\frac{\partial pd}{\partial x}+V\frac{\partial pd}{\partial y}\right)+12\mu\frac{\partial pd}{\partial t} \qquad (1.1)$$

It relates the pressure p, the spacing d, and other physical parameters (μ = air viscosity, U and V = slider velocities in x and y directions, t = time) to the design of a fluid bearing. The Reynolds equation balances the pressure forces (left hand side) with the viscous or shear forces (the right hand side) that are apparent in the air bearing between the disk and slider.

Due to the very low slider-disk spacing of 5-8 nm the flow cannot be treated as continuum flow and so-called rarefaction effects must be considered [26], [27]. The Knudsen number ($K_n = \lambda/d_0$), defined as the ratio of the mean free path λ of the molecules and the minimum fluid film thickness d_0, is used to determine whether rarefaction effects need to be considered in a given flow. Correction terms that depend on the Knudsen number $Q(Kn)$ have been implemented in the Reynolds equation for the air bearing in a hard disk drive, resulting in the following form of the Reynolds equation [26], [27]

$$\frac{\partial}{\partial x}\left[Q(Kn)pd^3\frac{\partial p}{\partial x}\right]+\frac{\partial}{\partial y}\left[Q(Kn)pd^3\frac{\partial p}{\partial y}\right]=6\mu\left(U\frac{\partial pd}{\partial x}+V\frac{\partial pd}{\partial y}\right)+12\mu\frac{\partial pd}{\partial t} \quad (1.2)$$

The distance between the bottom surface of the read/write element and the top surface of the magnetic layer is defined as the magnetic spacing, and equals the sum of the flying height, the carbon overcoat thickness and the thickness of the lubricant. The magnetic spacing has to be minimized to increase the data storage density. One way to achieve this is to lower the flying height. However, zero spacing is difficult to achieve since tribological problems, such as wear and stiction at the head/disk interface, will occur at this "contact recording". Hence, a small flying height of 5-8 nm is maintained between the head and the disk in "state of the art" hard disk drives.

1.4 Principle of Magnetic Recording

When a magnetic head moves relative to a magnetic medium, a magnetization pattern can be created. Digital information is coded as magnetic transitions between bits [28]. During writing, the computer sends data to the drive channel electronics in binary form (0 and 1). The data are converted into a current in the conductive coils of the write head. The current in the coil reverses direction at each 1 and remains the same at each 0 generating a magnetic field [29] between the poles. Relative motion between the write element and the rotating disk allows recording of a magnetic pattern. Figure 1.7 shows a schematic of the principle of longitudinal magnetic recording as an example.
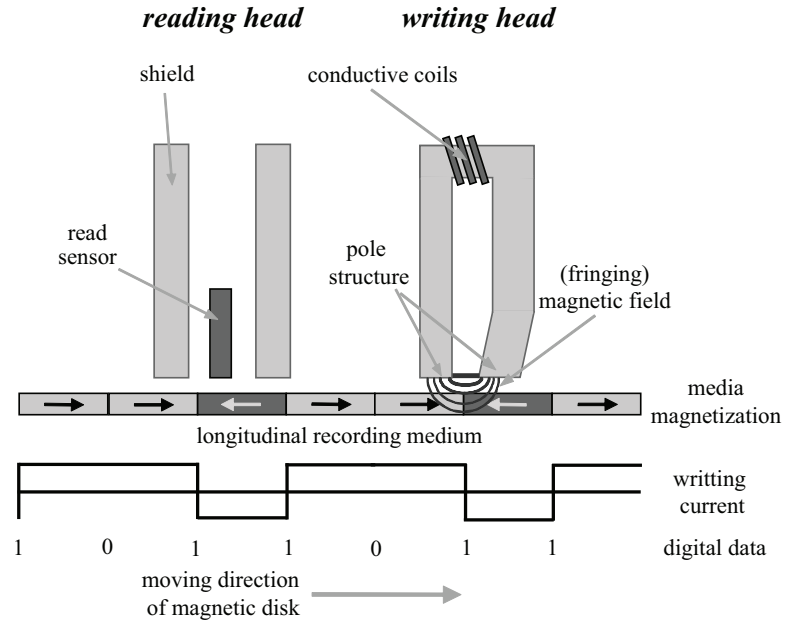
Figure 1.7: Schematic of the principal of longitudinal magnetic recording

Data is read from the disk by the read head, which detects the change in the magnetic field of adjacent bits and converts this change into an electrical signal. The electrical signal in turn is converted into binary signals that are sent to the computer for processing.

The strength of the read-back signal E for sine-wave recording is given by the Wallace equation [30]

$$E(\bar{x}) = \underbrace{Ce^{-kd_m}}_{1^{st} \text{ term}} \underbrace{\left[\frac{1-e^{k\delta}}{k\delta}\right]}_{2^{nd} \text{ term}} \underbrace{\left[\frac{\sin\dfrac{kg}{2}}{\dfrac{kg}{2}}\right]}_{3^{rd} \text{ term}} \cos k\bar{x} \qquad (1.3)$$

where

- $\bar{x}$ is the distance that the slider has moved over the disk

- C is a material constant related to the head/disk interface

- k is the wave number of the write pattern ($k = \dfrac{2\pi}{\lambda}$ with λ = wavelength)

- d_m is the magnetic spacing

- δ is the thickness of the magnetic medium

- g is the gap length between the poles of the reading head

The first term in Eq. (1.3) is the spacing loss term. The second is the loss term related to the magnetic medium thickness and the third term is related to the gap length of the recording head. It has been shown that the Wallace equation holds for both longitudinal and perpendicular magnetic recording [31]. However, Eq. (1.3) assumes that the track width is infinite. In practice, the track width of "state of the art" hard disks is very narrow and a modification of the spacing loss term in the Wallace equation can be useful [32] as follows

$$C_0(k_x, k_y)e^{-\sqrt{k_x^2+k_y^2}d} \tag{1.4}$$

where $k_x = \dfrac{2\pi}{\lambda_x}$ and $k_y = \dfrac{2\pi}{\lambda_y}$ are dependent on the wave lengths λ_x and λ_y along the down-track direction x and cross-track direction y, respectively.

The read element in a magnetic recording slider is sensitive to the vertical component of the magnetic field of the bits for both longitudinal and perpendicular

magnetic recording. The maximum vertical field is generated at the transition location by fringing fields of the magnetic media. The ideal shape for the signal amplitude is shown in Figure 1.8a). Therefore, the read-back signal for longitudinal magnetic recording resembles a pulse at the transition between bits as shown in Figure 1.8b).

In the case of perpendicular magnetic recording (PMR), the read head is sensitive to the media magnetization. The read element generates a constant read-back voltage of a given polarity. The polarity of the voltage changes when the direction of media magnetization is reversed. Hence, the read-back signal consists of a voltage step (see Figure 1.8c) and resembles a square wave for PMR media instead of a sine wave as for LMR media (see Figure 1.8b). The time derivative of a perpendicular read-back signal closely resembles waveforms obtained with a longitudinal medium, thus a signal differentiator can be utilized. The signal at the differentiator output is similar to longitudinal read-back (see Figure 1.8d) and the rest of the signal detection and processing can be adapted from standard hardware.
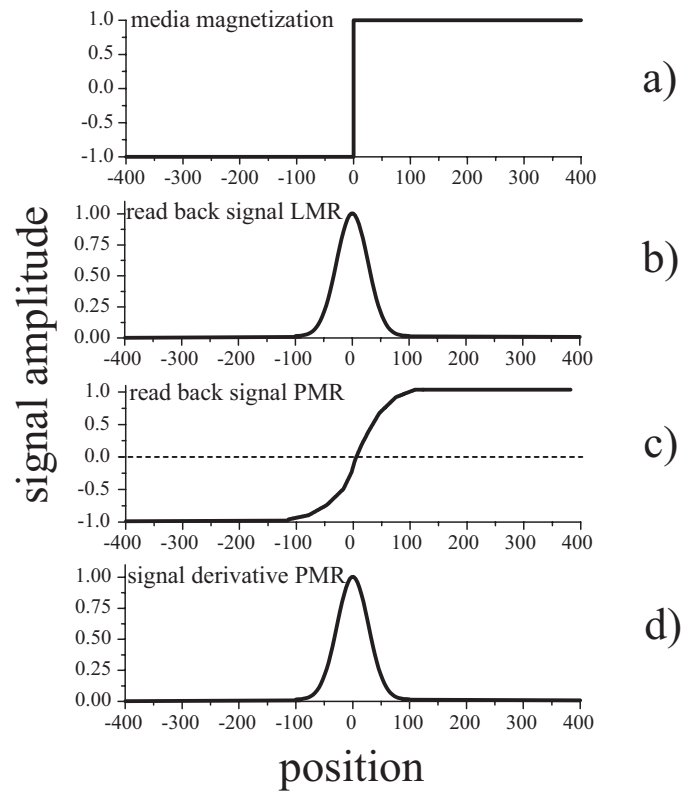
Figure 1.8: Comparison of read-back signal for longitudinal (b) and perpendicular (c)

magnetic recording media, including the signal derivative for PMR (d)

1.5   The Magnetic Medium

1.5.1   Longitudinal Magnetic Recording Media

In the past, longitudinal magnetic recording was the primary technique for magnetic storage. Improvements to magnetic materials, deposition of the materials and the tribology of the head disk interface have led to an increase in data storage density that doubled every 18 months from the early 1990s on. In the first generations

of magnetic hard disk drives, iron oxides imbedded in a binder material were spin coated onto an aluminum disk surface. This particulate medium had shortcomings since it did not have high saturation/remanent magnetization. In addition, the coercivity of these films could not be modified for high density requirements and the surface roughness was very high due to the inherent roughness of the particulate media.

In the late 1980s, thin film media were developed which provided higher saturation/remanent magnetization and higher coercivity. The surface roughness of thin film media was smaller compared to particulate media and the flying height of the slider could be substantially reduced. Several functional layers, such as adhesion and seed layers, magnetic recording layers and the carbon overcoat were sputtered on the disk substrate. The magnetic layer consisted of closely packed magnetic grains of different size with random magnetic orientations (isotropic media) in the film plane and track direction. A large number of magnetic grains were used to store a single bit of information in a magnetic domain. The magnetic domains were aligned parallel to the disk surface.

A measure of the performance of the magnetic material and how reliable bits can be detected is the signal to noise ratio (SNR), which can be estimated from [28], [33]

$$SNR \approx \frac{b^2 w_{read}}{a^2 D^3 (1+\sigma^2)} \tag{1.5}$$

where b is the bit length, w_{read} is the read width of the head, D is the diameter of a magnetic grain, σ is the normalized grain size distribution width, and a is the transition parameter. From Eq. (1.4) we see that the SNR depends inversely on the grain diameter D to the 3rd power. Therefore, reducing D is the most effective way to improve SNR. There are several ways to increase the SNR of the recording medium. Decreasing the randomness in magnetization of the grains and orienting the magnetic component in the track direction, the SNR can be increased as well. This so-called oriented media [34] yields a better SNR by over 2 dB than isotropic media. An increase of this magnitude increases the storage density by over 40%.

One way to minimize randomness in magnetization of the grains is mechanical texturing by creating circular lines on the substrate surface. Before the texturing, a nickel phosphorous layer is applied to the disk surface to increase the hardness of the alumina-magnesium substrate. Then, this smooth surface is textured with a scratch pattern to improve the magnetic orientation and enhance the magnetic film performance. In addition to the mechanical texturing, chromium (Cr) or chromium alloys are used as seed and growth layers to enhance epitaxial growth and further reduce grain size in the magnetic layer [35]. As an example, the small crystallographic difference between Cr (200) chromium crystal and the Co (110) cobalt crystal directs the growth of the cobalt film in a way that the preferred magnetic direction is parallel to the substrate [35]. This further improves longitudinal recording, and the coercivity of the magnetic film can be better controlled. Furthermore, nonmagnetic cobalt-chromium alloys can improve the lattice matching

between the seed layer and the cobalt-chromium-platinum (CoCrPt) based magnetic layer. This will increase the magnetic anisotropy (K_u) of the magnetic layer and its thermal stability. Figure 1.9 shows a schematic of the layer structure in LMR media as described above including the protective carbon overcoat and lubricant layer.
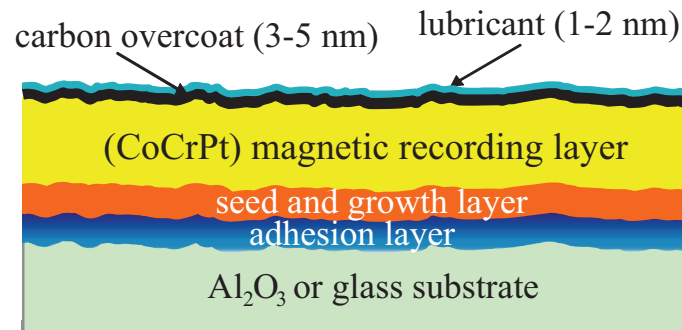
Figure 1.9: Layer structure of longitudinal magnetic recording media

The recording layer consists of grains of cobalt-platinum (CoPtX) alloys for either longitudinal or perpendicular magnetic recording (LMR, PMR) [2], [21]. In longitudinal recording the mean grain size diameter is on the order of 7nm and the thickness of the magnetic grain is approximately 10nm. An increase in recording density can be achieved by decreasing the size of the magnetic bits while maintaining the same signal to noise ratio (SNR) [33], [36]. Maintaining the SNR requires that the number of grains per bit is kept constant [37]. In high density recording the accuracy of the stored information depends on the precision of the transition and the cross-talk between two adjacent bits. Cross-talk is the phenomenon, when two adjacent bits

influence each other and cause a switch in magnetization of one of them, which in turn results in a loss of information. This cross talk can be reduced by using additives such as chromium (Cr), tantalum (Ta), and/or bromine (Br) to better separate the grains from each other and reduce the exchange coupling. The inter-granular exchange is controlled by using the additive materials as thin segregation elements in the Co-alloy matrix. However, a further reduction in grain size (below 7nm) leads to a decrease in the magnetic anisotropy energy stored in a grain and thermal energy can excite the magnetization causing reversal of the magnetization. This phenomenon is called the super paramagnetic effect.

1.5.2 The Super Paramagnetic Effect

If the ferromagnetic grains of the magnetic material on the hard disk become very small, thermal fluctuations can cause a random change in the magnetic direction of the grain. The magnetic material as a whole is not magnetized except when it is in an externally applied magnetic field (similar to paramagnetic materials). The magnetic energy stored in a grain is a factor of the magnetic anisotropy K_u and the grain volume V. In order to prevent thermal fluctuations of the magnetization of the grains, the ratio of

$$\frac{\text{magnetic energy}}{\text{thermal energy}} = \frac{\text{anisotropy} \cdot \text{volume}}{k_B \cdot \text{temperature}} = \frac{K_u V}{k_B T} \geq 60 \qquad (1.6)$$

where k_B is Boltzman's constant ($k_B = 1.38\text{E}^{-23}\text{J/K}$) and T is the temperature, has to be at a certain level. The ratio must be over 60 for longitudinal magnetic recording

[38]. Accordingly, if the volume V of the grains decreases further, the magnetic anisotropy energy K_u must increase for the grain to be thermally stable. This would require a higher magnetic writing field to switch the magnetization of the grains. Since the write field from recording heads is limited in magnitude by material properties, the diameter of thermally stable grains is limited to 7-8 nm in diameter for longitudinal recording [39], [40].

The design space of the magnetic medium is limited by thermal decay (KV too small), write ability (anisotropy field too high for writing field to switch) and an insufficient signal to noise ratio for reading the data [41], [11]. In the late 1990's, an IBM research group found that anitferromagnetically coupled (AFC) magnetic layers can be used to stabilize recorded information [42], [43]. In AFC media, the recording layer consists of two ferromagnetic layers with a magnetic orientation that is opposite to each other (anitferromagnetically coupled). The lower magnetic layer is called the stabilizing layer and the upper layer is the recording layer. In order to anitferromagnetically couple the magnetic layers, they need to be separated by a thin non-magnetic layer such as ruthenium (Ru). The thickness of the Ru layer controls the coupling stage of the magnetic layers and was found to be approximately 0.6 nm for the layers to be perfectly anitferromagnetically coupled [44]. The non-magnetic layer was later referred to as "Pixie Dust" [10]. Anti-ferromagnetic coupling pushed the super-paramagnetic effect of longitudinal magnetic recording even further; however, the writing with a fringing magnetic field and the reading using GMR heads was still a

challenge. In more recent years perpendicular magnetic recording was introduced coupled with new read/write head designs to further boost data storage density.

1.5.3   Perpendicular Magnetic Recording Media

In the case of longitudinal magnetic recording (LMR), the magnetization of the bits is in the plane of the disk as shown in Figure 1.7 [45], while in perpendicular magnetic recording (PMR) the magnetization is orthogonal to the plane of the disk (see Figure 1.11) [7]. In PMR media the magnetic bits have a higher coercivity and can be stacked closer together, which increases linear density [46].

The real difference and complexity of PMR media is the structure of the magnetic medium for perpendicular magnetic recording. It consists of a soft-magnetic under-layer (SUL) and a magnetically "hard" (high coercivity) recording layer [21]. Figure 1.10 shows a general structure of a perpendicular magnetic recording medium. The details are explained throughout this section.
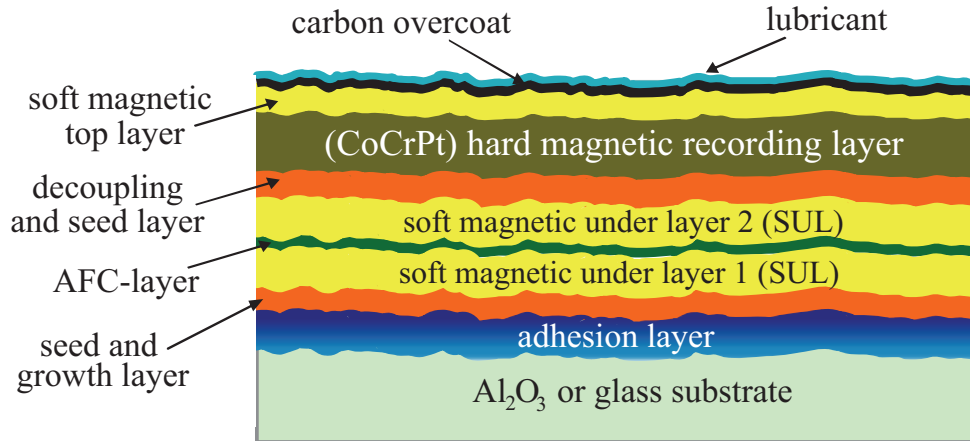
Figure 1.10: Schematic of the layer structure in a perpendicular magnetic recording medium

The recording principle is shown in Figure 1.11. The inductive write pole is aligned vertical to the surface of the disk platter as shown in Figure 1.11. The gap field of the write head, which is two times stronger compared to the weaker fringing field in longitudinal recording, is used to write the data. This is only possible due to the soft-magnetic under-layer which acts as a magnetic "mirror" and produces a "virtual image" of the poles below the recording layer (see Figure 1.11). Therefore, the recording medium is practically placed in the gap between the two poles and a stronger write field gradient can be applied that is needed to switch the high-coercivity recording layer. The returning field through the SUL back to the returning pole of the writing head is spread over a larger area.
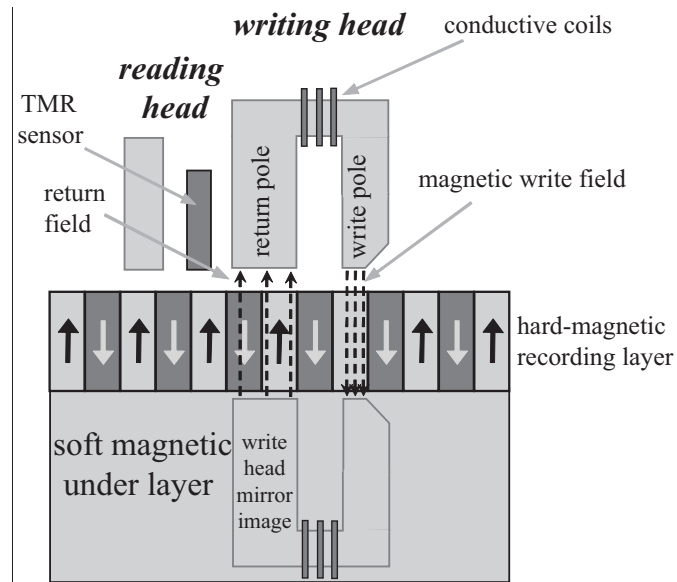
Figure 1.11: Principal for the write process in perpendicular magnetic recording (after

[7])

Therefore, the magnetic field between the SUL and the return pole is much weaker than the writing field and will not affect the magnetization of the recording layer.

Different cobalt (Co) alloys are being used for the SUL in an amorphous or crystalline state. Amorphous materials such as FeCoB, CoTaZr, or CoZrNb [41] were used in the past, which needed a thick seed layer to realign in a crystal structure for the recording layer. They have been replaced by crystalline materials such as FeCo which exhibit superior properties and crystal structure to reduce the seed layer thickness. Magnetically it is desirable that the thickness of the SUL is large enough to prevent saturation. The thickness of the SUL layer is between 50 nm and 120 nm, depending on the alloy type and crystal structure. The SUL has a magnetic direction in the circumferential direction similar to longitudinal recording. In addition, to further

increase the thermal stability and decrease the thickness, two thin SUL layers can be anti-ferromagnetically coupled by a thin ruthenium (Ru) layer to decrease the SUL thickness, which is somewhat similar to AFC in LMR media.

Another seed and growth layer is sputtered on top of the SUL to reduce the exchange interaction between the SUL and the recording layer and to increase the coercivity. In addition, the seed and growth layer induces a textured growth which aligns the magnetic orientation of the grains in perpendicular direction to the surface. This sub-layer structure greatly controls the grain size of the recording layer and provides the correct crystal orientation and a granular roughness to initiate the physical separation of the grains in the magnetic layer above. Ruthenium (Ru) alloys are used as seed and growth layer and provide a finely dispersed nucleation density with a narrow distribution in critical nuclei size [41].

The recording layer in PMR media is composed in a similar way as LMR media, except that the magnetic direction of the grains is perpendicular to the film plane. Therefore the recording layer can be designed with "tall and slim" grains which are superior for thermal stability and signal to noise ratio. PMR media shows weaker demagnetization fields for thicker layers which is also favorable, and the magnetic energy can be "stored in the depth". However, an optimum of 15-25 nm was found due to the growth process of the magnetic grains and limits of the so-called transition length [41].

Cobalt alloys such as CoCrPt, CoCrTa, and CoCrPtNb have been used as recording materials in the earlier stages of PMR media, where Cr was used as an

exchange decoupling material [41]. However, the anisotropy K_u of the alloys was not sufficient. Recently, oxide-based CoCrPt materials have been used, where Si-oxide or Cr-oxide are sputtered together with CoCrPt. During sputtering the cobalt alloy is surrounded by an oxide-based grain boundary, since both materials do not mix well with each other. Some of the Cr from the CoCrPt would oxidize as well and less Cr will be present in the grain core, which increases the anisotropy of the grain. The grains are thermally stable and the oxide grain boundary reduces exchange interactions between grains. The average grain size (pitch between grains) in current (2008) perpendicular media is on the order of 6nm. Grain sizes as small as 4nm, that are thermally stable have been reported [47].

With perpendicular magnetic recording it was possible to increase data storage density on a disk at a 40% rate for the past years. Perpendicular magnetic recording is one option to postpone the super-paramagnetic effect in magnetic recording with the possibility of breaking the 1Tbit/inch^2 barrier.

1.6 Magnetic Recording Read/Write Elements

Originally, the read/write element in hard disk drives was a small C-shaped piece of ferrite which was wrapped in a fine copper wire coil [48]. This element was used for both the read and the write process. In the beginning of the 1980's, so-called thin film heads, manufactured using semiconductor process technologies [49], enabled

a significant decrease of the slider size and an increase in storage density above 10

Mbits/inch^2. Eventually, the write element was separated from the read element.

1.6.1 The Magnetic Recording Write Element

A pole structure is used for the write element, featuring an inductive write

element and a return pole in a U-shape. Induction coils are wound around the U-piece

to induce a magnetic field between the poles, when a current flows (see Figure 1.7).

The magnetic field emerges from the inductive write pole and returns through the

return pole with a fringing field extending to the magnetic recording medium. In

longitudinal magnetic recording the fringing field is used to write the information (see

Figure 1.7). In perpendicular magnetic recording the field directly at the gap is used

for writting (see Figure 1.11). In addition, the size of the write element was

continuously decreased and a narrower pole width allowed to produce stronger

recording fields and improved magnetic flux flow [49]. In addition, the magnetic flux

density at the write pole was increased for more writing power due to changes in the

materials composition (for example, introducing FeNi and FeCo materials into the

permalloy), and reducing the coil turns around the U-piece increased the write speed.

1.6.2 Evolution of the Magnetic Recording Read Element

In most of the hard disk drives, the read sensor is located at the inside of the

read/write element, shielded by two plates to avoid misregistration by adjacent bits

(see Figure 1.7). When the read and write elements were separated, the so-called magneto resistive effect was utilized for the reading of the data. Anisotropic magneto resistance is based on the spin direction of the conduction electrons in the material, which results in low electrical resistance when it is parallel to the magnetic field and higher electrical resistance when the magnetic field has opposite polarity [28]. This effect is used in read elements since the 1990s, and allowed a large increase in storage density.

The biggest improvement in the read element design was made in the late 1980's, when Gruenberg [8] and Fert et al. [9] discovered that the resistance of certain magnetic heterostructures can vary dramatically in the presence of a changing magnetic field. This so-called giant magneto resistive (GMR) effect increased the sensitivity of the read element substantially by sensing changes in the magnetic orientation from bits of much smaller physical size. GMR elements were implemented in the late 1990s. The GMR sensor enabled an increase in areal storage density and was used at storage densities above 2 Gbits/inch^2.

Currently, tunneling magneto-resistive elements (TMR) have been implemented in hard disk drives with perpendicular magnetic recording (PMR) media. The principle of TMR sensors are similar to the GMR sensor, except that the current is flowing between two ferro-magnets which are separated by a thin insulator (for example MgO, about 1 nm thick) [50]. The total resistance of the device, in which the tunneling is responsible for current flow, changes with the relative orientation of the two magnetic layers (which is influenced by the magnetic bits). This leads to an

improved readability of PMR media. TMR elements show a higher magneto-resistance than GMR elements and are used for storage densities above 100 Gbits/inch^2 [49].

In current high-end products, integrated heater elements heat the materials around the read/write element, thus the write pole and surrounding area will protrude toward the disk surface [51], [52]. This technique is called pole-tip protrusion or thermal flying-height control (TFC), and is used to actively control the flying height of the slider. The read/write element of a TFC slider will be actuated for the read/write process and positioned at 5nm or less spacing above the disk surface [53], [54]. This improves the written magnetic transitions by ensuring that the write field of the read/write element is as close to the magnetic medium as possible.

1.7   Alternative Future Technologies for Magnetic Recording

The super paramagnetic effect, as discussed previously, poses a limit to the areal storage density. A number of techniques exist that have been proposed to overcome the present limitations to reach a storage density larger than one Tbit/inch^2 [55], [56]. To reach this goal, the pitch between two bits has to be on the order of 25 nm. Table 1.1 indicates the pitch between two bits for different storage densities.

Table 1.1: Pitch between two bits as a function of storage densities

density [Gbits/in^2]	pitch [nm]
500	36
750	29
1000	25
2500	16
5000	11

1.7.1   Patterned Media

To achieve storage densities of more than one Tbit/inch^2, discrete track recording (DTR) and bit-patterned media (BPM) have recently received substantial interest [57], [58], [59], [60], [61].   For patterned media, the magnetic bits are physically separated from each other to avoid magnetic "cross talk" (see Figure 1.12) [28], [62]. The number of grains per bit (in the case of DTR media) can be reduced by keeping the signal to noise ratio constant. In addition, the write poles of the magnetic head may be larger than the land regions on the disk resulting in a magnetic flux that is constant over the whole land region.

Figure 1.12 shows the differences between conventional, discrete track, and bit patterned media schematically [6].   Conventional media consists of a continuous granular recording layer with multiple grains per bit where the boundaries between the bits are determined by the grains.   In DTR media, patterned tracks (concentric grooves) are formed into the perpendicular magnetic recording (PMR) layer.   The magnetic information is separated physically and magnetically in cross track direction,

which eliminates track edge noise. Thus, the number of grains per bit can be reduced [57], [59].

In bit patterned media highly exchange coupled granular media is used for single domain magnetic islands. The magnetic islands are physically separated in both directions, along and cross track (see Figure 1.12). Since the transition noise is eliminated only one grain is needed for each bit of information. The media is thermally more stable since the volume V of a single bit is larger compared to the grain in conventional perpendicular recording media [63], [64]. Each island needs to be placed uniform on concentric tracks over the entire disk surface by lithographic techniques.
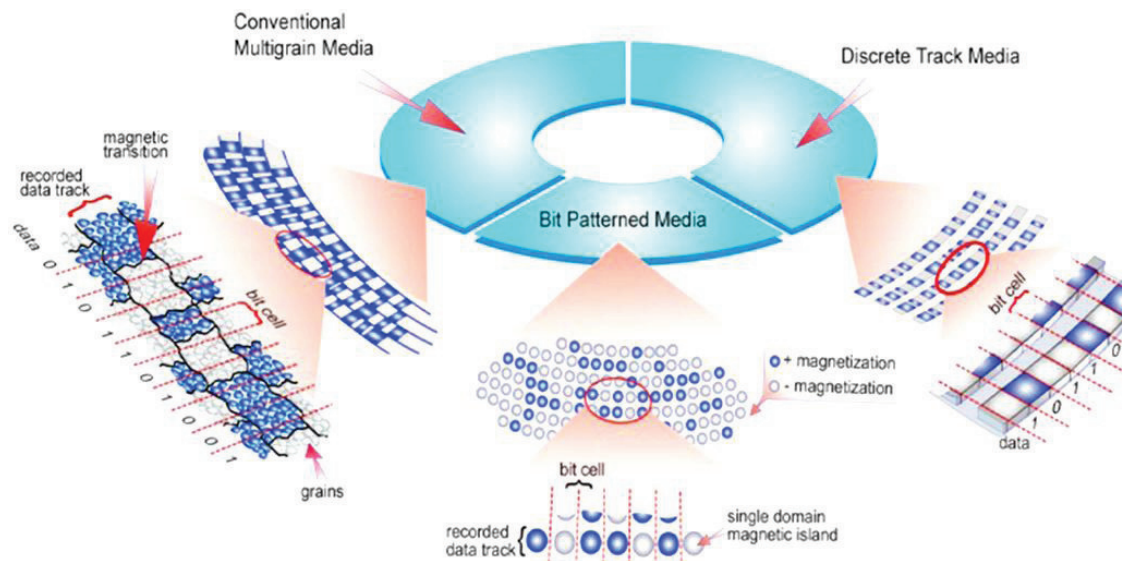
Figure 1.12: Schematic of discrete track recording and bit pattern media (Source: HGST [6])

The manufacturing process of the patterning is a big challenge and different nanofabrication methods have been proposed for patterned media [58] from different lithography techniques to self assembly patterns [64]. For 1 Tbit/inch^2, a sub-12 nm resolution of the nanofabrication process is required. There are two types to create patterns: I) a physical process, where a topographical pattern is created on a substrate and II) a chemical process, where the surface chemistry is selectively modified to grow nanostructures in some areas but not others. Many challenges exist for self assembly to be successful and give long range order for high density patterned media.

The most promising technique to produce nanostructures is lithography. In this approach, a pattern is created in a resist layer and etched into the substrate. Using different intermediate steps, one can transform the pattern onto the magnetic layer of a disk. A number of different techniques can be used to generate the pattern, such as electron beam lithography, ion beam lithography, immersion lithography and nano-imprint. Most of these lithographical technologies are very costly and to manufacture one disk takes several days; even weeks. Therefore, a master with a positive pattern of the final product can be manufactured using e-beam lithography. This master is then used for nano-imprint lithography with subsequent etching steps to produce thousands of replicas which would have a negative pattern. In turn, by duplicating the steps, a large number of replicas can produce hundreds of thousands of the final magnetic medium as shown in Figure 1.13 [65], [66]. A more detailed description of this procedure is given in Chapter 6.

Source: HGST 10,000 replica nano-imprint molds 100,000,000 disk substrates
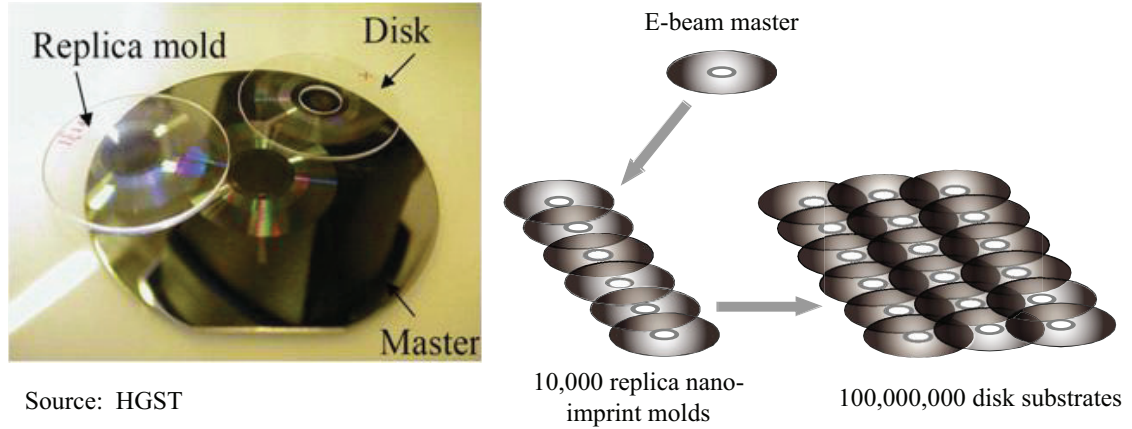
Figure 1.13: Nano-imprint replication of pattern media

Patterned media pose substantial tribological challenges for the head/disk interface. In particular, "flyability" and reliability of a hard disk drive [67] are important. The load carrying capacity of magnetic recording sliders is a function of the groove and bit parameters (see Figure 1.14). The effect of discrete tracks on the flying behavior of sliders has been investigated using a finite element based air bearing simulator [68]. An empirical equation for the flying height loss ΔFH of a slider as a function of discrete track parameters was obtained by Duwensee et al. [68]

$$\Delta FH = d_g \frac{w_g}{p_g} \tag{1.7}$$

where d_g is the groove depth, w_g is the groove width, and p_g is the groove pitch (see Figure 1.14). For flying heights on the order of several nanometers, variations in the depth and width of the grooves will affect the dynamic flying characteristics of the slider.
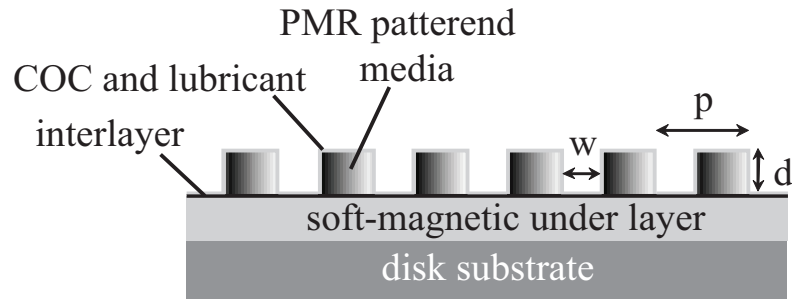
Figure 1.14: Schematic of a cross section of DTR media, describing the parameters
and materials of the discrete track.

Intermolecular forces between the slider and the land areas of discrete track
media become increasingly more important with a reduction in flying height and must
be considered in the design of the head/disk interface and the air bearing surface of the
slider. Furthermore, lubricant spreading, surface energy variations [69] and corrosion
of the media are of great concern [70]. This will be discussed in more detail in
Chapter 6.

1.7.2   Heat Assisted Magnetic Recording

Heat assisted magnetic recording (HAMR) is a recording technique that uses
the effect that magnetic properties such as magnetic anisotropy (K_u), and coercivity
(H_C) decrease at elevated temperatures (Curie temperature (T_C) of the magnetic
materials) to a value close to zero. A laser beam is heating the media to an elevated

temperature where the coercivity (H_c) of the magnetic bits is below the writing field of the head in order to write the data [71], [72], [73]. After the writing field is applied, the heated region is rapidly cooled down to ambient temperature and the magnetic information is "frozen" into the magnetic material. High coercivity magnetic materials can store single bits at a much smaller size with a sufficient signal to noise ratio, and therefore, are less limited by the super-paramagnetic effect. It has been predicted that bit-patterned media coupled with heat assisted magnetic recording can enable recording densities far above 1Tbit/inch^2 [74].
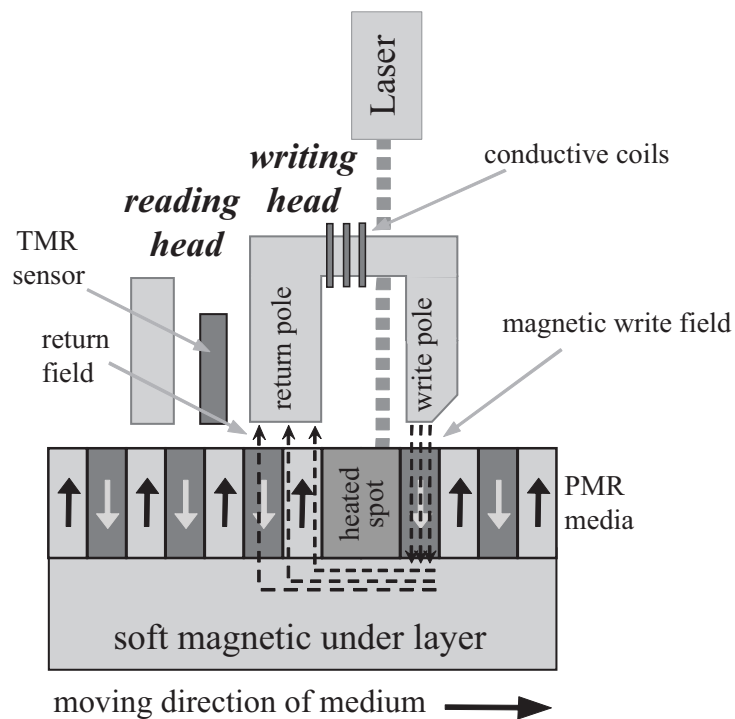
Figure 1.15: Schematic of heat assisted magnetic recording (HAMR)

There are several technical challenges with heat assisted magnetic recording, including the development of new high coercivity media with small grain size and correct thermal properties. On the read/write head side, an optical waveguide and near field source for coupling the laser light has to be implemented in the design. Thermal timing and side writing on neighboring bits and the power dissipation and thermal management has to be optimized.

1.8   Organization of the Dissertation

This dissertation focuses on the tribology of the head/disk interface and investigates the characteristics of the carbon overcoat and lubricant system on the disk.

Chapter 1 gives an introduction into magnetic recording and discusses mechanical components of a typical hard disk drive. The head/disk interface and the principle of magnetic recording are described, and recent and future trends in hard disk drive technology are discussed.

Chapter 2 provides an overview of wear and corrosion protective materials in hard disk drives. Different deposition and analysis methods are described and future perspectives are given.

Chapter 3 discusses different lubricants and additives used in hard disks. The interaction between the carbon overcoat and the lubricant are described. In addition, surface energy and disjoining pressure of the lubricated disk surface is discussed.

In Chapter 4, structural and mechanical properties for carbon overcoats of commercially available hard disks and sliders were evaluated using Raman spectroscopy, X-ray photoelectron spectroscopy, AFM roughness measurement, nano-indentation and scratch testing.

Chapter 5 focuses on lubricant spreading on a smooth solid surface. The long time spreading of micro-droplets was studied experimentally and an empirical expression is provided for the spreading area as a function of time. A theoretical model was developed to predict the uniform film thickness of the spreading droplet based on volume conservation and the principle of minimum energy.

Chapter 6 investigates the relationship between surface energy and adhesion as well as friction of surfaces separated by a molecularly-thin liquid film.

Chapter 7 describes a calibration method for the determination of surface energy on nano-structured surfaces covered with sub-monolayer liquid films by atomic force microscopy (AFM) pull-off force measurements using the correlation found in Chapter 6. The method avoids the need for complex calibration of the atomic force microscope and the indirect correlation with various adhesion models.

Chapter 8 gives the conclusions of this dissertation.

Bibliography

[1] T. Noyes and W.E. Dickinson, "The magnetic disk, random access memory," presented at the Western Joint Computer Conf., 1956.

[2] A.S. Hoagland, "History of magnetic disk storage based on perpendicular magnetic recording," IEEE Transaction on Magnetics, vol. 39, no. 4, pp. 1871-1875, 2003.

[3] http://www.magneticdiskheritagecenter.org/MDHC/RAMACBrochure.pdf.

[4] G.E. Moore, "Cramming more components onto integrated circuits," Electronics, vol. 38, no. 8, 1965.

[5] "http://www.insic.org/,".

[6] "http://www.hitachigst.com".

[7] D.A. Thompson and J.S. Best, "The future of magnetic data storage technology," *IBM J. Res. Develop.*, vol. 44, no. 3, pp. 311-322, 2000.

[8] P. Gruenberg, "Magnetic field sensor with ferromagnetic thin layers having magnetically antiparallel components," 4,949,039, 1990.

[9] M.N. Baibich et al., "Giant magnetoresistance of (001)Fe/(001)Cr magnetic superlattices," *Phys. Rev. Lett.*, vol. 61, pp. 2472-2475, 1988.

[10] E.E. Fullerton et al., "Antiferromagnetically coupled magnetic media layers for thermally stable high density recording," *Appl. Phys. Lett.*, vol. 77, no. 23, pp. 3806-3808, 2000.

[11] H.N. Bertram and M. Williams, "SNR and density estimates: A comparison of longitudinal and perpendicular recording," *IEEE Trans. Magn.*, vol. 36, no. 1, pp. 4-9, 2000.

[12] "http://techon.nikkeibp.co.jp/english/NEWS_EN/20080804/155945/,".

[13] W. Hua, B. Liu, G. Sheng, and J. Li, "Further studies of unload process with a 9D model," *IEEE Trans. Magn.*, vol. 37, no. 4, pp. 1855-1858, 2001.

[14] H. Kohira, H. Tanaka, M. Matsumoto, and F.E. Talke, "Investigation of slider vibrations due to contact with a smooth disk surface," *J. Tribol.*, vol. 123, pp. 616-623, 2001.

[15] J. Xu, J.D. Kiely, Y.-T. Hsia, and F.E. Talke, "Dynamics of ultra low flying sliders during contact with a lubricated disk," *Microsyst. Technol.*, vol. 13, pp.

1371-1375, 2007.

[16] Q.-H. Zeng and D.B. Bogy, "Effects of certain design parameters on load/unload performance," *IEEE*, vol. 36, no. 1, pp. 140-147, 2000.

[17] B. Liu et al., "Air-bearing design towards highly stable head-disk interface at ultralow flying height," *IEEE Trans. Magn.*, vol. 43, no. 2, pp. 715-720, 2007.

[18] F.E. Talke, "On tribological problems in magnetic disk recording technology," *Wear*, vol. 190, pp. 232-238, 1995.

[19] R.W. Wood, "The feasibility of magnetic recording at 1 terabit per square inch," *IEEE Trans. Magn.*, vol. 36, pp. 36-42, 2000.

[20] R.W. Wood, J. Miles, and T. Olsen, "Recording technologies for terabit per square inch systems," *IEEE Trans. Magn.*, vol. 38, pp. 1711-1718, 2002.

[21] R.H. Victora and X. Shen, "Composite media for perpendicular magnetic recording," *IEEE Trans. Magn.*, vol. 41, no. 2, pp. 537-542, 2005.

[22] T. Liew, R. Ji, C.H. Seek, and T.C. Chong, "Corrosion of magnetic recording heads and media," *Tribology international*, vol. 36, no. 4-6, pp. 447-454, 2003.

[23] A. Khurshudov and R.J. Waltman, "Tribology challenges of modem magnetic hard disk drives," *Wear*, vol. 251, pp. 1124-1132, 2001.

[24] A.R. Machcha, T.C. McMillan, F.E. Talke, and W.T. Tang, "Tribology of tri-pad sliders," *Tribol. Trans.*, vol. 40, no. 1, pp. 120-128, 1997.

[25] O. Reynolds, *An experimental investigation of the circumstances which determine whether the motion of water shall be direct or sinuous: And of the law of resistance in parallel channels.*: Royal Society of London, 1883.

[26] S. Fukui and R. Kaneko, "Analysis of flying characteristics of magnetic heads with ultra-thin spacings based on the boltzmann equation," *IEEE Trans. Magn.*, vol. 24, no. 6, pp. 2751-2753, 1988.

[27] S. Fukui and R. Kaneko, "Analysis of ultra-thin gas film lubrication based on linearized Boltzmann equation: First report-derivation of a generalized lubrication equation including thermal creep flow," *ASME J. Tribol.*, vol. 110, pp. 253-262, 1988.

[28] H.N. Bertram, *Theory of magnetic recording*. Cambridge: Cambridge University Press, 1994.

[29] "http://www.dataclinic.co.uk/data-recovery/hard-disk-functionality.htm,".

[30] R.L. Wallace, "The reproduction of magnetically recorded signals," *Bell Syst. Tech. J.*, vol. 30, p. 1145, 1951.

[31] S. Gebredingle, S. Gider, and R. Wood, "The magnetic spacing sensitivity of perpendicular recording," *IEEE Trans. Magn.*, vol. 42, no. 10, pp. 2273-2275, 2006.

[32] Y. Tang, S.-Y. Hong, N.-Y. Kim, and X. Che, "Overview of fly height control applications in perpendicular magnetic recording," *IEEE Trans. Magn.*, vol. 43, no. 2, pp. 709-714, 2007.

[33] H.N. Bertram, H. Zhou, and R. Gustafson, "Signal to noise ratio scaling and density limit estimates in longitudinal magnetic recording," *IEEE Trans. Magn.*, vol. 34, no. 4, pp. 1845-1847, 1998.

[34] M. Walker, "Performance media: Tweaking magnetic capabilities," *Techn. Paper. Seagate*, vol. TP-577, 2001.

[35] S. Katayama, T. Tsuno, K. Enjoji, N. Ishii, and K. Sono, "Magnetic properties and read-write characteristics of multilayer films on a glass substrate," *IEEE Trans. Magn.*, vol. 24, no. 6, pp. 2982-2984, 1988.

[36] R.L. White, R.M.H. New, R. Fabian, and W. Pease, "Patterned media: A viable route to 50 Gbit/in(2) and up for magnetic recording?," *IEEE Trans. Magn.*, vol. 3, no. 1, pp. 990-995, 1997.

[37] A. Moser et al., "Magnetic recording: advancing into the future," *J. Phys. D: Appl. Phys.*, vol. 35, pp. 157-167, 2002.

[38] D. Weller and A. Moser, "Thermal effect limits in ultrahigh-density magnetic recording," *IEEE Trans. Magn.*, vol. 35, no. 6, pp. 4423-4439, 1999.

[39] A. Moser and D Weller, "Thermal effects in high-density recording media," in *The physics of ultra-high density magnetic recording*. Berlin, Heidelberg, New York: Springer, 2001, pp. 144-174.

[40] S. Batra, J. Hannay, H. Zhou, and J. Goldberg, "Investigations of perpendicular write head design for 1Tb/in2," *IEEE Trans. Magn.*, vol. 40, no. 1, pp. 319-325, 2004.

[41] H.J. Richter, "The transition from longitudinal to perpendicular recording," *J. Phys. D: Appl. Phys.*, vol. 40, pp. 149-177, 2007.

[42] S.S.P. Parkin, N. More, and K.P. Roche, "Oscillations in exchange coupling and magnetoresistance in metallic superlattice structures: Co/Ru, Co/Cr, and Fe/Cr," *Phys. Rev. Lett.*, vol. 64, pp. 2304-2307, 1990.

[43] S.N. Piramanayagam, S.I. Pang, and J.P. Wang, "Magnetization and thermal stability studies on laminated antiferromagnetically coupled (LAC) media," *IEEE Trans. Magn.*, vol. 39, no. 2, pp. 657-662, 2003.

[44] H.J. Richter and E. Girt, "How antiferromagnetic coupling can stabilize recorded information," *IEEE Trans. Magn.*, vol. 38, no. 5, pp. 1867-1872, 2002.

[45] "http://en.wikipedia.org/wiki/Perpendicular_recording,".

[46] S. Iwasaki and K. Takemura, "An analysis for the circular mode of magnetization in short wavelength recording," *IEEE Trans. Magn.*, vol. 11, no. 5, pp. 1173-1175, 1975.

[47] D.M. Newman, M.L. Wears, M. Jollie, and D. Choo, "Fabrication and characterization of nano-particulate PtCo media for ultra-high density perpendicular magnetic recording," *Nanotechnology*, vol. 18, no. 20, p. 205301, 2007.

[48] "http://en.wikipedia.org/wiki/Disk_read-and-write_head,".

[49] K. Terunuma, "Current status and future of magnetic heads for HDD," *Physica status solidi C*, vol. 4, no. 12, pp. 4493-4497, 2007.

[50] S. Yuasa, T. Nagahama, A. Fukushima, Y. Suzuki, and K. Ando, "Giant room-temperature magnetoresistance in single-crystal Fe/MgO/Fe magnetic tunnel junctions," *Nature Materials*, vol. 3, no. 12, pp. 868-871, 2004.

[51] D.W. Meyer, P.E. Kupinski, and J.C. Liu, "Slider with temperature responsive transducer positioning," 1999.

[52] M. Kurita et al., "Active flying-height control slider using MEMS thermal actuator," *Microsyst. Technol.*, vol. 12, pp. 369-375, 2006.

[53] M. Suk et al., "Verification of thermally induced nanometer actuation of magnetic recording transducer to overcome mechanical and magnetical spacing challenges," *IEEE Trans. Magn.*, vol. 41, no. 11, pp. 4350-4352, 2005.

[54] S.-C. Lee and B.D. Strom, "Charaterization of thermally actuated pole tip protrusion for head-media spacing adjustment in hard disk drives," *Journal of Tribology*, vol. 130, no. 2, p. 022001, 2008.

[55] G.F. Hughes, "Patterned media write designs," *IEEE Trans. Magn.*, vol. 32, no. 6, pp. 521-527, 2000.

[56] R.M.H. New, R.F.W. Pease, and R.L. White, "Lithographically patterned single-domain cobalt islands for high density magnetic recording," *J. Magn.and Magn Mat.*, vol. 155, pp. 140-145, 1996.

[57] Y. Soeno et al., "Feasibility of discrete track perpendicular media for high track density recording," *IEEE Trans. Magn.*, vol. 39, no. 4, pp. 1967-1971, 2003.

[58] B.D. Terris, T. Thomson, and G. Hu, "Patterned media for future magnetic data storage," *Microsyst. Technol.*, vol. 13, pp. 189-196, 2007.

[59] D. Wachenschwanz et al., "Design of a manufacturable discrete track recording medium," *IEEE Trans. Mag.*, vol. 41, no. 2, pp. 670-675, 2005.

[60] H.J. Richter et al., "Recording on bit-patterned media at densities of 1 Tb/in(2) and beyond," *IEEE Trans. Magn.*, vol. 42, no. 10, pp. 2255-2260, 2006.

[61] A.O. Adeyeye and N. Singh, "Large area patterned magnetic nanostructures," *J. Phys. D: Appl. Phys.*, vol. 41, p. 153001, 2008.

[62] K. O'Grady and H. Laidler, "The limits to magnetic recording * media considerations," *J. of Magn. and Magn. Mater.*, vol. 200, p. 616}633, 1999.

[63] M. Albrecht et al., "Thermal stability and recording properties of sub-100 nm patterned CoCrPt perpendicular media," *J. Appl. Phys.*, vol. 91, pp. 6845-6847, 2002.

[64] B.D. Terris and T. Thomson, "Nanofabricated and self-assembled magnetic structures as data storage media," *J. Phys. D: Appl. Phys.*, vol. 38, p. R199–R222, 2005.

[65] X.M Yang et al., "Challenges in 1 Teradot/in(2) dot patterning using electron beam lithography for bit-patterned media," *J. Vac. Sci. & Techn. B*, vol. 25, no. 6, pp. 1953-1957 , 2007.

[66] G.M. Schmid et al., "Template fabrication for the 32 nm node and beyond," *Microelectronic Engineering*, vol. 84, p. 853–859, 2007.

[67] S. Suzuki, P. Dorsey, and M. Duwensee, "Discrete track recording media and its tribological challanges in head/disk interface," *J. Jap. Soc. of Trib.*, vol. 52, no. 6, pp. 406-411, 2007.

[68] M. Duwensee, Suzuki S., J. Lin, D. Wachenschwanz, and F.E. Talke, "Simulation of the head disk interface for discrete track media," *Microsyst. Technol.*, vol. 13,

pp. 1023-1030, 2007.

[69] K. Fukuzawa, T. Muramatsu, H. Amakawa, S. Itoh, and H. Zhang, "Nonuniform distribution of molecularly thin lubricant caused by inhomogeneous buried layers of discrete track media," *IEEE Trans Magn.*, vol. 44, no. 11, pp. 3663-3666, 2008.

[70] K. Moon, S.Y. Hong, Y. Tang, and X. Che, "Fabrication of discrete track media for narrow groove and improved reliability," 20,080,259,482.

[71] R.E. Rottmayer et al., "Heat-assited magnetic recording," *IEEE. Trans. Magn.*, vol. 42, no. 10, pp. 2417-2421, 2006.

[72] W.A. Challener et al., "Light delivery techniques for heat-assisted magnetic ," *Jpn. J. Appl. Phys.*, vol. 42, p. 981–988, 2003.

[73] J. Zhang et al., "Lubrication for heat-assisted magnetic recording media," *IEEE Trans. Magn.*, vol. 42, no. 10, pp. 2546-2548, 2006.

[74] http://media.seagate.com/2009/03/storage-effect/hamr-follows-pmr-to-keep-disks-driving/.

2 Wear and Corrosion Protective Materials in Hard Disk Drives

The rapid increase in storage density is strongly dependent on the reduction of the magnetic spacing between the read/write head and the magnetic recording layer. At very small head/disk spacing, contacts between slider and disk are likely to occur, leading to wear and degradation of the head/disk interface [1]. The development of thin protective overcoats and lubricants to reduce friction and wear is the largest tribological challenge in the design of the head/disk interface. The material of choice is carbon as the protective overcoat and perfluoropolyethers as lubricants. This chapter focuses on the carbon materials used as protective overcoats in the head/disk interface.

2.1 The Carbon Overcoat

Different forms of amorphous diamond-like carbon (a-DLC) films have been used as wear and corrosion protective overcoats on magnetic hard disks and sliders [2] [3]. Carbon forms a great variety of crystalline and disordered structures. Carbon exists in three hybridizations forms, sp^3, sp^2, and sp^1 [4]. In the sp^3-configuration, as found in diamond, the four valence electrons of the carbon atom are strongly bonded with σ-bonds of their sp^3-orbitals to the neighbor atom in a tetrahedral form. This gives unique properties in terms of high mechanical hardness, chemical inertness,

optical transparency and semiconducting band structure due to strong bonding. Industrially manufactured diamond-like carbon (DLC) has similar properties to the sp^3-diamond system. There are many different amorphous carbon forms, such as soot, chars, or glassy carbon, all with different mechanical properties [5]. Hydrogen and nitrogen can be introduced into the amorphous carbon (a-C) structure. Hydrogenated or nitrogenated carbon polymers (CH_x and CN_x, respectively) show improved tribological properties. As an example, the composition of various forms of amorphous, hydrogenated carbon alloys is shown in a ternary phase diagram in Figure 2.1. Modern depositions methods can produce different kinds of carbon over the entire triangle [6].
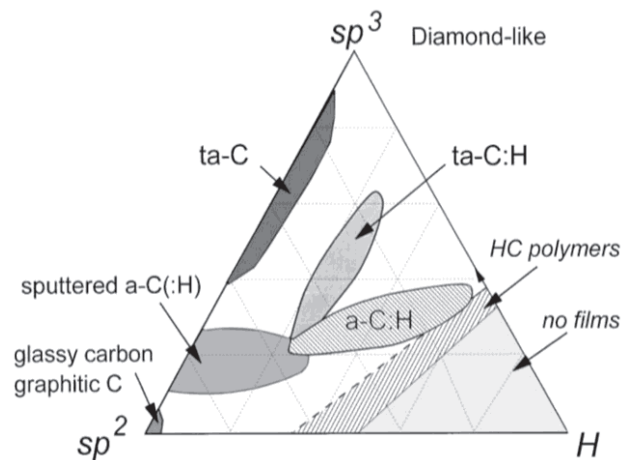
Figure 2.1: Ternary phase diagram of amorphous carbon-hydrogen alloys [6]

The structure of the carbon film is strongly dependent on the method and conditions employed during the film deposition. The amorphitization stage in the

carbon overcoat can be changed from amorphous carbon (a-C) to tetrahedral amorphous carbon (ta-C) and depends on the energy (temperature and pressure) and the reactants used during deposition. As a consequence, the mechanical and tribological properties of the films can change with the changes in the sp^2 and sp^3 content [7], [8], [9].

Manufacturing carbon overcoats for hard disks and sliders on the order of nano-meters in thickness is a technical challenge [10], [11]. Films of this thickness are likely to exhibit pin holes and defects, where corrosion can start. In the past, non-hydrogenated DLC films or amorphous carbon films have been prepared using cathodic arc or magnetron sputtering [12]. Since the mid-1990s nitrogenated amorphous carbon (CN_x) has been used in combination with hydrogen (nitrogenated-hydrogenated amorphous carbon, CN_xH_y) [13]. The amount of hydrogen and nitrogen along with the ratio of sp^2/sp^3- hybridization determines the mechanical properties of the carbon film. Different sputter and deposition systems have been developed to coat the magnetic hard disk and slider with an ultra-thin carbon layer (on the order of 1-3 nm in thickness) that is corrosion and wear resistant.

2.1.1 Deposition Methods

Diamond-like carbon films are produced via a wide range of deposition methods. The common mechanism that is used in all DLC deposition methods is that the film is condensed from a beam containing solid carbon or hydrocarbon in an inert environment or ultra-high vacuum. The high kinetic energy of the carbon is used in a

physical or chemical process on the growing film to overcome the sp^3-bonding energy [5], [14].

2.1.1.1 Ion Beam Deposition

The first diamond-like carbon was prepared using ion beam deposition (IBD) by Aisenberg and Chabot [15]. Carbon ions are produced by the plasma between the electrode and the grid as shown in Figure 2.2. Ion beam deposition is the most commonly used method until today; however, many different variations have been developed to attain a certain coating.

An ion-gun generates an argon ion beam which is focused on a graphite cathode (target) to form carbon ions by plasma sputtering [16] (Figure 2.2 a)). A magnetic field is used to confine the plasma and maximize the ionization. Magnets are placed behind the graphite target, which cause the electrons to spiral and increase their path length, and thus, increase the ionization rate of the plasma (Magnetron sputtering deposition (MSD)). This method was improved by using hydrocarbon gas injected directly into the plasma [17]. The carbon ions are accelerated by an applied potential thru the grid electrode towards the substrate in a high vacuum environment. The impact of these ions on the target disk induces sp^3-bonding. Plasma sputtering is the most common industrial process for DLC deposition and was used for early amorphous carbon deposition on hard disks.

In modern systems, a radio frequency (RF) discharge is created between two electrodes (the powered electrode and grid electrode) to create the plasma [**18**]. Figure 2.2 b) shows an image of the improved setup. This is also called plasma beam deposition. In addition, this method is widely used to generate nitrogenated DLC films by adding nitrogen gas to the plasma and hydrocarbons. The created plasma is mono-energetic. Therefore, the deposition is uniform and independent from the substrate geometry. The conditions for sputtering can be controlled by the plasma power (potential between the electrode and the grid) and gas pressure.

a)

b)

graphite target

electrode (-)

Ar ion beam

C beam

RF discharge

reactive gas

ion gun

grid
electrode (+)

disk target
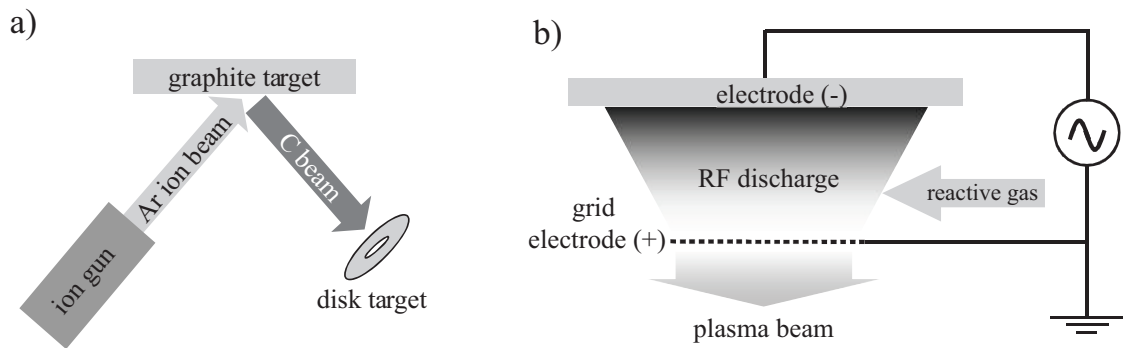
plasma beam

Figure 2.2: Ion beam deposition method. a) direct ion beam, b) ion assisted sputtering

2.1.1.2 Cathodic Vacuum Arc

Cathodic arc deposition is based on the formation of plasma by a high current electrical discharge between a small carbon striker electrode and a graphite cathode in

high vacuum. Particles and high energy plasma with a high carbon ion density is generated in a so-called evaporator. The particles are filtered by magnetic micro-particle filters which guide the carbon ions towards the substrate. The magnet array homogenizes and flattens the carbon plasma distribution and gives a uniform deposition profile on the target. As an example, Figure 2.3 shows the single (a) and the double (b) 90 degree bend filter system which is known as filtered cathodic vacuum arc (FCVA) [19]. In Figure 2.3c) a high current pulsed arc (HCA) with a 120° filter tube is shown. In both methods, the generated carbon ions in the plasma follow the filter axis, while the larger or smaller particles hit the walls and do not reach the substrate.

The evaporator is used in a pulsed mode of approximately 100Hz with pulses in the low millisecond after primary spark initiates the discharge. Per pulse a layer of 0.07-0.3 nm is deposited on the target and the process time of a whole wafer would be below two seconds. Cathodic vacuum arc is commonly used for carbon coating of sliders.
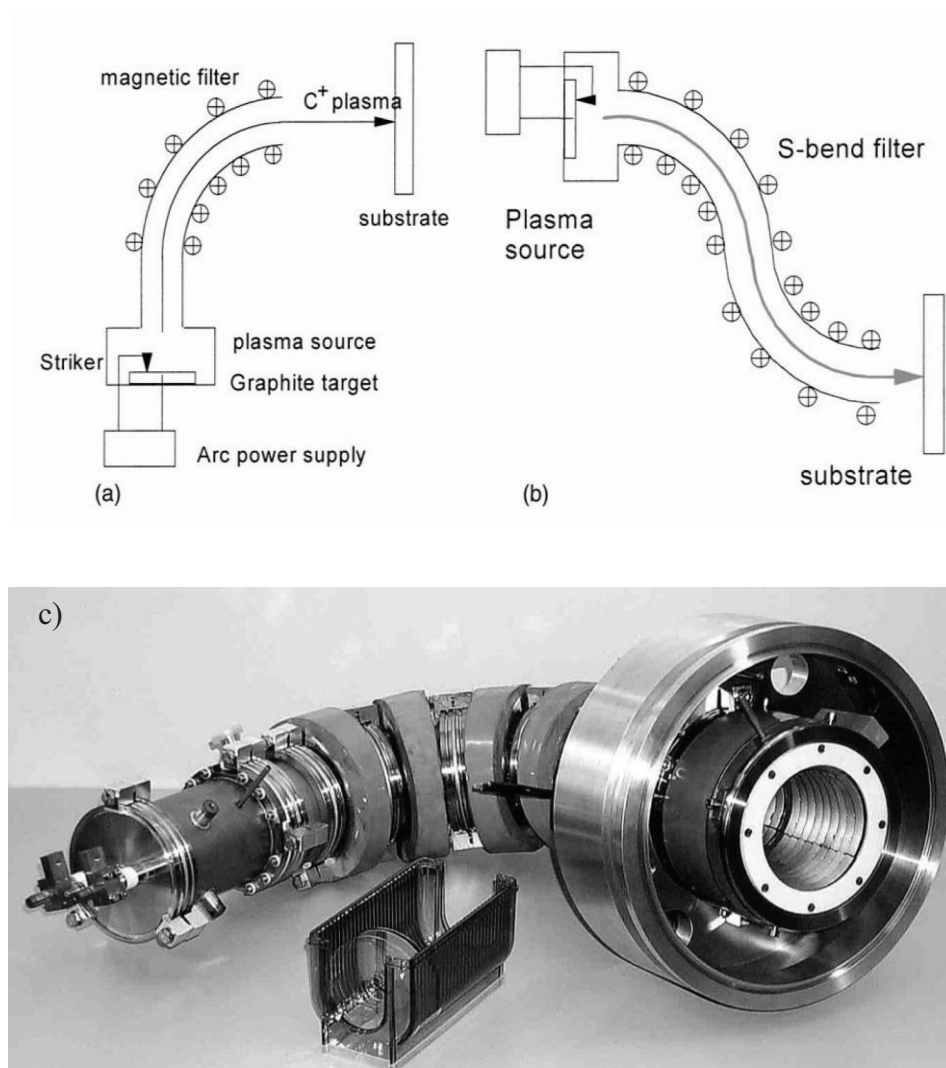
Figure 2.3: Schematic of a cathodic arc deposition system, a single bend (a) and an S- bend filter (b) [5]. In c) a 120° macro-particle filter is shown [20].

It has been shown that cathodic vacuum arc deposition has a very low coverage limit of ~1.0 nm due to its high energy deposition and carbon ion density. X-ray photoelectron spectroscopy and nano-scratch testing have shown that these ultra-thin overcoats have improved corrosion performance and increased resistivity against plastic deformation even at a thickness of only 1 nm [20].

2.1.1.3 Additional Deposition Methods

In addition to ion beam and cathodic arc deposition, a number of different deposition methods (not only for carbon and DLC) have been developed. The following methods are utilized in laboratories and small form factor manufacturing.

In pulsed laser deposition (PLD) a high energy laser pulse vaporizes the carbon material and forms a high energy plasma. The plasma expands towards the substrate and gives the atoms the energy to create the sp^3-bonds. The pulsed laser deposition (PLD) is a multifunctional method for depositing different materials on a substrate. PLD has extraordinary features, which makes it remarkable for the laboratory usage.

Another popular laboratory DLC deposition method is the plasma enhanced chemical vapor deposition (PECVD) which is based on a chemical process rather than high energy. The reactor consists of two electrodes of different areas in an inert gas chamber. The high frequency power (RF) is coupled to the cathode, on which the substrate is mounted, and the anode is grounded. The RF-power produces the plasma between the electrodes. The electrons in the plasma have a higher mobility than the produced ions and build up a sheath next to the electrodes with an excess of ions. A higher negative sheath voltage accelerates the positive ions towards the substrate to form sp^3-bonding.

2.2 Characterization of Carbon Overcoats

Carbon composition, defect analysis, surface energies and mechanical properties are characterized by different surface and structure analysis to ensure the performance of the materials in the head/disk interface structure. Table 2.1 summarizes a selection of surface characterization techniques and their application. This chapter will focus on methods that are used for the analysis of carbon overcoats (COC).

Raman spectroscopy, X-ray photoelectron spectroscopy (XPS), and Auger electron spectroscopy (AES) are the most essential techniques to characterize carbon overcoats (COC) and will be explained in detail. The ternary phase diagram in Figure 2 emphasizes that two parameters determine the structure and properties of diamond-like carbons, the fraction of sp3 bonded carbon and the content of hydrogen and/or nitrogen. Structural characterization focuses on these two parameters. In addition to the above characterization methods, diffraction and nuclear magnetic resonance (NMR) have also been used to determine structural parameters. Topography and mechanical properties of the carbon films can be performed by atomic force microscopy (AFM), nano-hardness and nano-scratch measurements. It is important to conduct these film characterizations to correlate and optimize deposition parameters and tribological performance parameters such as the coefficient of friction, stiction and wear rate.

Table 2.1: Different surface characterization techniques and their application.

Technique	Application examples
Raman spectroscopy	Carbon structure and contamination analysis
Infrared spectroscopy	Polymer characterization, particle contamination
X-ray photoelectron spectroscopy (XPS)	Carbon composition, film thickness, disk corrosion
Auger Electron Spectroscopy (AES)	Carbon composition, defect analysis
AFM	Surface roughness, topography,
Nano-indentation / nano-scratch test	Hardness, Young's modulus, scratch resistance
Ellipsometry	Refractive index, film thickness

2.2.1 Raman Spectroscopy

The Raman effect was first demonstrated in 1928 by Sir C. R. Raman, who received the Nobel prize in 1930 for his work [21]. Raman spectroscopy measures disperse radiation, which is caused by inelastic scattering of photons due to molecular vibrations and rotations of the specimen's surface atoms/molecules (which are energy specific); hence, one can obtain a detailed bonding structure of the carbon overcoat [5]. In the Raman spectrometer, a high power laser light beam is sent through an edge filter for subtracting the excitation side bands to form a truly monochromatic light, which is focused via an optical microscope perpendicular onto the sample surface. The laser spot can be focused to below 1 μm on the sample which gives relatively high resolution compared with other optical analysis methods. The very weak disperse emitted light (Raman modes) from the sample is collected by the same optics and sent

to a high performance detector to analyze the spectrum. Raman spectroscopy can be performed in air and the sample does not need to be in a vacuum.

In Figure 2.4, typical Raman spectra of diamond, graphite and amorphous carbon are compared. Diamond has a single Raman active mode, the diamond-like D-band at 1332 cm^{-1}. Single crystal graphite shows only one Raman active mode which is called the graphite like G-band at 1580 cm^{-1}. Amorphous graphite consists of two modes, the G-band and a mode at approximately 1350 cm^{-1} which is labeled "D" for disordered [5]. It is important to mention that the latter D-mode does not compare to the D-band in crystalline diamond. It corresponds to breathing vibrations in the amorphous carbon. However, the position is somewhat similar to the diamond-like D-band. It is significant for carbon materials that the Raman spectra remain dominated by these two D- and G- modes.

Ferrari et al. characterized the G-band of the Raman spectra and the ratio of intensity of the amorphous D-band (I(D)) divided by the intensity of the G-band (I(G)) as a function of amorphisation [6]. They describe a three-stage model of the disorder of carbon from perfect graphite to tetrahedral amorphous carbon. The first stage shows a reduction in grain size of ordered graphite layers which causes an up-shift of the G-band to 1600 cm^{-1}. Since the disorder for this system increases, the ratio of I(D)/I(G) increases. Stage 2 corresponds to a topological disordering but an increased sp^2 network which is found in sputtered amorphous carbon. Therefore, the G-band and I(D)/I(G) are decreasing. In stage 3 the sp^3 content increases as the ring-form of graphite is changing into short chain like order. Since the vibrational frequency of

these short chains is higher the G-band position increases while the I(D)/I(G) is further decreased [6].
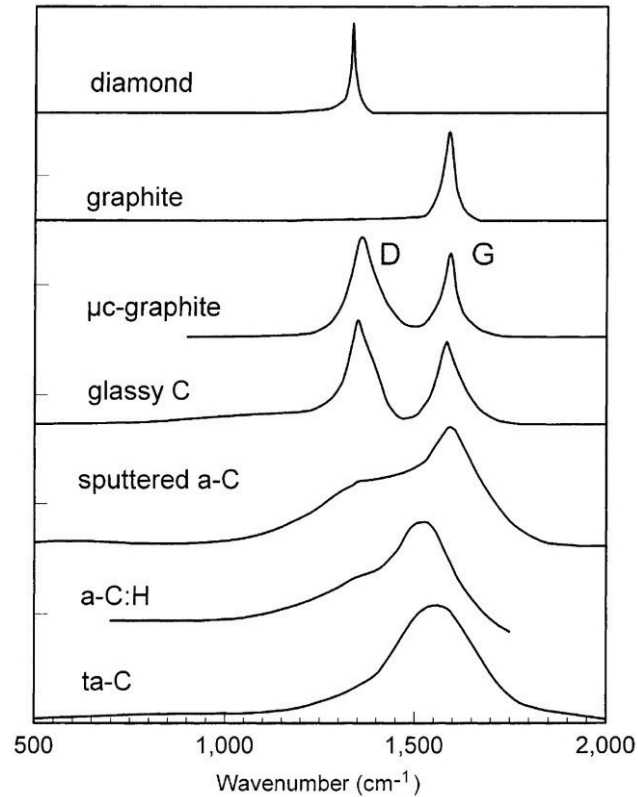
Figure 2.4: Comparison of typical Raman spectra of different carbon structures [5]

Structural modifications by nitrogen or hydrogen can be identified by a shift of the G-band position as well as I(D)/I(G) peak ratios. In addition, an increased photoluminescence background can be observed, which is directly related to the hydrogen or nitrogen amount in the carbon overcoat [22]. An increased concentration leads to an increase of photoluminescence intensity, due to the increase in non-radiative recombination, known as dangling bonds.
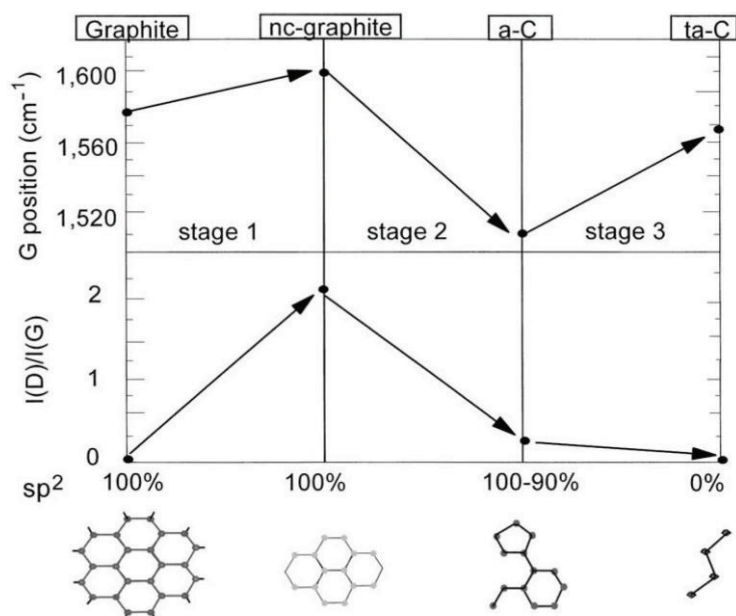
Figure 2.5: Schematic of the variation of Raman G-band wavenumber (cm^{-1}) and I(D)/I(G) ratio as a function of the degree of disorder. The three stages of amorphisation of carbon are shown [**5**].

Raman spectroscopy is used to investigate the structural parameters of the carbon overcoats from disks and sliders. In addition, it can be used to measure the thickness of thin carbon films down to 10 nm [**23**], [**24**].

2.2.2 X-ray Photoelectron Spectroscopy (XPS)

X-ray photoelectron spectroscopy (XPS) is a technique that measures composition, chemical and electronic state of the elements that exist within a material. Electrons from occupied states in the core level of an atom are released by the high X-

ray energy ($\hbar\omega$) and are analyzed based on their kinetic energy (E_{kin}). This is described by

$$\hbar\omega = \phi + E_{kin} + E_b \qquad (2.1)$$

where ϕ is the workfunction of the atom and E_b is the binding energy. Since the X-ray energy is constant depending on the light source and the kinetic energy can be analysed, characteristic peaks of the binding energy of elements of interest can be detected with an XPS spectrum.

The X-rays are focused on the sample in an analytic chamber. The X-rays generate electrons from the core level of the atoms. The electrons are collected in a half-dome analyser and their specific kinetic energy is determined. The individual peaks of the elements in the sample are recorded in a so-called spectrum survey. Individual peaks can be analysed by a second, high resolution scan. Hence, small peak shifts or changes of the intensity can be determined. This gives information about the bonding state of the atoms. XPS gives an insight into the composition of the carbon overcoat and lubricant. XPS is also used to study the thickness and corrosion state of the hard disk and the slider.

Another electron spectroscopy technique that determines defects, composition and corrosion in the head disk interface is Auger electron spectroscopy (AES). While XPS is averaging over a large area of several micro meters to millimeters, AES is capable of a quantitative element characterization over small areas of less than 0.5 µm

in diameter.   It is an essential elemental analysis technique especially for submicroscopic components as can be found in the read/write element in the slider.

2.2.3 Atomic Force Microscopy (AFM)

The atomic force microscope (AFM) [25] is a scanning probe microscope, based on the intermolecular interaction between the sample surface and a sharp tip (AFM tip). This allows it to measure topography and surface forces of conducting and insulating surfaces with nano-meter resolution [26]. Depending on the measurement technique, the forces that are measured with an AFM are Van der Waals forces and capillary forces (in bulk liquids), mechanical contact force such as lateral forces (LFM), magnetic forces (MFM), electrostatic forces (EMF), etc.

The AFM tip is mounted on a cantilever spring which deflects as a reaction to the applied forces. This deflection is measured by a laser beam which is reflected from the back of the cantilever onto a 4-quadrant photo detector. Figure 2.6 shows a schematic of the work principle of an AFM.
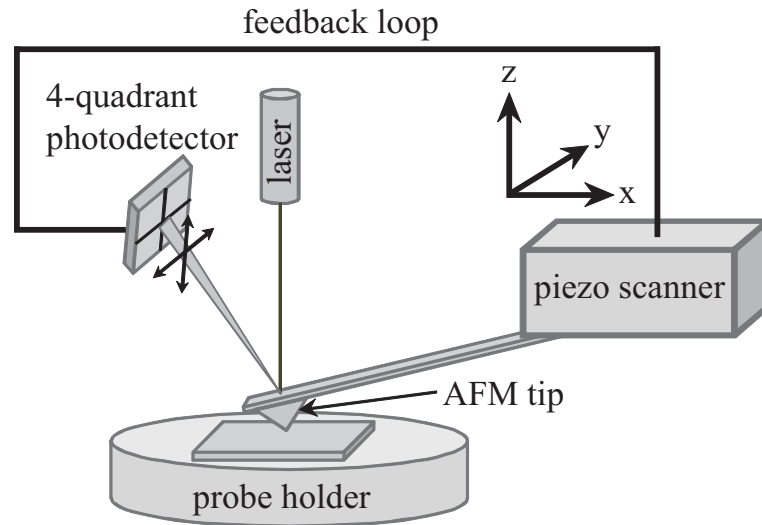
Figure 2.6: Schematic of the AFM principle

During measurement the AFM tip is in a feedback loop with a piezo scanner to adjust the tip-to-sample distance to maintain a constant force (constant deflection of the cantilever) between the AFM tip and the sample. The piezo scanner is usually a tube scanner that moves the AFM cantilever and tip in x, y, and z-direction. The sample is scanned line by line by moving the AFM tip back and forth in x-direction in a raster-like motion over the sample. After each line the tip is moved one step in the y-direction until a 2-dimensional image is obtained. Using the feedback information of the z-direction from the scanner, one can generate a 3-dimensional topographical image.

2.2.3.1   Contact Mode

The AFM can be operated in a number of modes, which are either static or dynamic, depending on the application. In static mode the force between the tip and the surface is kept constant during scanning by maintaining a constant cantilever deflection. The laser point reflecting onto the photo detector is kept in the same vertical position and according to the feedback signal the piezo moves the tip up or down. The tip is in actual contact with the sample surface and in addition to the topography a friction signal can be obtained by measuring the torsion of the cantilever beam. The frictional signal is obtain from the horizontal position of the laser on the photo detector. During a measurement cycle, the tip is moved back and forth (trace and re-trace) over the sample surface and generates a so-called "friction loop" as shown in Figure 2.7. The friction signal shows a positive sign for the trace and negative sign for the retrace. The friction force can be estimated from the average lateral friction signal (solid lines in Figure 2.7) of the trace or the re-trace.
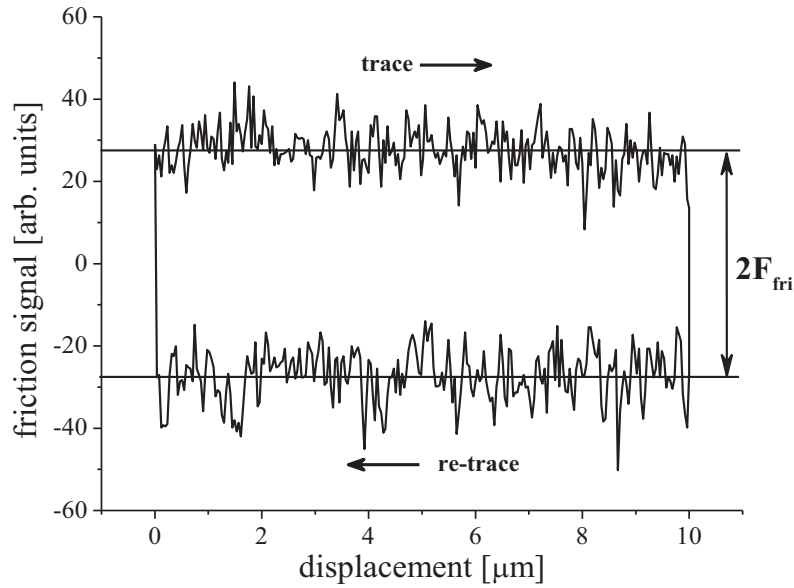
Figure 2.7: AFM friction loop

2.2.3.2   Close Contact Mode (Dynamic Mode)

A method to measure the topography without disturbing the sample surface is the close-contact-mode (dynamic mode) where the cantilever is externally oscillated close to its resonance frequency in non-contact or in intermittent contact with the sample surface. Tip-sample interaction forces acting on the cantilever when the tip comes close to the surface cause the amplitude of this oscillation to decrease. The oscillation amplitude, phase, and change in resonance frequency can be determined with very high sensitivity and thus allows very accurate vertical and lateral resolution.

2.2.3.3   Magnetic Force Microscopy (MFM Mode)

Magnetic force microscopy allows the visualization of the magnetic bits on the disk surface with high lateral resolution. A magnetized tip is used in close-contact mode and the interaction with the magnetic material causes a change in the resonance frequency of the tip. MFM has become the standard technique to determine the bit length and width and characterization of bit structure irregularities in failure areas of the disk. Figure 2.8 shows a typical MFM image of a magnetized section of a hard disk with the transition of the magnetic direction of the bits. The image shows a longitudinal magnetic recording sample. The transition between a light and a dark area represents a "one" (in binary code), while a larger dark or light area can consist of multiple "zeros". This particular disk shows a bit width of approximately 200 nm and a bit aspect ratio of 8:1.

In addition, the geometry of the pole tip of the slider can be measured using AFM and MFM techniques to find correlations with the emerging field distribution of the write head [**27**]. The distance of the magnetized tip towards the GMR or TMR read sensor can be varied while the sensor's signal is measured. This gives a map of the three-dimensional sensitivity of the read sensor.

500 nm
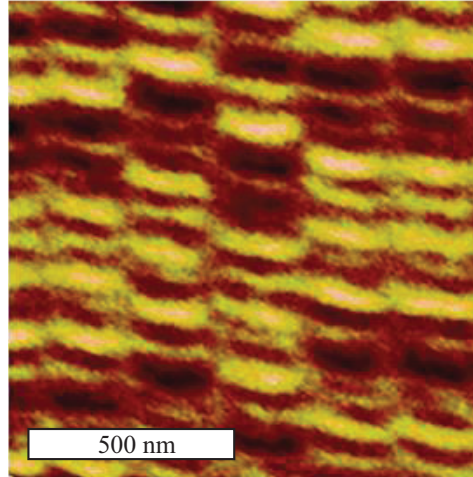
Figure 2.8: MFM image of a written section of a magnetic hard disk

2.2.3.4 Adhesion Measurements Using AFM Force-Distance Curve

In this dissertation, the AFM is used to determine intermolecular interactions between the probe tip and the sample surface using force distance curves. For this method, the AFM tip is first moved towards the surface and then retracted from it while the static deflection of the cantilever is monitored as a function of displacement. Using Hook's law one can determine the force that is needed to "pull-off" the tip from the sample surface. A detailed description of the procedure is given in Chapter 6.

2.2.3.5 Intermolecular Forces

In the head/disk interface, intermolecular forces, which are close range forces between atoms and molecules, play an important role at head-disk spacings below 5

nm. This interaction of atoms and molecules is described by the Lennard-Jones potential

$$F(r) = -\frac{A}{r^6} + \frac{B}{r^{12}}$$

(2.2)

where r is the distance between the atoms (or molecules) and A, B are Hamaker constants. The Lennard-Jones potential consists of relatively long range attractive forces ($-\frac{A}{r^6}$ term) and short range repulsive forces ($\frac{B}{r^{12}}$ term).

The method to calculate the Hamaker constant A for two surfaces separated by a medium is given by Lifshitz [28]

$$A_{123} = \frac{3}{4}k_BT\left(\frac{\varepsilon_1 - \varepsilon_3}{\varepsilon_1 + \varepsilon_3}\right)\left(\frac{\varepsilon_2 - \varepsilon_3}{\varepsilon_2 + \varepsilon_3}\right) + \left(\frac{2h\upsilon_e}{8\sqrt{2}} \frac{(n_1^2 - n_3^2)(n_2^2 - n_3^2)}{(n_1^2 + n_3^2)^{1/2}(n_2^2 + n_3^2)^{1/2}[(n_1^2 + n_3^2)^{1/2} + (n_2^2 + n_3^2)^{1/2}]}\right)$$

(2.3)

where ε_i is the permittivity of the material i, n_i is the refractive index of the material i, υ_e is the ionization frequency, h is Planck's constant, k_b is Boltzmann's constant and T is the temperature. The Hamaker constant is governed by the permittivity and the refractive index of the materials used and changes in these properties greatly influence the intermolecular forces between the surfaces.

2.2.4 Roughness Measurements

Atomic force microscopy in contact and close contact mode is widely used to determine the roughness of carbon coated disks and sliders. Roughness measurements are generally conducted using a 0.75μm x 0.75μm sampling area. Different roughness models have been developed over time and a summary is given in the following.

The root mean square roughness (Rms) and the roughness average (Ra) are calculated as follows:

$$Rms = \sqrt{\frac{1}{L}\int_0^L (z(x) - z_{mean})^2 \, dx} \tag{2.4}$$

$$Ra = \frac{1}{L}\int_0^L |z(x) - z_{mean}| \, dx \tag{2.5}$$

where $z(x)$ is the profile value of the roughness profile, L is the profile length, and z_{mean} is the mean value of the profile given by $z_{mean} = \frac{1}{L}\int_0^L z(x)dx$. The Rms or Ra value is typically one tenth of the vertical distance between the highest and the lowest point on the measured surface, and is called the Peak-to-Valley value, $z_{pv} = |z_{max}| + |z_{min}|$. Figure 2.9 shows a roughness profile and the different roughness parameters of a random surface.
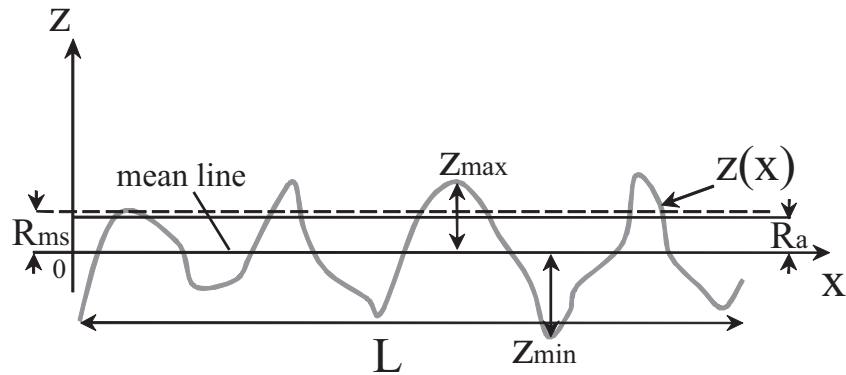
Figure 2.9: Roughness profile

The amplitude density function (also known as the peak-height distribution) is another important parameter to characterize surface roughness. The amplitude density function equals the number of peaks N within the roughness profile as a function of their peak heights with respect to the mean line. For truly random surfaces the amplitude density function would be a Gaussian distribution. However, many surfaces differ from a Gaussian. That asymmetry of a height distribution about the mean can be described by another surface roughness parameter which is called skewness R_{SK}

$$R_{SK} = \frac{1}{NR_q^3}\sum_{i=1}^{N} z_i^3 \qquad (2.6)$$

Figure 2.10 shows how different profiles lead to different amplitude density functions and skewness.
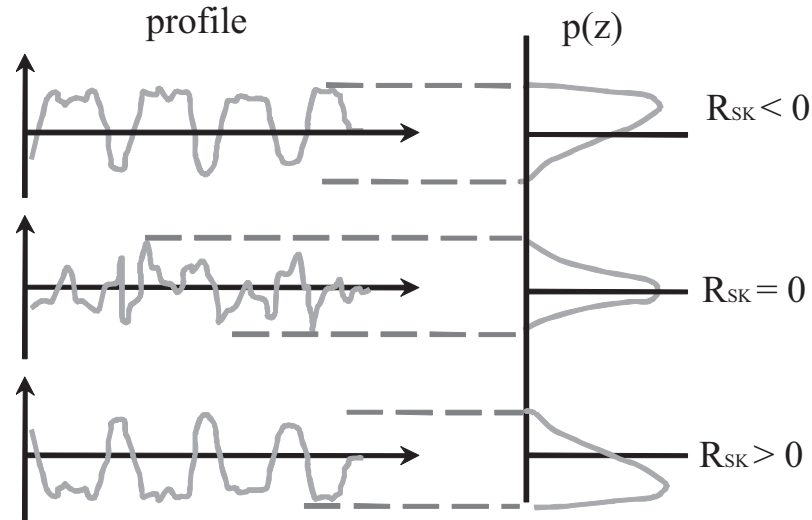
Figure 2.10: Construction of the amplitude density function with different profiles that lead to various values of the skewness

Another roughness parameter that indicates the shape of the peak height distribution in terms of width and height is the kurtosis R_{KU} given by

$$R_{KU} = \frac{1}{NR_q^4} \sum_{i=1}^{N} z_i^4 \qquad (2.7)$$

Figure 2.11 shows profiles that lead to various values of kurtosis. The ideal Gaussian shape of the amplitude density function would have a kurtosis of 3. Most profiles that have a kurtosis of less than three are very broad with a small maximum.

$R_{KU} < 3$

$R_{KU} = 3$

$R_{KU} > 3$
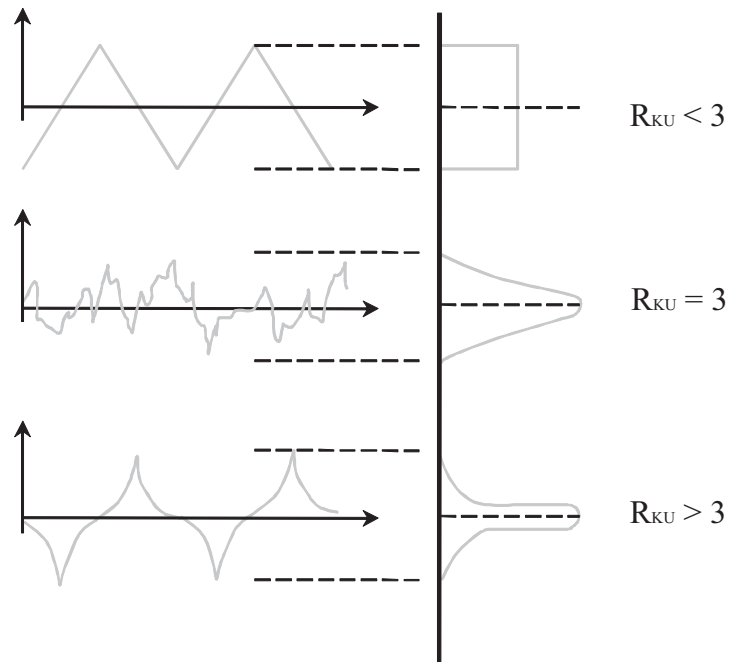
Figure 2.11: Different profiles that lead to various values of the kurtosis

2.2.5 Contact Mechanics

This chapter gives an overview about the contact mechanics of a flat (the sample surface) against a sphere (AFM tip) such as is used for AFM friction and force displacement measurements. For simplicity it is assumed that the contacts deform elastically. A contact model is shown in Figure 2.12.
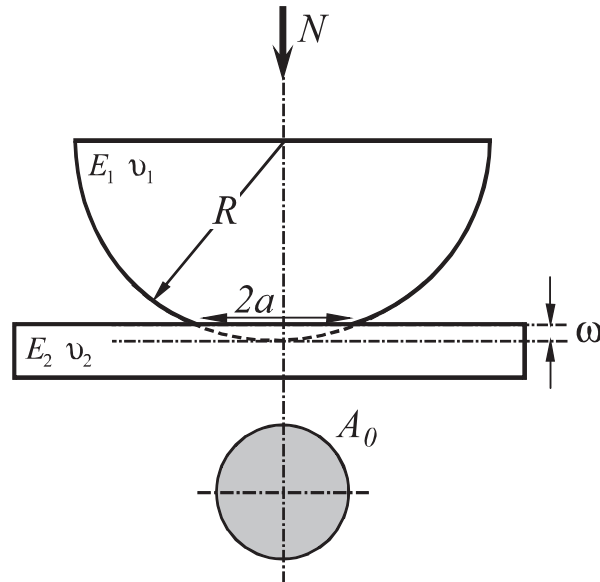
Figure 2.12: Schematic of the contact between a sphere and a flat surface

The so-called interference height ω of a contact is the distance that two points outside the contact zone move closer together and can be calculated using

$$\omega = \frac{a^2}{R} \tag{2.8}$$

where a is the contact radius, and R is the radius of the sphere.

Several theories describe the elastic deformation between a flat surface and a sphere [29]. Differences occur from the relation between the applied load N, the contact radius a, or the interference height ω of the contact. The three most commonly used theories, developed by Hertz [30], Derjaguin-Müller-Toporov (DMT) [31], and Johnson-Kendall-Roberts (JKR) [32] are summarized in Table 2.2. Hertz theory applies to an elastic contact, where neither surface forces nor adhesion forces

are taken into account. The DMT and JKR model take the adhesion force into account either outside (DMT) or inside (JKR) the contact area.

Table 2.2: Relationship of the contact radius a, the sample deformation δ, and the adhesion force between the Hertz, DMT, and JKR theories [29]

	Hertz	DMT	JKR
a	$\sqrt[3]{\dfrac{RN}{E^*}}$	$\sqrt[3]{\dfrac{R}{E^*}(N+2\pi RW)}$	$\sqrt[3]{\dfrac{R}{E^*}\left(N+3\pi RW+\sqrt{6\pi RWN+(3\pi RW)^2}\right)}$
ω	$\dfrac{a^2}{R}=\left(\dfrac{N^2}{RE^{*2}}\right)^{1/3}$	$\dfrac{a^2}{R}=\dfrac{(N+2\pi RW)^{2/3}}{\sqrt[3]{RE^{*2}}}$	$\dfrac{a^2}{R}-\dfrac{2}{3}\sqrt{\dfrac{6\pi Wa}{E^*}}$
F_{adh}	0	$2\pi RW$	$\dfrac{3\pi RW}{2}$

E^* is the reduced Young's modulus $\dfrac{1}{E^*}=\dfrac{3}{4}\left(\dfrac{1-\upsilon_1^2}{E_1}+\dfrac{1-\upsilon_2^2}{E_2}\right)$, which can be determined from the Young's modulus and the Poisson's ratio of the sphere (E_1,υ_1) and the flat surface (E_2,υ_2), respectively. W is the adhesion work per unit area, which is related to the surface energy of the two materials in contact [28]. This will be described in more detail in Chapter 6, where the focus is on the adhesion between two smooth surfaces coated with a molecularly thin lubricant film. In the DMT model the elastic sphere is deformed according to the Hertz model. The JKR model considers the short range forces inside the contact, but neglects the long-range forces outside the contact. Because of this, the contact radius (a_{JKR}) changes as shown in Table 2.2.

The DMT and JKR model are actual limits of the contact theory at opposite

extremes [**33**] over a spectrum of the elasticity parameter

$$\lambda = \frac{2.06}{D_0} \sqrt[3]{\frac{RW^2}{\pi E^2}}$$ (2.9)

where D_0 is a typical atomic dimension. When λ is increasing from zero to infinity,

a continuous transition from the DMT to the JKR model is established. Figure 2.13

shows the transition between DMT and JKR model, which is known as the Mauguis-

Dugdale (MD) model.
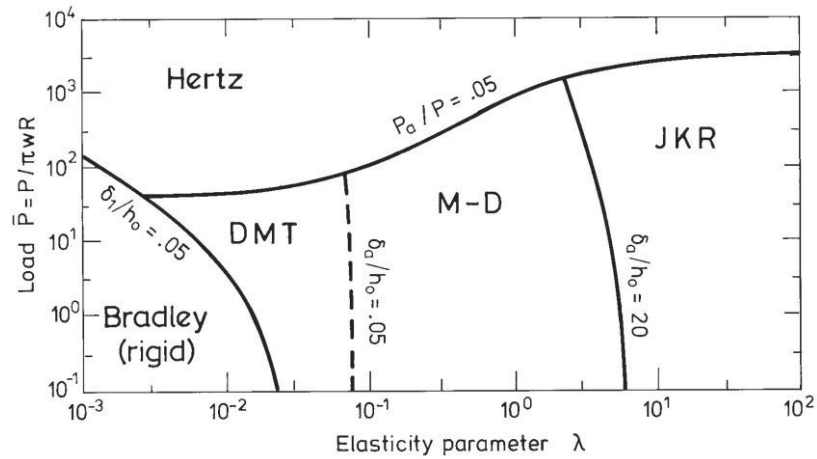
Figure 2.13: Adhesion map for contact of elastic spheres [**34**]

This dissertation is only concerned with the contact of an AFM tip (which is

assumed to be a perfect sphere) and the ultra-smooth surface of the magnetic disk.

However, in a practical case, rough surfaces are present and the adhesion is modeled

by a collection of spherical asperities (see Greenwood and Williamson (GW) contact model) [35]. The model assumes a smooth surface in contact with an equivalent rough surface. The asperities have a probability height distribution and a simple spherical geometry.

2.2.5.1 Plastic Deformation

Tabor [36] has shown for a ball indentation test, that the onset of plastic flow is reached at about $0.6H$, where H is the hardness. Greenwood and Williamson [35] defined the so-called critical interference ω_c, the point where a change from elastic to plastic deformation occurs, as follows

$$\omega_c = 0.89 R \left(\frac{H}{E^*} \right)^2 \qquad (2.10)$$

Later, Chang et al. [37] considered volume conservation for plastically deformed spherical contacts. The radius of contact a for a contact interference of $\omega > \omega_c$ can be calculated as follows

$$a = \sqrt{4R\omega \left(2 - \frac{\omega_c}{\omega} \right)} \qquad (2.11)$$

Figure 2.14 shows such a contact. One can observe that the contact radius is larger compared to the Hertz model. Kogut and Etsion [38] developed an adhesion model for elastic-plastic contact. In that case, a dimensionless interference ratio ω / ω_c is

used to determine whether the contact is in the elastic, elastic-plastic, or fully plastic regime.
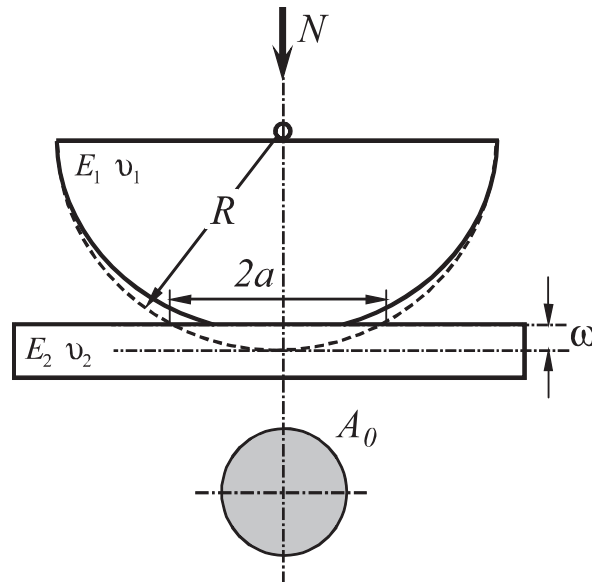
Figure 2.14: Schematic of the contact between a sphere and a flat surface using a volume conservation model [37]

2.2.6 Nano-indentation

Nano-indentation and nano-scratch testing has been used to obtain the hardness, the Young's modulus, the friction coefficient, the scratch resistance and other mechanical properties at small dimensions [39], [40]. "Nano" refers to depth-sensing during the indentation measurement which is in the sub-micrometer range

down to a few nano-meters. The instrument is capable of making small indentations and measuring displacements with high accuracy while recording the normal load (and lateral force - for scratch testing) [41]. In addition, ultrasonically excited nano-indentation testing can be used to provide an accelerated wear and fatigue test at a local contact [42].

In nano-indentation, a diamond tip with a high precision geometry such as a so-called Berkovich tip is pressed into the sample with a known load. The tip has a three-sided pyramid geometry and is calibrated against a reference sample, such as quartz. During the indentation process the depth of penetration and the normal load are measured and the area of the indentation can be determined using the known geometry of the indentation tip. The normal load and the displacement can be plotted in a load-displacement curve (Figure 2.15), from which further material properties can be calculated. If the load and unload curve overlap, the materials behaves elastically. However, in most cases the sample undergoes plastic deformation during loading and does not regain its original shape as the load decreases. Therefore, the load and unload curve do not overlap (see Figure 2.15). The difference is called "loading-unloading hysteresis".

The slope of the curve dN/dh during unloading is indicative of the stiffness of the contact S. The reduced Young's modulus E^{*} can be calculated using the stiffness of the contact [43]

$$E^* = \frac{1}{\beta} \frac{\sqrt{\pi}}{2} \frac{S}{\sqrt{A(h_c)}} \qquad (2.12)$$

where $A(h_c)$ is the area of the indentation at the contact depth h_c, and β is a geometrical constant. The hardness H is defined as the maximum load N_{max} divided by the residual indentation area $A(h_c)$

$$H = \frac{N_{max}}{A(h_c)} \qquad (2.13)$$

The plasticity index of the system is [29]

$$\psi_P = \frac{W_1}{W_1 + W_2} \qquad (2.14)$$

where W_1 is the area between the loading and unloading in the force displacement curve (see Figure 2.15) and the sum of $W_1 + W_2$ is the work done on the indenter tip and the sample. The work W_1 is a measure of the dissipated energy needed for the deformation [44]. For a perfectly elastic surface $\psi_P = 0$, since $A_1 = 0$, while for a entirely plastic surface $\psi_P = 1$, since $A_2 = 0$. Most samples have a plasticity index $1 < \psi_P < 1$.

The qualitative hardness and Young's modulus of carbon films can be investigated using a nano-indenter (Triboscope®, Hysitron, Inc.). One of the problems of performing nano-indentations on ultra-thin coating is that for hardness

measurements the maximal indentation depth should not exceed 10% of the thickness of the material to be measured to eliminate substrate effects [**45**]. Hence, the indentation depth of state of the art carbon overcoats of 3nm thickness has to be less than 0.3 nm, or approximately two atomic layers of carbon.
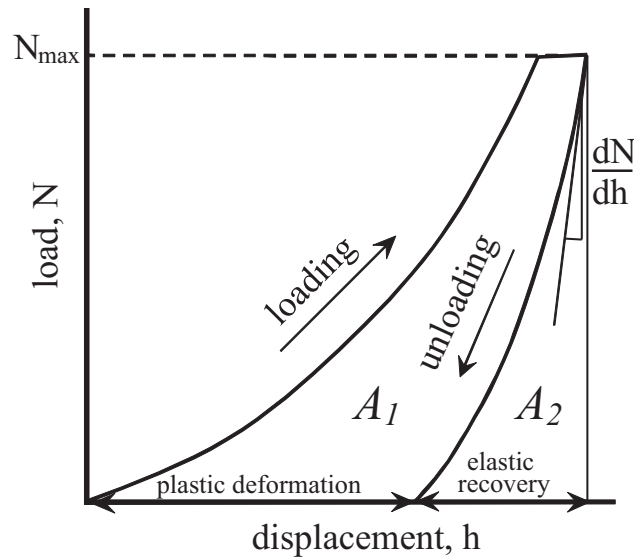
Figure 2.15: Schematic of load-displacement curve for a nano-indentation test.

2.2.6.1 Nano-scratch Test

Nano-scratches are generated by moving the diamond probe perpendicular over the sample surface to investigate abrasive wear resistance of a coating [**26**]. In addition, by recording the normal load and lateral force, the friction coefficient can be calculated. The diamond probe is scratched across the surface under either a constant

load or a progressively increasing load until film failure occurs. Scratching at different locations at constant load can be used to investigate coating quality and homogeneity.

2.2.6.2 Nano-indentation in the Presence of Ultrasonic Excitation

The dynamic interfacial fatigue of materials can be determined by ultrasonically excited nano-indentation or nano-scratch techniques [46]. An ultrasonic piezoelectric transducer (PZT) can be used to generate a sinusoidal displacement of the sample in the direction of the indentation, normal to the surface. In the presence of ultrasonic excitation, a large number of impacts occur between the indenter tip and the sample, while without ultrasonic vibrations the contact is static.

2.3 Silicon Nitride Films as Protective Overcoats

In high density magnetic recording the carbon thickness must be reduced to less than 2 nm [47]. At this thickness, the carbon coverage will not be sufficient to prevent oxidation of the magnetic layer. Silicon nitride has been found to be promising in preliminary tests as a thin overcoat for hard disks and shows superior properties such as a low coverage limit of 1 nm thickness, high density and strong durability. Yen et al. [48] deposited amorphous silicon nitride (a-SiN) using plasma enhanced chemical vapor deposition. They found that the density and hardness exceeded the values found for amorphous carbon nitrides. Table 2.3 shows a comparison between silicon nitride with Si_3N_4 stochiometry and a reference

amorphous carbon sample. The density was measured with X-ray reflectivity of a sample with a film thickness of 50-60 nm and the hardness was determined using a nano-indentation on a 120 nm thick film.

Table 2.3: Properties of a-SiN$_x$ and reference a-CN$_x$ overcoats [48].

Overcoat-type	Density [g/cm^3]	Hardness [GPa]
a-SiN$_x$	3.2	25
a-CN$_x$	1.8	11

In their experiments they determined the minimum thickness of the coverage limit. X-ray photoelectron spectroscopy showed that the Co2p-oxide shift disappears at a film thickness of 1 nm as shown in Figure 2.16. However, the tribological properties of the material are not well understood and vary significantly with the stochiometry of the film (Si:N), which also plays an important role in the interaction between silicon nitride surface and the applied lubricant [49].

The implementation of iron particles in a-SiN seems to be a promising method to convert the magnetically inactive protective overcoat into a soft magnetic layer, which could enhance the magnetic properties of the magnetic hard disk. Thus, the magnetic spacing between the disk and the slider could dramatically decrease, increasing the recording density. This soft magnetic layer can give an additional torque to switch the magnetic direction in the recording layer, while keeping good durability.
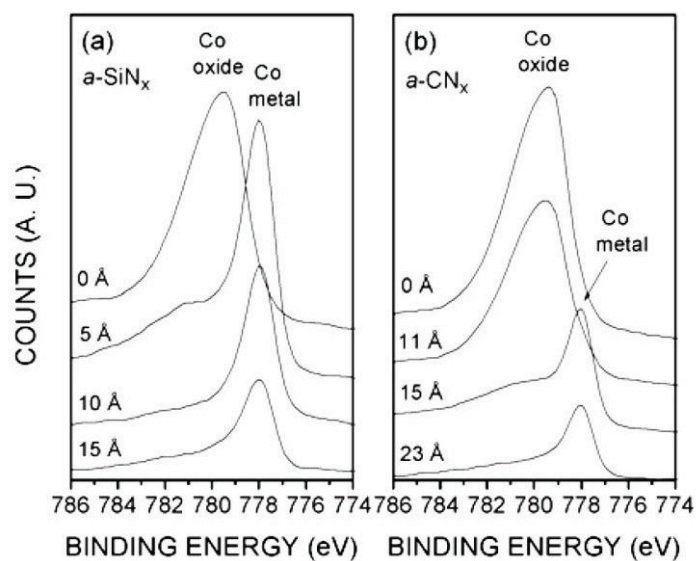
Figure 2.16: XPS spectra of the Co2p peak for (a) a-SiN$_x$ coated and (b) a-CN$_x$ coated CoCrPt disks [48].

There are still open questions on the performance of theses layers, both from a magnetically and mechanically standpoint. For example, are there any changes in the intermolecular forces acting on the head/disk interface? Is it possible to lubricate the FeSiN layer with today's high performance lubricants? Information about the film thickness of the lubricant is needed as well as degradation data and possible Lewis acid reactions. Has the layer a high corrosion resistivity? The research on these issues is currently ongoing and results will hopefully be available in the near future.

Bibliography

[1] D.B. Bogy et al., "Some tribology and mechanics issues for 100-Gb/in2 hard disk drive," *IEEE Trans. Magn.*, vol. 38, no. 5, pp. 1879-1885, 2002.

[2] T.W. Scharf, R.D. Ott, D. Yang, and J.A. Barnard, "Structural and tribological characterization of protective amorphous diamond-like carbon and amorphous CNx overcoats for next generation hard disks," *J. Appl. Phys.*, vol. 85, no. 6, pp. 3142-3154, 1999.

[3] K. Komvopoulos, "Head–disk interface contact mechanics for ultrahigh density magnetic recording," *Wear*, vol. 238, pp. 1-11, 2000.

[4] J. Robertson, "Amorphous carbon," *Adv. Phys.*, vol. 35, no. 4, pp. 317-374, 1986.

[5] J. Robertson, "Diamond-like amorphous carbon," *Materials Science and Engineering*, vol. R 37, pp. 129-281, 2002.

[6] A.C. Ferrari and J. Robertson, "Interpretation of Raman spectra of disordered and amorphous carbon," *Phys. Rev. B*, vol. 61, no. 20, p. 14095, 2000.

[7] K. Oguri and T. Arai, "Tribological properties and characterization of diamond-like carbon coatings with silicon prepared by plasma-assisted chemical vapor deposition," vol. 47, pp. 710-721, 1991.

[8] A. Erdemir, M. Switala, R. Wei, and P.J. Wilbur, "A tribological investigation of the graphite-to-diamond-like behavior of amorphous carbon films ion beam deposited on ceramic substrates," vol. 50, pp. 17-23, 1992.

[9] Y.W. Chung and W.D. Sproul, "Superhard coating materials," *MRS bulletin*, vol. 28, no. 3, pp. 164-165, 2003.

[10] K.E. Johnson, C.M. Mate, J.A. Merz, R.L. White, and A.W. Wu, "Thin-film media - Current and future technology," vol. 40, p. 511, 1996.

[11] D.J. Li, M.U. Guruz, C.S. Bhtia, and Y.W. Chung, "Ultrathin CNx overcoats for 1 Tb/inch(2) hard disk drive systems ," *Appl. Phys. Lett.*, vol. 81, no. 6, pp. 1113-1115, 2002.

[12] J. Zhang, "DLC review: Current techniques for diamond-like carbon synthesis," *Vacuum Technology and Coating*, vol. 5, no. 8, pp. 41-47, 2003.

[13] T.A. Yeh, C.L. Lin, J.M. Sivertsen, and J.H. Judy, "Friction, wear and elasto-plastic stress analysis of rf-sputtered carbon-nitrogen protective coatings for rigid magnetic storage disks," vol. 120, p. 314, 1993.

[14] H.O. Pierson, *Handbook of carbon, graphite, diamond and fullerenes: Properties, processing and applications*.: Noyes Publications, 1994.

[15] S. Aisenberg and R. Chabot, "Ion-beam deposition of thin films of diamond-like carbon," *J. Appl. Phys.*, vol. 42, pp. 2953-2958, 1971.

[16] J. Mort and F. Jansen, *Plasma deposited thin films*. Boca Raton: CRC press, 1986.

[17] H.R. Kaufman, "Technology of ion beam sources used in sputtering," *J.Vac. Sci. Technol.*, vol. 15, no. 2, pp. 272-276, 1978.

[18] B.K. Yen et al., "Effect of N doping on structure and properties of DLC films produced by plasma beam deposition," *IEEE Trans. Magn.*, vol. 37, no. 4, pp. 1786-1788, 2001.

[19] S. Anders, A. Anders, M.R. Dickinson, R.A. MacGill, and I.G. Brown, "S-shaped magnetic macroparticle filter for cathodic arc deposition," *IEEE trans. plas. sci.*, vol. 25, no. 4, pp. 670-674, 1997.

[20] R. Ohr, B. Jacoby, M.v. Gradowski, C. Schug, and H. Hilgers, "Analytical and functional characterization of ultrathin carbon coatings for future magnetic storage devices," *Surf. Coat. Technol.*, vol. 174-175, pp. 1135-1139, 2003.

[21] C.V. Raman and K.S. Krishnan, "A new type of secondary radiation," *Nature*, vol. 121, pp. 501-502, 1928.

[22] M. Neuhaeuser, H. Hilgers, P. Joeris, R. White, and J. Windeln, "Raman spectroscopy measurements of DC-magnetron sputtered carbon nitride (a-C:N) thin films for magnetic hard disk coatings," *Diamond and Related Materials*, vol. 9, pp. 1500-1505, 2000.

[23] S.S. Varanasi, J.L. Lauer, F.E. Talke, G. Wang, and J.H. Judy, "Friction and wear studies of carbon overcoated thin films magnetic sliders: application of Raman microspectroscopy," *Journal of Tribology*, vol. 119, p. 471, 1997.

[24] T.W. Scharf and I.L. Singer, "Thickness of diamond-like carbon coatings quantified with Raman spectroscopy," *Thin Solid Films*, vol. 440, pp. 138-144, 2003.

[25] G. Binnig, C.F. Quate, and Ch. Gerber, "Atomic force microscope," *Phys. Rev. Lett.*, vol. 56, no. 9, pp. 930-934, 1986.

[26] R.W. Carpick and M. Salmeron, "Scratching the surface: Fundamental investigations of tribology with atomic force microscopy," *Chem. Rev.*, vol. 97,

pp. 1163-1194, 1997.

[27] M.R. Koblischka et al., "Magnetic force microscopy applied in magnetic data storage technology," *Appl. Phys. A*, vol. 76, pp. 879-884, 2003.

[28] J.N. Israelachvili, *Intermolecular and surface forces, 2nd edition*. London: Academic Press, 1991.

[29] H.J. Butt, B. Cappella, and M. Kappl, "Force measurements with the atomic force microscope: Technique, interpretation and applications," *Surf. Sci. Rep.*, vol. 59, pp. 1-152, 2005.

[30] H. Hertz, "Über die Berührung fester elastischer Körper," *J. reine angewandte Matematik*, vol. 92, pp. 156-171, 1882.

[31] B.V. Derjagiun, V.M. Muller, and Y.P. Toprov, "Effect of contact deformations on the adhesion of particles," *J. Colloid Interface Sci.*, vol. 53, no. 2, pp. 314-326, 1975.

[32] K.L. Johnson, K. Kendall, and A.D. Roberts, "Surface energy and the contact of elastic solids," *Proc. R. Soc. Lond.A.*, no. 324, pp. 301-313, 1971.

[33] D. Tabor, "Surface forces and surface interactions," *J. Coll. Interf. Sci.*, vol. 58, no. 1, pp. 2-13, 1977.

[34] K.L. Johnson and J.A. Greenwood, "An adhesion map for the contact of elastic spheres," *J. Coll. Interf. Sci.*, vol. 192, pp. 326-333, 1997.

[35] J.A. Greenwood and J.B.P. Williamson, "Contact of nominally flat surfaces," *Proc. R. Soc. London Ser. A*, vol. 295, pp. 300-319, 1966.

[36] D. Tabor, *The hardness of metals*. Oxford: Oxford University Press, 1951.

[37] W.R. Chang, I. Etsion, and D.B. Bogy, "An elastic-plastic model for the contact of rough surfaces," *Journal of Tribology*, vol. 109, pp. 257-263, 1987.

[38] L. Kogut and I. Etsion, "A finite element based elastic-plastic model for the contact of rough surfaces," *Trib. Trans.*, vol. 46, no. 3, pp. 383-390, 2003.

[39] W.C. Oliver and G.M. Pharr, "An improved technique for determining hardness and elastic-modulus using load and displacement sensing indentation experiments," *J. Mater. Res.*, vol. 7, no. 6, pp. 1564-1583, 1992.

[40] C.M. Mate, G.M. McClelland, R. Erlandsson, and S. Chiang, "Atomic-scale friction of a tungsten tip on a graphite surface," *Phys. Rev. Lett.*, vol. 59, no. 17,

pp. 1942-1945, 1987.

[41] www.hysitron.com.

[42] Y. Matsuda et al., "Nano-hardness testing with ultrasonic excitation," *Wear*, vol. 259, pp. 1497-1501, 2005.

[43] G.M. Pharr, W.C. Oliver, and F.R. Brotzen, "On the generality of the relationship among contact stiffness, contact area, and elastic-modulus during indentation," *J. Mat. Res.*, vol. 7, no. 3, pp. 613-617, 1992.

[44] E. Boschung, M. Heuberger, and G. Dietler, "Energy dissipation during nanoscale indentation of polymers with an atomic force microscope," *Appl. Phys. Lett.*, vol. 64, no. 26, pp. 3566-3568, 1994.

[45] J.L Hay, M.E. O'Hern, and W.C. Oliver, "The importance of contact radius for substrate-independent property measurement of thin films," *Mat. Res. Soc. Symp. Proc.*, vol. 522, pp. 27-32, 1998.

[46] H. Kutomi, A. Daugela, W.W. Gerberich, H. Fujii, and T.J. Wyrobek, "Nanoscale friction reduction and fatigue monitoring due to ultrasonic excitation," *Trib. Int.*, vol. 36, pp. 255-259, 2003.

[47] C.M. Mate, Q. Dai, R.N. Payne, B.E. Knigge, and P. Baumgart, "Will the numbers add up for sub-7-nm magnetic spacings? Future metrology issues for disk drive lubricants, overcoats, and topographies," *IEEE Trans. Magn.*, vol. 41, no. 2, pp. 626-631, 2005.

[48] B.K. Yen et al., "Coverage and properties of a-SiNx hard disk overcoat," *Proceedings MMM Conference*, 2002.

[49] R.J. Waltman, B.K. Yen, and R.L. White, "The adhesion of monomolecular hydroxyl-terminated perfluoropolyether liquid films on the sputtered silicon nitride surface as a function of end group acidity and mobility," *Trib. Lett.*, vol. 20, no. 1, pp. 69-81, 2005.

[50] R.W. Carpick and M. Salmeron, "Scratching the surface: Fundamental investigations of tribology with atomic force microscopy," *Chem. Rev.*, vol. 97, pp. 1163-1194, 1997.

3 Lubricants for Hard Disk Drives

Liquid films at a solid-solid interface have been known for centuries to reduce friction and improve durability of two solid surfaces in contact with each other. Lubricants play a key role in the tribology of the head/disk interface [1]. As the slider flies over the disk intermittent contact can occur between the head and the disk which results in friction and wear. If contact occurs, the lubricant should exhibit a "self-healing" effect to quickly cover areas where lubricant was displaced. Lubricants have to be designed to bond to the surface and not spin off while the disk is spinning. In addition, the lubricant should not degrade over time during the lifetime of a hard drive. Perfluoropolyether (PFPE) lubricants have properties that make them well suited for use in hard disk drives [2].

3.1 Lubricant Chemistry and Properties

Different types of perfluoropolyether lubricants have been used since the early 1970s to improve the performance of the head/disk interface. Important properties are the following [3]:

- Low surface tension and good spread ability

- Hydrophobic properties

- High adhesion to the carbon surface

-Low degradation and vapor pressure

-Thermal and chemical stability

-Non-toxic and non-flammable

Different structures such as Fomblin Z^{TM}, Fomblin Y^{TM}, DuPont Krytox^{TM}, and Demnum^{TM}, where the notations Z-, Y-, K-, and D- indicate the type of perfluoropolyether, have been used as lubricants in hard disk drives. Fomblin Z and Y are random co-polymers prepared by photo-oxidation of tetrafluoroethylene and hexafluoropropylene, respectively, while Krytox and Demnum are synthesized via polymerization of perfluororpropylene oxide and trimethylene oxide, respectively. The lubricants are based on perfluoro-polyether (PFPE) which forms the so-called backbone. The PFPE backbone can be functionalized with polar end-groups which increase the bonding to the surface [4]. Their physical properties can be controlled by adjusting chain composition, molecular weight distribution and the nature of their end groups.

Fomblin Z^{TM} is widely used as the main PFPE backbone in the hard-disk drive industry today. It consists of a linear, random copolymer of perfluoromethylene-oxide and perfluoroethylene-oxide with an equivalent molar ratio (x/y as shown in Figure 3.1). Hydroxyl units are attached as the so-called end-group to increase adhesion between the carbon overcoat and the lubricant. The two most popular forms of lubricant are known as Z-Dol and Z-Tetraol. Figure 3.1 shows the chemical structure of Z-Dol and Z-Tetraol [5].

$$\text{Fomblin Z}^{\text{TM}}$$

Z-Dol: $\quad \overbrace{OH\text{-}CH_2}^{\text{hydroxylend-group}} \text{-} \underbrace{(CF_2\text{-}O)_x}_{\substack{\text{perfluoromethylene}\\\text{oxide}}} \text{-} \overbrace{(CF_2CF_2O)_y}^{\text{perfluoroethylene-oxide}} \text{-} CF_2CH_2\text{-}OH$

Z-Tetraol: $\quad \underset{\underset{OH}{|}}{HO\text{-}CH_2CHCH_2}O \text{-} CH_2\text{-} CF_2O \text{-} \text{Fomblin Z}^{\text{TM}}\text{-} CF_2CH_2OCH_2\underset{\underset{OH}{|}}{CHCH_2}\text{-}OH$
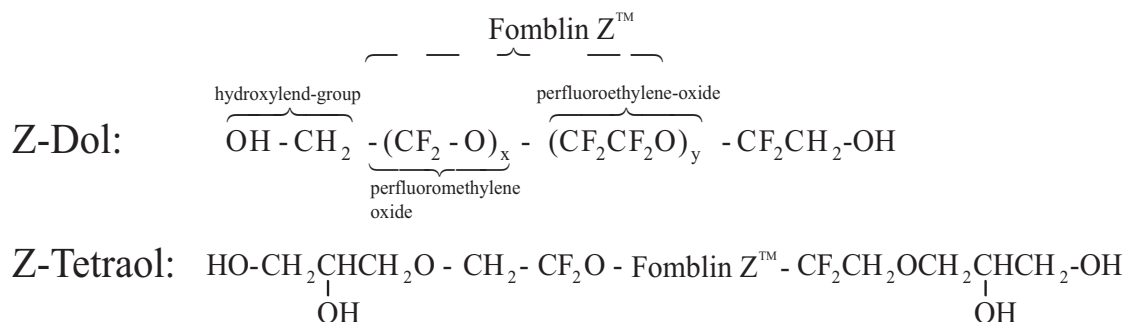
Figure 3.1: Chemical structure of Z-Dol and Z-Tetraol.

The molecular weight (MW) of the molecules in PFPE lubricants has a distribution around an average value. Different molecular weight can be created by changing the number of perfluoromethylene-oxide (x) and perfluoroethylene-oxide (y), which results in a different length of the molecule. For example, Z-Dol 4000 (MW: 4000 amu) has a length of approximately 14 nm, while Z-Dol 2000 (MW: 2000 amu) has a length of approximately 7 nm [6]. PFPEs have a diameter between 0.7 nm and 0.8 nm. Different molecular weight changes the chemical and mechanical properties of the PFPE lubricant. Molecules with a high MW show increased stiction at the contact interface and have a decreased vapor pressure, while molecules with low MW show an increase in mobility and vapor pressure, leading to unwanted evaporation from the disk [7]. Therefore, the molecular weight distribution (also called polydispersity) of the lubricant must be controlled via fractionation to produce a lubricant with homogeneous molecular weight. The degree of the distribution is described by the polydispersity index (PDI), which is defined as the ratio of the

weight- and number- average of molecular weights. Z-Dol and Z-Tetraol lubricants have a PDI of typically 1.2 to 1.4 [8].

The PFPE lubricant is applied to the surface by dip-coating the disk into a lubricant-solvent bath. The lubricant thickness can be controlled by the pull-rate and/or the concentration (~0.1 wt.%) of the PFPE lubricant in the solvent [9]. The solvents are hydro-fluoroether such as 3M's HFE solvent ($C_4F_9OCH_3$) or DuPont's Vertrel-XF ($CF_3CHFCHFCF_2CF_3$) [10]. The choice of the type of solvent, lubricant, and concentration in the solution is critical since it influences the adsorption of the PFPE lubricants onto the carbon surface [8]. Interaction between the lubricant and the solvent, which is driven by the molecular weight and the interaction of the polar end groups, can also impact the lubricant uniformity and thickness. However, the solvent acts as a carrier of the lubricant to the disk surface, and once it is fully evaporated it should not impact the tribological performance of the head disk interface. The thickness of the lubricant that is left on the disk surface can be varied by different concentrations of the PFPE in the solvent and by different pull-rates of the disk from the solution. Figure 3.2 shows the lubricant thickness as a function of pull-rate and two different Z-Dol (MW 2000) concentrations of 0.05 and 0.09 wt% in the solution.
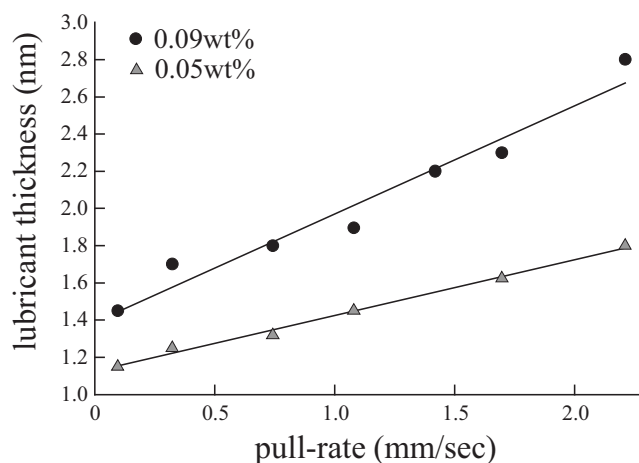
Figure 3.2: Lubricant thickness as a function of drain speed for two different Z-Dol (MW 2000) concentrations (●,▲) (Courtesy of Dr. Ho-Jeong Kang)

3.1.1 PFPE Lubricant/Carbon Interface

Physical attractive forces between the perfluoropolyether lubricant and the carbon surface are based on van der Waals forces which result in dispersive interactions. Furthermore, polar interaction between the functionalized OH-end groups of the PFPE lubricant and the polar sites of the carbon surface form hydrogen bonding and strong acid-base bonds. Therefore, the "bonding" character of the polar end-groups to the carbon overcoat and the weak adhesion and diffusive properties of the backbone of the lubricant has to be tuned for best performance of the head/disk interface [11]. Figure 3.3 shows the different interaction strength of PFPE's with various polar end groups.

molecular structure:		interaction type:
Z - PFPE back bone		weak: dispersive
Z-Dol - one OH-group on each end group		dispersive + polar
Z-Tetraol with two OH-groups on each end group		dispersive + strong polar
ZTMD with multiple OH-groups along the PFPE chain		dispersive + polar + polar along the chain

Figure 3.3: Structure and interaction of PFPE lubricants with the carbon surface (after [**11**])

The interaction strength between PFPE lubricant and the carbon overcoat is strongly depended on temperature. The lubricant/carbon interaction can be increased by annealing of the lubricant end-groups at elevated temperatures. Thus, the bonding of the lubricant onto the disk substrate is increased. The bonding ratio, which is the ratio between the bonded lubricant divided by the total applied lubricant provides information on how much lubricant is bonded. The bonding ratio has a balance between 60% and 80% depending on the lubricant and its end-group configuration. Annealing at elevated temperature minimizes evaporation and spin-off of the PFPE lubricant from the disk. However, it reduces the mobility of the lubricant which reduces the durability of the head-disk interface.

In addition, the carbon thickness on the magnetic disk can influence the lubricant properties. If the thickness of the carbon overcoat is reduced to less than 3 nm, the lubricant film can interact with the oxide groups formed by the underlying magnetic film. This results in an increase in lubricant thickness as observed by Waltman et al. [**12**].

The lubricant thickness on today's magnetic disks is on the order of one molecular layer of the PFPE lubricant, between 1.2 nm and 1.8 nm. The mass of the lubricant on a disk is less than one micro-gram. In the following, challenges of the lubrication for hard disks and possible solutions are discussed.

3.1.2 Lubrication

Lubrication is divided in three regimes, boundary, hydro-dynamic and mixed lubrication. Figure 3.4 shows the three regions in a so-called Stribeck curve [**13**]. The friction coefficient is shown as a function of viscosity, sliding speed, and load. The initial flat section of the curve represents boundary lubrication, where interfacial contact occurs at the interface [**14**]. Boundary lubrication shows the highest friction coefficient. The following declining section indicates mixed lubrication, in which the load across the contact is carried partly by contact between asperities on the surfaces, and partly by the lubricating fluid. The rising trend beyond the friction coefficient minimum of the curve indicates full fluid-film lubrication in which the load across the contact is supported entirely by viscous shear forces in the lubricant. Surface asperity contact is absent.
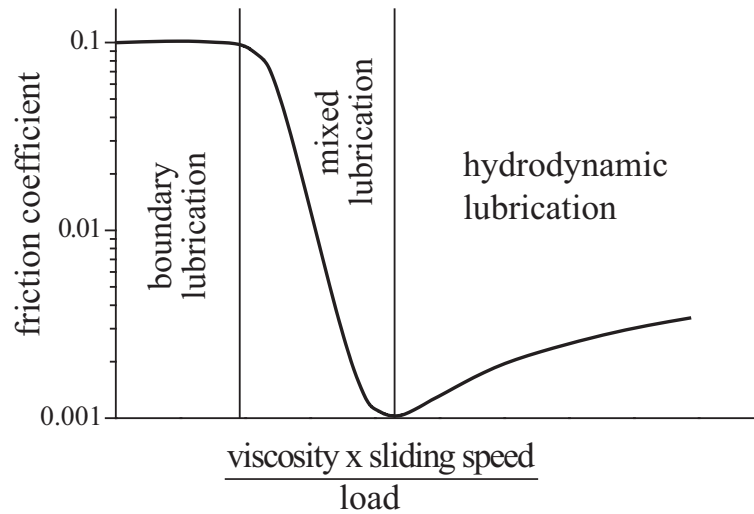
Figure 3.4: Typical Stribeck curve (after [**14**])

PFPE lubricants on carbon overcoats have a thickness on the order of one molecular layer. The viscosity and dynamic properties of a PFPE lubricant at that thickness are different compared to the bulk properties due to the strong interaction with the solid surface. The films become solid-like and boundary lubrication as well as mixed lubrication occur during contact between the slider and the lubricated disk [**15**]. Mixed lubrication is caused by the mobile fraction of the lubricant on the disk. When a slider contacts the disk lubricant will get displaced, and the mobile lubricant will slowly move into the depleted area.

3.1.3 Lubricant Engineering

The engineering of efficient lubrication systems is crucial, and a better understanding of these lubricant-carbon interfacial interactions is needed. As described earlier the performance of the lubricant on the disk surface depends on the ratio of the bonded to the mobile fraction. The lubricant needs to be engineered in a way that negative lubrication effects in the head/disk interface, as described in the following, are minimized.

Z-Tetraol has a bonding ratio of approximately 80% due to its four OH-groups and the increased bonding interaction with the disk surface. Z-Dol on the other hand, has only two OH-groups and a bonding ratio of approximately 50% [16]. Thus Z-Dol has a higher mobility than Z-Tetraol due to the increased non-bonded fraction of molecules. Even though higher mobility of a lubricant is desirable for "self-healing" purposes, high mobility can cause increased stiction between the slider and the disk, lubricant transfer to the slider, and spin-off of lubricant at high velocities. Intermittent slider-disk contact can increase lubricant transfer to the slider [17], which increases adhesion and consequently may result in failure of the head disk interface.

As the flying height decreases, intermolecular forces influence the interaction between the lubricant and the slider. Intermolecular forces at flying heights below 5nm can destabilize the slider air-bearing and the slider shows vibrational motion [18]. For example, van der Waals interaction in combination with air shear stress and air bearing pressure cause lubricant modulation or lubricant motion on the disk. It has been demonstrated [19] that so-called "moguls" and "ripples" occur in the lubricant

film on a disk surface. Moguls are correlated with disk waviness, i.e., due to air shear, lubricant depletes on the upward part of the waviness of the disk and accumulates in the downward slopes [19]. The disk waviness is a long range surface roughness with heights on the order of micro meter that, if small enough, can influence the flyability of the slider. The ripples correlate with the air-bearing frequencies and are caused by air shear effects. One solution to decrease moguls and ripples on the disks surface is to reduce the disk waviness and the thickness of the lubricant, respectively.

3.1.3.1   Lubricant Transfer from the Disk to the Slider

The presence of lubricant on a slider has been described by evaporation/condensation mechanisms due to the low molecular weight parts [20] and vapor pressure of the PFPE lubricant [21]. In addition to this gas transfer mechanism, a mechanical mechanism of lubricant transfer can occur during contact. The condensation mass flux R_{cond} is a measure for the lubricant flow (in gas form) from the disk to the slider [21]

$$R_{cond} = P_0 \sqrt{\frac{M_n}{2\pi RT}} \cdot \exp\left(-\frac{\Pi(h)M_n}{\rho RT}\right) \tag{3.1}$$

where P_0 is the bulk vapor pressure, M_n is the molecular weight of the PFPE, R is the gas constant, T is the absolute temperature, ρ is the lubricant density, and $\Pi(h)$ is the disjoining pressure at a certain lubricant film thickness h. The first term is the Langmuir equation for the bulk liquid and is modified for surfaces effects by the

second term. The second term is governed by the disjoining pressure (which is discussed at the end of this chapter) to retain lubricant on the disk. Marchon et al. predicted by using numerical simulations that the net accumulation of lubricant on the slider decreases exponentially with increasing molecular weight of the lubricant.

Due to high shear stresses in the slider air bearing, the lubricant accumulates behind the sliders trailing pad which is closest to the disk surfaces. Thus, the lubricant at the corner of the trailing pad and the disk surface causes high lubricant-lubricant adhesion that highly affects the head-disk interface [**22**]. In addition, at contact, lubricant can be picked up from the disk or re-deposited on the disk, which causes lubricant modulation on the disk surface.

3.1.3.2   Dewetting of PFPE Films

Dewetting in a molecularly thin PFPE lubricant occurs when the film thickness increases locally above a critical value. The film becomes unstable and small droplets can form on the surface [**23**]. The formation of lubricant droplets can drastically influence the head/disk interface. The critical film thickness at which dewetting occurs is linearly dependent on the molecular weight of the lubricant. Waltman et al. [**23**] have shown that the critical dewetting thickness for Z-Dol with a molecular weight of 1000 amu is on the order of 1nm, while for 4000 amu it is on the order of 3nm. Typical dewetting occurs at thicknesses that are above one molecular layer of the PFPE lubricant and the amount that is applied in excess of the critical thickness is contributing to the formation of droplets. Today's disks are coated with a lubricant

film thickness that is well below the critical dewetting thickness. However, ripples and moguls can be on the order of the critical dewetting thickness and cause instability in the lubricant film. In addition, changes in the carbon surface chemistry and additives in the lubricant can influence the critical dewetting thickness as well.

3.1.3.3 PFPE Lubricant Degradation

Formation of Lewis acids, which are in general metal oxides and halides, have been found to be the predominant degradation mechanisms of disk surfaces [**24**]. The materials used for slider body and the disk substrate, Al_2O_3-TiC and Al_2O_3, respectively, are the origin for the formation of Lewis acid, e.g. $AlCl_3$. Lewis acid mainly forms at the surface of the slider. When lubricant is transferred to the slider, intramolecular disproportionation reactions [**18**] of the PFPE lubricant at the Lewis acid occur as shown in Figure 3.5. The reaction of the oxygen with a CF_2-unit of the PFPE lubricant results not only in fragmentation of the PFPE chains but also generates fluorocarbonyl end-groups. The Lewis acid is acting as a catalyst in this reaction. In addition, fluorocarbonyl end-groups (CF_3), once in contact with moisture from the humidity, convert into strong fluorinated carboxylic acids [**25**]. Hence, the PFPE is reduced to a monomer and/or low molecular weight oligomer with lower vapor pressure. As a result, the fragmented PFPE lubricant evaporates, which can lead to a complete loss of lubrication on the magnetic disk.

$$R-O-CF_2-O-CF_2-R$$

Lewis Acid $\rightarrow$ $R-O-CF_3 + F-C-R$
$\underset{O}{\overset{\|}{}}$
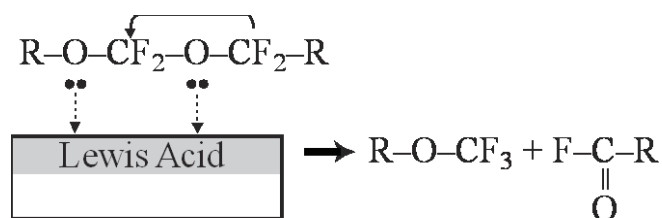
Figure 3.5: Lewis acid intramolecular disproportionation reaction of PFPE's (after

[**18**])

3.1.4 Additives in PFPE Lubricants

Over the last decade, additives such as X1-P or additional hybrid end-group structures like A20H, C2, and ZTMD molecules have been investigated to improve the lubricant performance of PFPEs [**26**], [**27**], [**28**], [**29**], [**30**]. Additives can decrease lubricant mobility. Hence, the molecular weight can be further reduced below 2000 amu without evaporation of the lubricant. In addition, additives prevent degradation via catalytic reactions (e.g. Lewis acid) of the PFPE.

An additive that works well with the Fomblin Z^{TM} lubricant system and has highly improved the lubrication performance is the so-called X-1P molecule [**27**]. X-1P is a partially fluorinated hexaphenoxy cyclotriphosphazene. Its chemical structure is shown in Figure 3.6. Mate et al. have found that the X-1P molecules position themselves between the carbon overcoat and the PFPE lubricant. X-1P prevents the PFPE lubricant from bonding to open sites on the carbon surface, therefore, increasing the mobility of the lubricant. In addition, a lower surface energy of the lubricant film was found [**28**]. X-1P has a higher surface energy (35 mJ/m^2) compared to that of a

PFPE (15-25 mJ/m^2) and therefore, it is energetically favorable for X-1P to cover the high energy surface sites of the carbon overcoat (40-50 mJ/m^2). The PFPE lubricant attaches to the X-1P layer with at a lower surface energy. Therefore, the overall surface energy is decreased compared to a solely PFPE lubrication.

It was found that X-1P acts as a Lewis base, which in turn blocks Levis acid sides by an acid-base reaction and prevents lubricant degradation [30]. The molecules passivate the Lewis acid sites, preventing catalytic decomposition of the PFPE lubricant. Adding only a small fraction between 1-10 wt% of X-1P to the lubricant solution can almost eliminate lubricant degradation due to Lewis acids [31].
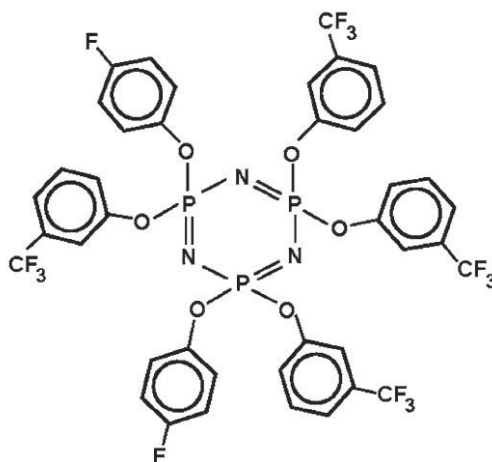
Figure 3.6: Chemical structure of X1-P

In the last decade, researchers tried to link the outstanding properties of X-1P additives with Fomblin Z^{TM} type perfluoropolyether lubricants by terminating the

backbone with the X1P cyclotriphosphazene group [**32**]. The chemical structure of the X-1P - PFPE hybrids known as A20H and C2 are shown in Figure 3.7. In C2 the pentaphenoxy-group of A20H was replaced by a trifluoro-ethoxy group to decrease the molecular weight of A20H. The Z backbone PFPE is shown in the right hand lower corner. Both lubricant additives can be mixed with both lubricant systems, Z-Dol and Z-Tetraol to improve lubricant performance. However, only A20H features an increased attractive interaction with the carbon overcoat of the disk [**30**]. In addition, the bonding characteristics of A20H can be enhanced by using ultraviolet (UV) light for curing, while C2 is lacking these properties. Both additives show a decrease in degradation of the PFPE due to their Lewis base end-groups, which neutralize Lewis acids on the disk and slider surface.
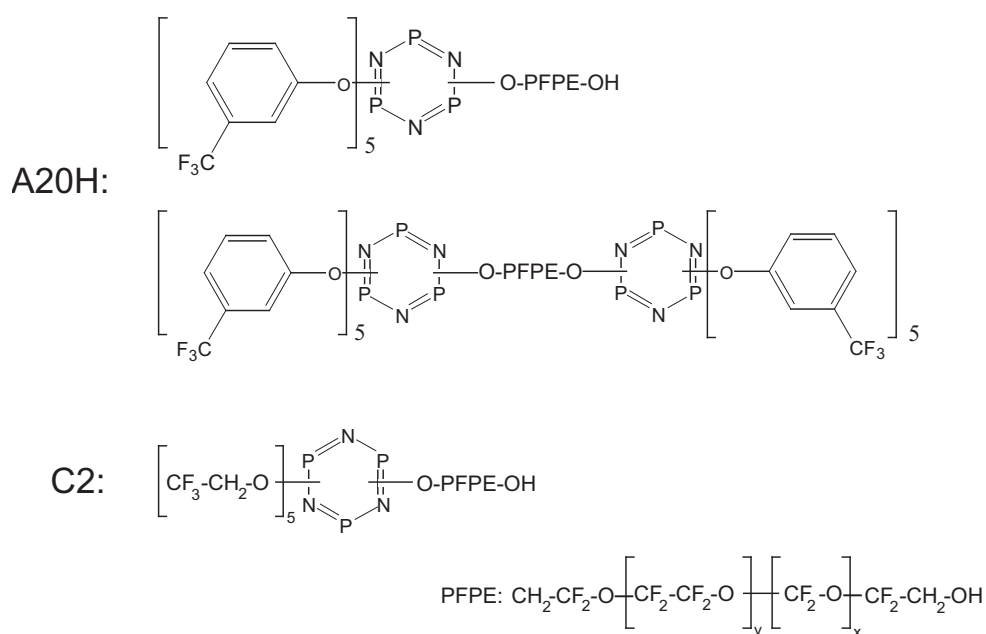
Figure 3.7: Chemical structure of A20H and C2 terminated onto a PFPE lubricant.

In recent years, Fomblin multidentate lubricants (ZTMD) have been developed, where additional functional hydroxyl groups are introduced in the middle of the PFPE chain [**33**]. This new lubricant can sustain higher air shear stress due to increased interaction with the carbon surface. ZTMD shows higher hydrophobicity and lower surface energy. Thus, adhesive interactions with the slider are decreased. In addition, due to the bonding of sections of the backbone of the lubricant to the carbon surface (as shown in Figure 3.3), the lubricant lays flat on the surface. As a result, reduction in clearance between the slider and the disk surface can be achieved [**34**]. In addition lubricant modulation or rippling is reduced with sufficient reflow characteristics. The chemical structure of ZTMD with eight hydroxyl groups is shown in Figure 3.8. The backbone is a Fomblin Z structure with a molecular weight of approximately 1000 amu on each side of the chain.

Figure 3.8: Chemical structure of ZTMD

3.2 Characterization Techniques for PFPE Lubricant Systems

The properties of molecularly thin lubricant films on magnetic hard disks can be dramatically different from those corresponding to bulk liquids. Different techniques have been developed to evaluate the lubricant-carbon interaction in the head/disk interface. The two most powerful instruments are described in more detail.

3.2.1 Surface Reflectance Analysis

Surface reflectance analysis (SRA) is an optical inspection technique to determine the composition and thickness uniformity of thin films on surfaces [35], [36]. The instrument is based on the principle of ellipsometry, where a laser light source is used to scan over the sample surface to measure changes in the phase and intensity of the beam after it is reflected form the sample surface (Figure 3.9). The laser light is circularly polarized with a linear polarizer and a quarter wave plate. While a reference beam is generated, a primary beam is focused on the sample surface. The properties and the thickness of the surface material change the parameters of the polarized light that is reflected. The fraction of the incident beam power that is reflected from the interface is given by the reflection coefficient R. The reflected light is passed through an analyzer to separate the light which is parallel polarized (P-polarized) from the light that is perpendicular polarized (S-polarized).
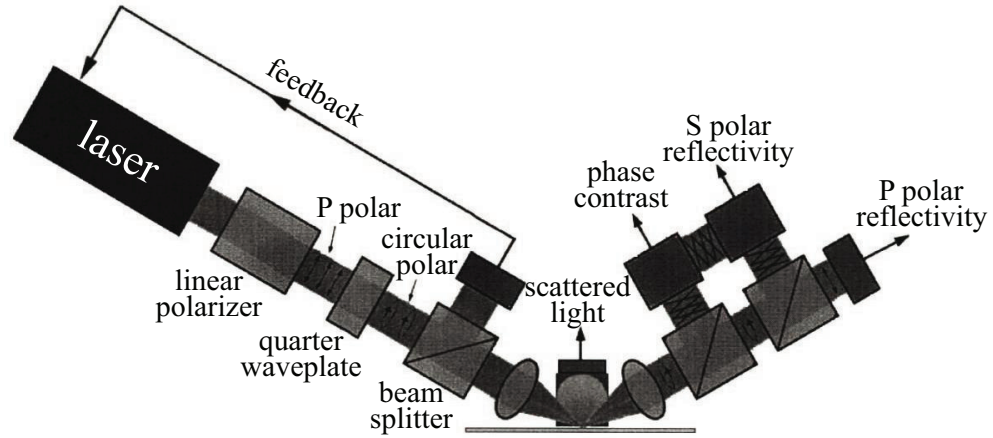
Figure 3.9: Schematic of the SRA instrument (after: [**37**])

The theory of Fresnel's equations relates the parameters of polarized light with the material properties of the measured surface, in particular the refractive index. These equations describe the behavior of light when moving between media of different refractive indices n. The reflection coefficient R for P-polarized light can be calculated as follows

$$R_P = \left[\frac{\tan(\theta_t - \theta_i)}{\tan(\theta_t + \theta_i)}\right]^2 = \left[\frac{n_1 \cos(\theta_t) - n_2 \cos(\theta_i)}{n_1 \cos(\theta_t) + n_2 \cos(\theta_i)}\right]^2 = \left[\frac{n_1\sqrt{1 - \left(\frac{n_1}{n_2}\sin\theta_i\right)^2} - n_2 \cos(\theta_i)}{n_1\sqrt{1 - \left(\frac{n_1}{n_2}\sin\theta_i\right)^2} + n_2 \cos(\theta_i)}\right]^2 \quad (3.2)$$

where θ_i is the incident angle of the light beam onto the surface and n_1/n_2 are the refractive indices of the materials (in this case air and disk surface). If the incident light is S-polarised, R is given by

$$R_S = \left[\frac{\sin(\theta_t - \theta_i)}{\sin(\theta_t + \theta_i)}\right]^2 = \left[\frac{n_1 \cos(\theta_i) - n_2 \cos(\theta_t)}{n_1 \cos(\theta_i) + n_2 \cos(\theta_t)}\right]^2 = \left[\frac{n_1 \cos(\theta_i) - n_2 \sqrt{1 - \left(\frac{n_1}{n_2}\sin\theta_i\right)^2}}{n_1 \cos(\theta_i) + n_2 \sqrt{1 - \left(\frac{n_1}{n_2}\sin\theta_i\right)^2}}\right]^2 \quad (3.3)$$

Using Fresnel's equation, one can show that if the film thickness of an organic material (carbon overcoat or lubricant) becomes thicker, the reflectivity of the P-polarized light will increase while the reflectivity of the S-polarized light will decrease.

In addition, the relative phase shift of the S and P polarized light is determined. Therefore, four parameters, i.e., P polar reflectivity, S polar reflectivity, phase contrast, and light scattering are simultaneously measured. In principle, the SRA is a high speed ellipsometer, which gives film thickness information of the lubricant film and carbon overcoat at a high vertical resolution (less than 0.1 nm) by measuring the polarization state of light reflected from the disk surface [37]. The instrument is used to measure the distribution of lubricant, wear of the carbon film, and due to the scattered light detection, detects debris that is accumulating on the disk.

Another system that uses a similar technique as the surface reflectance analyzer is the Candela™ Optical Surface Analyzer (OSA) [38]. The OSA system is an industrial tool for automatic, non-destructive defect, scratch and ridge inspection,

particle and stain inspection as well as waviness analysis. The determination of film thickness uniformity with a noise floor of 0.05 nm is possible [**39**]. It is able to simultaneously measure surface reflectivity and topography by combining scatterometry, ellipsometry, reflectometry, and topographical analysis. A second laser path adds sensitivity to micro-scratches, regardless of orientation.

3.2.2 Contact Angle Goniometry

Contact angle goniometers are used to measure the static contact angle to determine surface tension of a liquid and the surface energy of a surface [**40**], [**41**]. A liquid droplet with known surface energy is placed on a surface via a motorized syringe. Depending on the surface energy of the droplet and the surface, the droplet is spreading on the surface or "balls" up in a half-dome shape. The instrument consists of an arrangement of a lens and a CCD camera to capture the image of the droplet as shown in Figure 3.10. From this image the contact angle can be determined from the shape using computer software.

The contact angle θ_C is the angle formed by a droplet at the boundaries between the liquid, gas, and solid. The contact angle depends on the interfacial tensions between the liquid and gas (LG), the solid and liquid (SL), and the solid and gas (SG) as shown in [**42**]. Young's equation can be used to determine the surface energies with the contact angle method [**43**]

$$\gamma_{LG} \cos\theta_{C} = \gamma_{SG} - \gamma_{SL} \tag{3.4}$$

where γ_{SG} is the free energy of the surface, γ_{SL} is the solid-liquid interfacial energy and γ_{LG} is the free surface energy of the reference liquid.
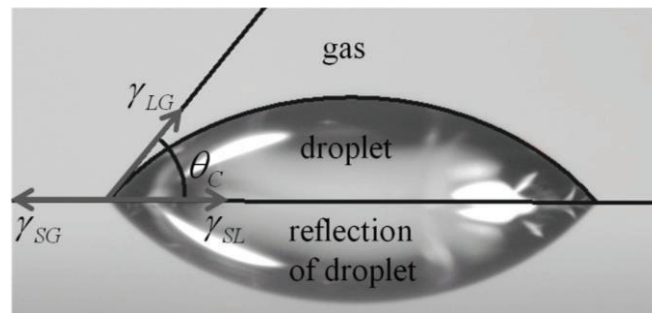
Figure 3.10: Contact angle measurement for determination of surface energy

In chapter 7 a new method to measure surface energy on the nano-scale using AFM force-displacement curves is presented.

3.3 Surface Energy and Surface Tension

The surface energy is the work required to increase the surface area of a substance ,i.e.,

$$\gamma = \left(\frac{dG}{dA}\right) \tag{3.5}$$

where G is the Gibbs free energy and A is the surface area. Surface energy quantifies the disruption of intermolecular bonds that occur when a surface is created [42]. Figure 3.11 shows a schematic of molecule interaction near a surface. Molecule (1), which resembles a molecule in the bulk of the material, feels attractive cohesive forces from all sides, which average to a net force equal to zero. At the surface of the liquid, the molecule (2) is not attracted as intensely by the molecules in the neighboring medium (e.g. vacuum, air or another liquid) and interacts with molecules of the liquid only on one side. Hence, it is pulled back into the surface, creating a tension that pulls the liquid surface flat. Therefore, the surface energy of liquids is also called surface tension.
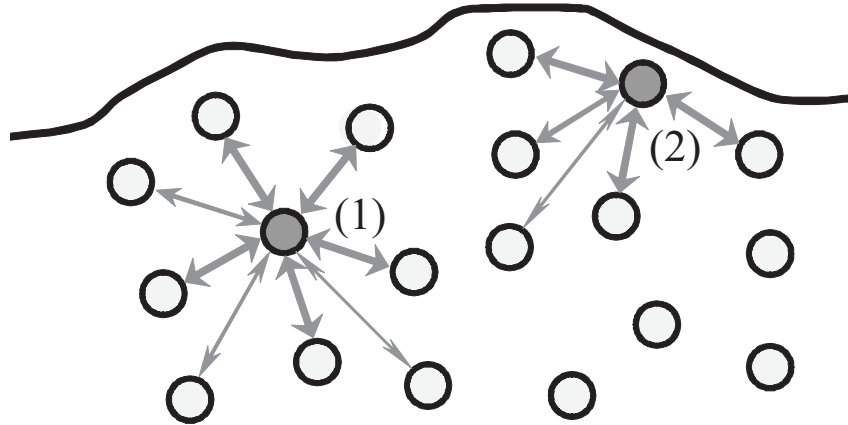
Figure 3.11: Schematic of molecule interaction in the bulk (1) and near the surface (2).

At a liquid-solid interface, if the adhesive forces between the liquid and the solid are stronger than the cohesive forces between the molecules of the liquid, wetting of the

surface occurs and the lubricant is spreading. However, if the cohesive forces are stronger than the adhesive forces, the liquid molecules form single droplets on the surface and do not wet the surface. In addition, high surface energy materials rearrange or react with molecules from the atmosphere to lower their surface energy by processes known as passivation or adsorption. As an example, the high adhesive forces of the carbon overcoat are lowered by applying a lubricant with low cohesive interaction forces.

3.3.1 Surface Energy Determination

In order to obtain the individual surface energies and not the difference $\gamma_{SG} - \gamma_{SL}$ as shown in Eq. (3.4), an additional relation is required. The Dupré equation states that [44]

$$\gamma_{SL} = \gamma_{SG} + \gamma_{LG} - W_{adh} \tag{3.6}$$

where $W_{adh} = 2\sqrt{\gamma_{SG}\gamma_{LG}}$ is the work of adhesion per unit area. The work of adhesion comes from the interaction between the liquid and solid molecules or atoms. There are different types of interactions, e.g. dispersive (van der Waals interactions), polar (e.g. hydrogen-bonding, dipole-dipole interaction, or covalent bonding), electronic, and magnetic interactions. In the head/disk interface the main interactions between the lubricant and the carbon overcoat are of dispersive and polar nature. Different liquids can be used to determine the dispersive γ^d and polar γ^p component of surface

energy. The surface energies of the solid and the liquid is a combination of the dispersive and the polar component and can be written as

$$\gamma_{SG} = \gamma_{SG}^d + \gamma_{SG}^p \quad and \tag{3.7}$$

$$\gamma_{LG} = \gamma_{LG}^d + \gamma_{LG}^p \tag{3.8}$$

respectively.

The dispersive surface energy component can be determined by using liquids that only interact via dispersive forces with the sample surface, such as alkane-hydrocarbons (e.g. hexadecane). Using Eqs. (3.4) and (3.6) one can calculate the dispersive surface energy of the solid for a solely dispersive system ($\gamma^p = 0$) if the dispersive surface energy of the reference liquid is known [45]

$$\gamma_{SG}^d = \frac{\gamma_{LG}^d (1 + \cos\theta)^2}{4} \tag{3.9}$$

Owens and Wendt [46] proposed a more general form of Eq. (3.6) which includes both dispersive (d) and polar (p) components

$$\gamma_{SL} = (\gamma_{SG}^d + \gamma_{SG}^p) + (\gamma_{LG}^d + \gamma_{LG}^p) - 2\sqrt{\gamma_{SG}^d \gamma_{LG}^d} - 2\sqrt{\gamma_{SG}^p \gamma_{LG}^p} \tag{3.10}$$

Introducing this form into Young's equation (Eq. (3.4)), one can determine the polar component of the solid surface using a reference liquid with known dispersive and polar component such as water ($\gamma_{LG}^d = 21.8\,mJ/m^2$, and $\gamma_{LG}^p = 51.0\,mJ/m^2$)

$$\gamma_{SG}^p = \frac{(\gamma_{LG}(1 + \cos\theta))^2 - 4\gamma_{SG}^d \gamma_{LG}^d}{4\gamma_{LG}^p} \tag{3.11}$$

The dispersive component of the solid γ_{SG}^{d} can be calculated using Eq. (3.9). Therefore, the dispersive and polar surface energy components of a surface and a solid coated with a molecularly-thin film can be determined. For a carbon surface lubricated with PFPE, one can specifically determine the surface energy components as a function of lubricant thickness, lubricant bonding ratio, and changes of the carbon overcoat.

3.4 Disjoining Pressure

When the lubricant film gets damaged or depleted during contact between the slider and the disk, lubricant can spread into the damaged areas to restore the film. In the macroscopic regime, surface tension gradient and gravity are the driving forces for spreading of a lubricant [47]. However, the spreading of liquid films in the microscopic regime is fundamentally different. The driving force for spreading of molecularly-thin films on solid surfaces (such as the PFPE films on hard disks) is a gradient in the disjoining pressure [48]. First introduced by Derjaguin [49], the disjoining pressure Π is defined as the negative derivative of the Gibbs free energy G with respect to film thickness

$$\Pi(h) = -\frac{dG}{dh} \tag{3.12}$$

In a liquid film, a pressure can be generated by a change in the thickness of the film. This pressure is greater than the pressure in the bulk phase of the same liquid. The pressure will act as a force per unit area to increase or decrease the film thickness of

the liquid on the solid surface depending whether the pressure is attractive or repulsive [**48**]. If the interactions between the lubricant molecules and the solid surface are stronger than the interactions between the lubricant molecules themselves, $\Pi > 0$ and consequently spreading of the lubricant occurs. However, if $\Pi < 0$, the liquid can lower its free energy and dewetting occurs [**50**]. Tabor and Winterton [**51**] found that the disjoining pressure for a dispersive liquid on a solid surface is governed by van der Waals interactions

$$\Pi(h) = -\frac{A}{6\pi h^3} \tag{3.13}$$

where A is the Hamaker constant. The disjoining pressure $\Pi(h)$ has three components: I) $\Pi^d(h)$ is a result of van der Waals forces acting between the film and substrate, II) $\Pi^e(h)$ an ionic, electrostatic component, and III) $\Pi^p(h)$ a polar or structural component, a consequence of different structure of the molecules in the thin film compared to the bulk lubricant [**52**].

In the case of lubricants with polar end-groups (e.g. Z-Dol, Z-Tetraol) a more complicated expression is needed to account for the interaction of the end groups. This expression can be found empirically. In this case, the disjoining pressure can be related to the surface energy components, γ^d and γ^p as the negative derivative with respect to film thickness [**45**]

$$\Pi(h) = \Pi^d(h) + \Pi^p(h) = -\frac{d\gamma^d}{dh} + \frac{d\gamma^p}{dh} \tag{3.14}$$

where $\Pi^d(h)$ is the dispersive component and $\Pi^p(h)$ is the polar component of the disjoining pressure. It has been proven [53], [54] that for a lubricant film on a solid surface the dispersive part of the surface energy that is in excess to the bulk value $\Delta\gamma^d(h)$ can be described by [45]

$$\Delta\gamma^d(h) = -\frac{1}{12\pi}\frac{A^*}{(d_0 + h)^2} \tag{3.15}$$

where A^* is the "effective" Hamaker constant and d_0 is a constant. The effective Hamaker constant is defined as the difference between the Hamaker constants describing the van der Waals interactions between the solid-liquid and the liquid-liquid interaction pairs, $A^* = A_{SL} - A_{LL}$ [42].

The combination of a perfluoropolyether lubricant with a carbon coated magnetic hard disk is critical for the head/disk interface performance. The lubricant wets uniformly the entire surface, quickly flows into depleted areas to heal defects in the coverage of the surface and has low vapor pressure. These characteristics are related to the disjoining pressure, which contains contributions from van der Waals, polar, hydrogen-bonding, and structural forces. As an example, the restoration of a defect in lubricant coverage will occur if the disjoining pressure is positive $\Pi(h) > 0$, and for the lubricant to be stable $\frac{\partial\Pi(h)}{\partial h} < 0$. In summary, disjoining pressure provides a measure of the wettability of lubricant on a substrate as well as the lubricants thickness dependence as a function of the lubricant-surface interactions.

Bibliography

[1] B. Bhushan, *Tribology and mechanics of magnetic storage devices*. New York: Springer, 1996.

[2] H. Liu and B. Bhushan, "Nanotribological characterization of molecularly thick lubricant films for applications to MEMS/NEMS by AFM," *Ultramicroscopy*, vol. 97, pp. 321-340, 2003.

[3] R.J. Waltman and G.W. Tyndall, "Lubricant and overcoat systems for rigid magnetic recording media," *J.Magn. Soc. Japan*, vol. 26, no. 3, pp. 97-108, 2002.

[4] T.E. Karis, B. Marchon, D.A. Hopper, and R.L. Siemens, "Perfluoropolyether characterization by nuclear magnetic resonance spectroscopy and gel permeation chromatography," *J. Fluor. Chem.*, vol. 118, pp. 81-94, 2002.

[5] A.M. Scarati and P. Caporiccio, "Frictional behaviour and wear resistance of rigid disks lubricated with neutral and functional perfluoropolyethers," *IEEE Trans. Magn.*, vol. 23, pp. 106-108, 1987.

[6] G.W. Tyndall, P.B. Leezenberg, R.J. Waltman, and J. Castenada, "Interfacial interactions of perfluoropolyether lubricants with magnetic recording media," *Trib. Lett.*, vol. 4, pp. 103-108, 1998.

[7] T. Nakakawaji et al., "Ultrafiltered perfluoropolyether lubricant under molecular weight distribution control," *Tribol. Trans.*, vol. 43, no. 4, pp. 671-676 , 2000.

[8] R.J. Waltman, G.W. Tyndall, G.J. Wang, and H. Deng, "The effect of solvents on the perfluoropolyether lubricants used on rigid magnetic recording media," *Tribology Letters*, vol. 16, no. 3, pp. 215-230, 2004.

[9] C. Gao, Y.C. Lee, J. Chao, and M. Russak, "Dip-coating of ultra-thin liquid lubricant and its control for thin-film magnetic hard disks," *IEEE Trans. Magn.*, vol. 31, no. 6, pp. 2982-2984, 1995.

[10] K.E. Johnson, C.M. Mate, J.A. Merz, R.L. White, and A.W. Wu, "Thin-film media - Current and future technology," vol. 40, p. 511, 1996.

[11] M.S. Jhon and H.J. Choi, "Lubricants in future data storage technology," *J. Ind. Eng. Chem.*, vol. 7, no. 5, pp. 263-275, 2001.

[12] R.J. Waltman et al., "The effect of carbon overcoat thickness on the Zdol boundary lubricant film," *Trib. Lett.*, vol. 12, no. 1, pp. 51-60, 2002.

[13] R. Stribeck, "Characteristics of plain and roller bearings," *Zeitschrift V.D.I.*, vol.

46, 1902.

[14] S.L. Smith, D. Dowson, and A.A.J. Goldsmith, "The lubrication of metal-on-metal total hip joints: A slide down the stribeck curve," *Proc. Instn. Mech. Engrs. J*, vol. 215, pp. 483-493, 2001.

[15] J. Peachey, J. Vanalsten, and S. Granick, "Design of an apparatus to measure the shear response of ultrathin liquid-films," *Rev. Sci. Instr.*, vol. 62, no. 2, pp. 463-473, 1991.

[16] R.J. Waltman, G.W. Tyndall, G.J. Wang, and H. Deng, "The effect of solvents on the perfluoropolyether lubricants used on rigid magnetic media," *Trib. Lett.*, vol. 16, no. 3, pp. 215-230, 2004.

[17] H. Kubotera and D.B. Bogy, "Numerical simulation of molecularly thin lubricant film flow due to the air bearing slider in hard disk drives," *Microsyst. Technol.*, vol. 13, pp. 859-865, 2007.

[18] R.P. Ambekar and D.B. Bogy, "Effect of slider lubricant pickup on stability at the head-disk interface," *IEEE Trans. Magn.*, vol. 41, no. 10, pp. 3028-3030, 2005.

[19] B. Marchon, Q. Dai, V. Nayak, and R. Pit, "The physics of the disk lubricant in the continuum picture," *IEEE Trans. Magn.*, vol. 41, no. 2, pp. 616-620, 2005.

[20] V. Raman, D. Jen, D. Gillis, and R. Wolter, "Component level investigations of liquid accumulation on slider - fly stiction," *IEEE Trans. Magn.*, vol. 5, pp. 2412-2414, 1999.

[21] B. Marchon, T. Karis, Q. Dai, and R. Pit, "A model for lubricant flow from disk to slider," *IEEE Trans. Magn.*, vol. 39, no. 5, pp. 2447-2449, 2003.

[22] V. Gupta and D.B. Bogy, "Dynamics of sub-5nm air bearing sliders in the presence of electrostatic and intermolecular forces at the head disk interface," *IEEE Trans. Magn.*, vol. 41, no. 2, pp. 610-615, 2005.

[23] R.J. Waltman, A. Khurshudov, and G.W. Tyndall, "Autophobic dewetting of perfluoropolyether films on amorphous-nitrogenated carbon surfaces," *Trib. Lett.*, vol. 12, no. 3, pp. 163-169, 2002.

[24] P.H. Kasai, "Perfluoropolyethers: Intramolecular disproportion," *Macromolecules*, vol. 25, pp. 6791-6799, 1992.

[25] P.H. Kasai and V. Raman, "Degradation of disk lubricant: Ramification in disk drives and direct detection by TOF-SIMS," *Trib. Lett.*, vol. 15, no. 1, pp. 15-28, 2003.

[26] M. Yang, F.E. Talke, D.J. Perettie, T.A. Morgan, and K.K. Kar, "Environmental effects on phosphazene lubricated computer hard disks," *IEEE Trans. Magn.*, vol. 30, no. 6, pp. 4143-4145, 1994.

[27] M. Yang et al., "Cyclotriphosphazenes as potential lubricants for thin film hard disks," *Trib. Trans.*, vol. 38, no. 3, pp. 636-644, 1995.

[28] C.M. Mate et al., "Investigation of phosphazene additive for magnetic recording lubrication," *IEEE Trans. Magn.*, vol. 34, no. 4, pp. 1744-1746, 1998.

[29] C.-Y. Chen, D.B. Bogy, T. Cheng, and C.S. Bhatia, "Effect of the additive X-1P on the tribological performance and migration behavior of PFPE lubricant at the head-disk interface," *IEEE Trans. Magn.*, vol. 36, no. 5, pp. 2708-2710, 2000.

[30] P.H. Kasai and A. Wakabayashi, "Disk lubricant additives, A20H and C2: Characteristics and chemistry in the disk environment," *Trib. Lett.*, vol. 31, pp. 25-35, 2008.

[31] P.H. Kasai, "Degradation of perfluoropolyehers and role of X1-P additives in disk files," *Proceedings MIPE Conference*, pp. 363-370, 1997.

[32] R.J. Waltman, N. Kobayashi, K. Shirai, A. Khurshudov, and H. Deng, "The tribological properties of a new cyclotriphosphazene-terminated perfluoropolyether lubricant," *Trib. Lett.*, vol. 16, pp. 151-162, 2004.

[33] H. Chiba, E. Yamakawa, T. Tokairin, Y. Oshikubo, and K. Watanabe, "Synthesis of multi-functional PFPE lubricant and its tribological characteristics," *Proc. 3rd World Tribol. Congr.*, pp. WTC2005-63165, 2005.

[34] B. Marchon et al., "Fomblin multidentate lubricants for ultra-low magnetic spacing," *IEEE Trans. Magn.*, vol. 42, no. 10, pp. 2504-2506, 2006.

[35] G.H. Vurens and D.L. Klein, "Composition and thickness distribution of carbon overcoat films on thin film magnetic disks studied with surface reflectance analyzers," *Proceedings of SPIE*, vol. 3619, pp. 27-34, 1999.

[36] D.L. Klein and G.H. Vurens, "Measurement of thin film disks by surface reflectance analysis," in *Proceedings of SPIE*, vol. 3619, 1999, pp. 18-26.

[37] G.H. Vurens, D.L. Klein, W. Gan, and T. Ultican, "Tribology applications of surface reflectance analyzers: optical characterization of the head disk interface," *Trib. Int.*, vol. 33, pp. 647-653, 2000.

[38] http://www.kla-tencor.com/current-products.html.

[39] http://www.kla-tencor.com/data-storage/candela-6300series.html.

[40] D.Y. Kwok, T. Gietzelt, K. Grundke, H.-J. Jacobasch, and A.W. Neumann, "Contact angle measurements and contact angle interpretation," *Langmuir*, vol. 13, pp. 2880-2894, 1997.

[41] "http://en.wikipedia.org/wiki/Goniometer".

[42] J.N. Israelachvili, *Intermolecular and surface forces, 2nd edition*. London: Academic Press, 1991.

[43] T. Young, "An essay on the cohesion of fluids," *Phil. Trans. R. Soc. Lond.*, vol. 95, pp. 65-87, 1805.

[44] A.W. Adamson, *Physical chemistry of surfaces*, 5th ed. New York: John Wiley & Sons, 1990.

[45] R.J. Waltman, "The interactions between Z-Tetraol perfluoropolyether lubricant and amorphous nitrogenated- and hydrogenated-carbon surfaces and silicon nitride," *J. Fluor. Chem.*, vol. 125, pp. 391-400, 2004.

[46] D.K. Owens and R.C. Wendt, "Estimation of the surface free energy of polymers," *J. Appl. Poly. Sci.*, vol. 13, pp. 1741-1747, 1969.

[47] G.F. Teletzke, H.T. Davis, and L.E. Scriven, "How Liquids Spread on Solids," vol. 55, no. 1-6, pp. 41-82, 1987.

[48] C.M. Mate, "Application of disjoining and capillary pressure to liquid lubricant films in magnetic recording," *J. Appl. Phys.*, vol. 72, no. 7, pp. 3084-3090, 1992.

[49] B.V. Derjaguin and M.M. Kusakov, "(In russian)," *Izv. Akad. Nauk. SSSR, Ser Khim*, vol. 5, p. 741.

[50] H.I. Kim, C.M. Mate, K.A. Hannibal, and S.S. Perry, "How disjoining pressure drives the dewetting of a polymer film on a silicon surface," *Phys. Rev. Lett.*, vol. 82, no. 17, pp. 3496-3499, 1999.

[51] D. Tabor and R.H.S. Winterton, "Surface forces: Direct measurement of normal and retarded van der Waals Forces," *Nature*, vol. 219, pp. 1120-1121, 1968.

[52] B.V. Derjaguin and N.V. Churaev, "Structural component of disjoining pressure," vol. 49, no. 2, pp. 249-255, 1974.

[53] J.N. Israelachvili, *Intermolecular and surface forces with applications to colloidal and biological systems*. London: Academic Press, 1985.

[54] F. Brochard-Wyart, J.-M. DiMeglio, D. Quere, and P.G. DeGennes, "Spreading of nonvolatile liquids in a continuum picture," *Langmuir*, vol. 7, pp. 335-338, 1991.

4 Spectroscopic Analysis and Surface Characterization of Magnetic Hard Disks

Structural and mechanical properties of the surface of a number of commercially available hard disks and sliders manufactured by various vendors were evaluated using AFM roughness measurement, nano-indentation and scratch testing, Raman spectroscopy and X-ray photoelectron spectroscopy.

4.1 AFM Roughness Measurements on Disk and Slider Surfaces

Atomic force microscopy (Veeco – Dimension 3000) in close contact mode (dynamic mode) was used to determine the roughness of a number of commercially available disks and sliders. The root-mean-square (Rms) roughness was determined on an area of $10x10\ \mu m^2$. A typical topography of the surface of a carbon coated disk is shown in Figure 4.1 as a 3-dimensional image.

The hard disks used in this experiment are from manufacturing years between 2004 and 2008. Figure 4.2 shows Rms roughness values for the disks, which decrease from 0.55 nm to 0.15 nm. Disk #1 has the highest Rms roughness and was manufactured in 2004, while disk #7 with the lowest Rms roughness was

manufactured in 2008. The disks have become so smooth over the years that the Rms

roughness is now on the order of the atomic distance between two carbon atoms.
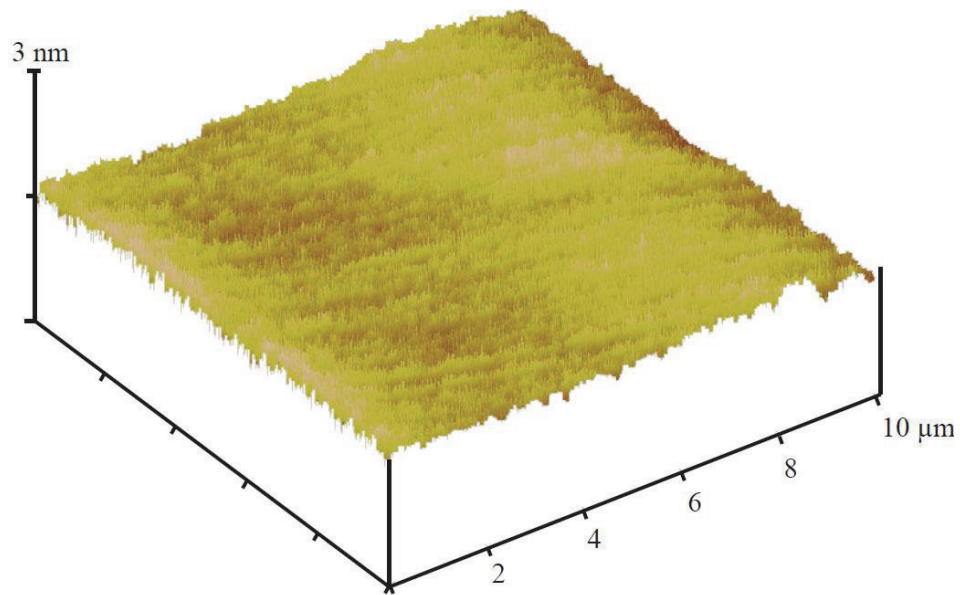
Figure 4.1: 3-D topography image of a smooth magnetic hard disk.

The Rms roughness for the sliders used in this study was between 0.3 nm and

0.5 nm (Figure 4.3). The surface roughness at the trailing edge of sliders has not been

improved as much over the last five years as the surface roughness of hard disks. In

today's disk drives the Rms roughness of the disks is much smaller than the Rms

roughness of the sliders.
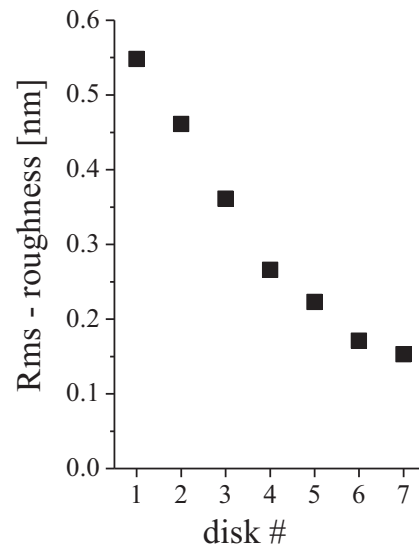
Figure 4.2: Comparison of RMS roughness of magnetic hard disk surfaces.
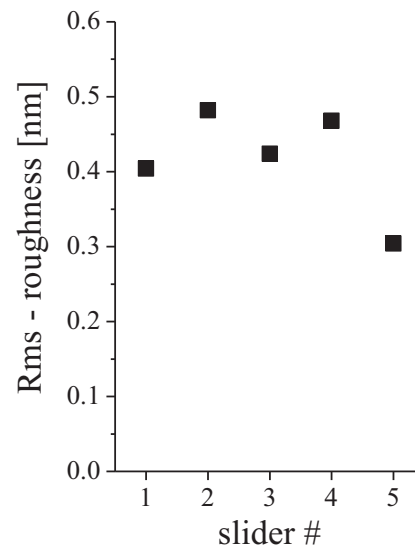
Figure 4.3: Comparison of RMS roughness commercially available slider surfaces.

4.2 Nano-indentation and Nano-scratch Testing of Sliders and Disks

The qualitative characterization of the mechanical properties of the surface of commercially available sliders and disks were investigated using a 2D - lateral force transducer (Triboscope®, Hysitron, Inc.) in conjunction with a scanning probe microscope stage (NanoScope®, Digital Instruments). Nano-indentation and nano-scratch testing was used to determine the relative hardness and the friction coefficient, respectively. For both sets of measurements, a cube corner diamond tip was used and the normal force applied to the surface was varied between 30 µN and 70 µN.

Figure 4.4 shows the hardness of the disks (a) and the sliders (b) measured using nano-indentation. The applied normal force was 70 µN, resulting in a penetration depth between 10 nm and 15 nm. Thus, the indentation depth is much larger than the thickness of the carbon film.
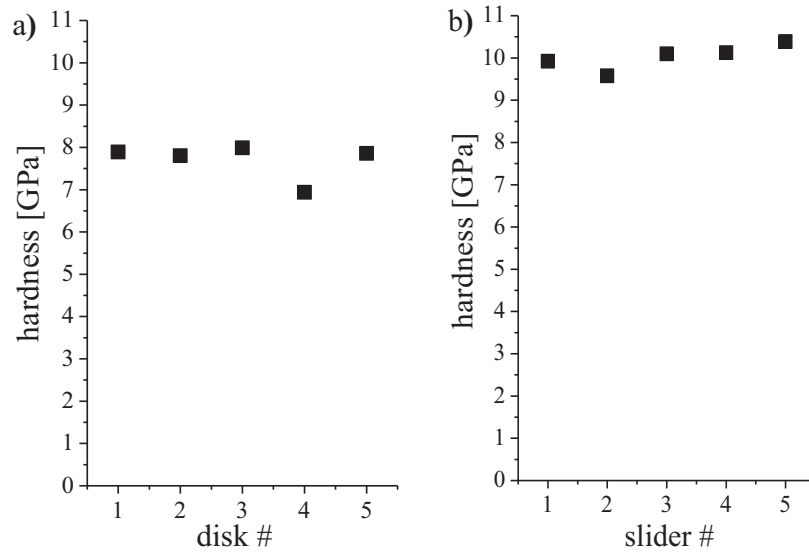
Figure 4.4: Hardness measurements on typical a) disk and b) slider surfaces using nano-indentation.

The results show hardness values between 7 GPa and 8.5 GPa for the disks and between 9.5 GPa and 10.5 GPa for the sliders. Figure 4.5 shows a 3-D scanning probe image of the nano-indentation on a hard disk with an indentation depth of approximately 10 nm.
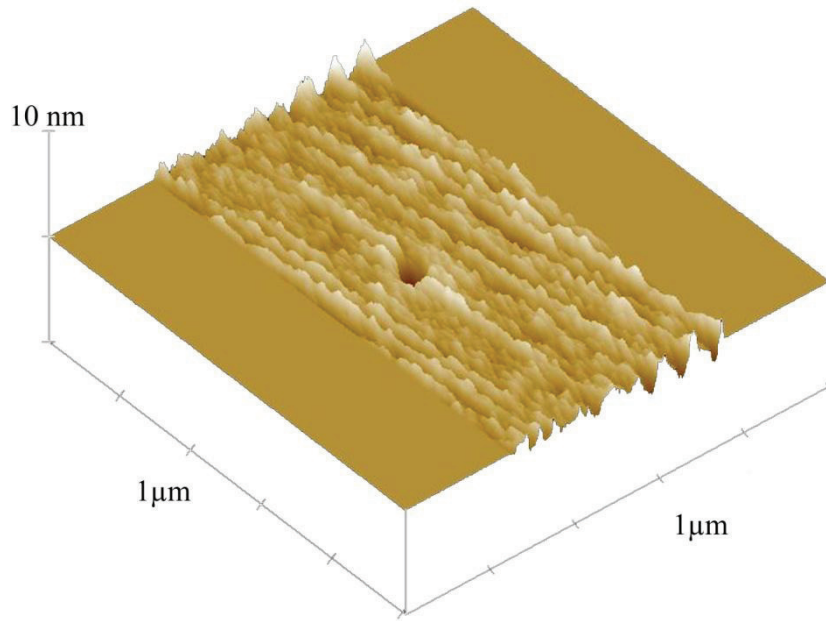
Figure 4.5: 3-D image of a nano-indentation on a hard disk.

Nano-scratch tests were also performed on conventional hard disks and sliders. The normal force, lateral force and resulting friction coefficients were measured. During the scratch testing the normal force applied to the cube corner diamond tip was increased from 0 µN to 70 µN. Figure 4.6 shows a scanning probe microscopy image of a typical nano-scratch test of about 4 µm in distance on a hard disk. A penetration into the surface occurs at loads above 35 µN, or 2 µm distance of the scratch.
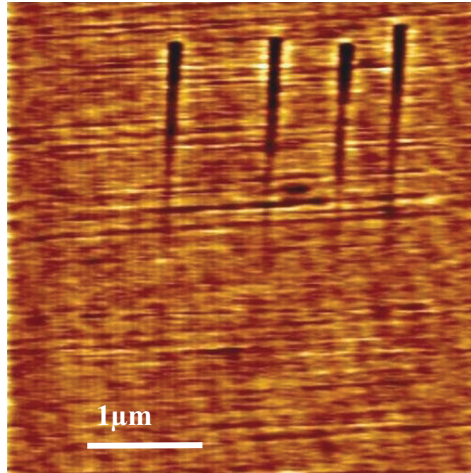
Figure 4.6: SPM image of nano-scratches on a hard disk.

Figure 4.7 shows the friction coefficients measured during nano-scratch testing of the carbon coated disks (a) and sliders (b). Analyzing the results of the tests, we observe that the friction coefficients are very similar for all disks and increase slightly with increasing load. For a load of 35 μN, a friction coefficient of approximately 0.17 was measured for the various disks, while at a load of 70 μN the friction coefficient increased to a value between 0.2 and 0.23. At a higher load, the indentation depth during scratching increases. Thus, it is likely that plastic deformation occurs which can result in plowing of the tip on the sample and therefore, the friction coefficient increases.

The friction coefficient for the various sliders varied between 0.25 and 0.4 and increased at higher loads of 70 μN. The value of the friction coefficient for slider #1 was higher compared to that of the other sliders and increased to 0.7 at the maximum

load of 70 µN. The increase in the friction coefficient appears to be related to plastic deformation during scratching. It is apparent, that the materials and tribological properties of the various disk and slider surfaces investigated are comparable and it seems that the films were manufactured in a similar way.
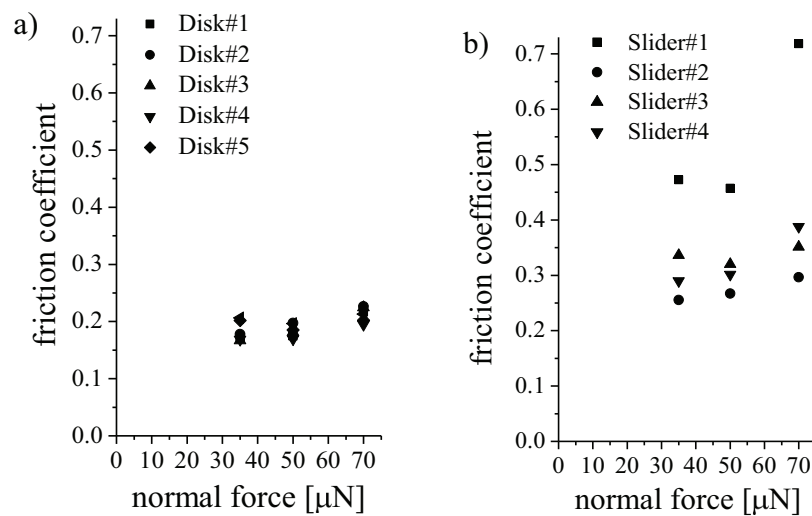
Figure 4.7: Friction coefficient measurements of carbon coated disks and slides at 35 µN, 50 µN and 70 µN using nano-scratch tests.

4.2.1 Nano-indentation in the Presence of Ultrasonic Excitation

Nano-indentation measurements in the presence of ultrasonic excitation have been performed on the carbon over-coated slider and hard disk. A driving frequency

between 101 kHz and 103 kHz was applied to the piezo at displacement amplitude of 1-2 nm. The indentation force maximum to the indenter tip was held constant at 35 μN for all measurements. Figure 4.8a) shows the force-displacement curve for an indentation measurement on a slider without ultrasonic excitation. The indentation depth is approximately 4.5 nm and the in-situ scanning probe microscopy (SPM) image in Figure 4.9a) does not show any physical evidence of an indentation.

Figure 4.8b) shows a force-distance curve of a nano-indentation performed in the presence of ultrasonic excitation. The indentation depth is significantly larger than for the static measurement at the same normal load. A clear indentation mark is visible in the scanning probe microscope (SPM) image (Figure 4.9b)). Discontinuities in the force displacement curve of Figure 4.8b) are observed during the loading cycle. It is hypothesized that these discontinuities are related to fatigue of the interface between the carbon film and the Al_3O_2-TiC substrate. During the cyclic loading, delamination from the substrate can occur and fatigue in the carbon overcoat can result in discontinuities in the force displacement curve [1]. Figure 4.9b) shows delamination or pile up to the left and right (bright half-oval area) of the indentation. The first discontinuity occurs at an indentation depth of approximately the thickness of the carbon overcoat at about 2 nm. We hypothesize that this is the indentation depth when the tip is breaking through the carbon layer. The second discontinuity at an indentation depth of about 4 nm is assumed to be the point where the carbon overcoat starts to delaminate.
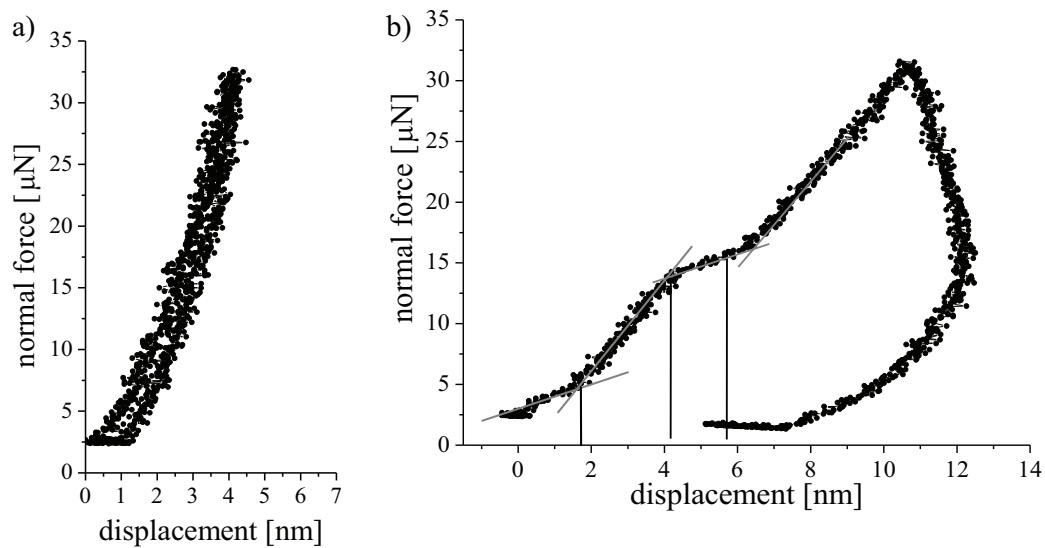
Figure 4.8: Nano-indentation (a) without ultrasonic excitation and (b) in the presence

of ultrasonic excitation, at 35 µN maximum force.
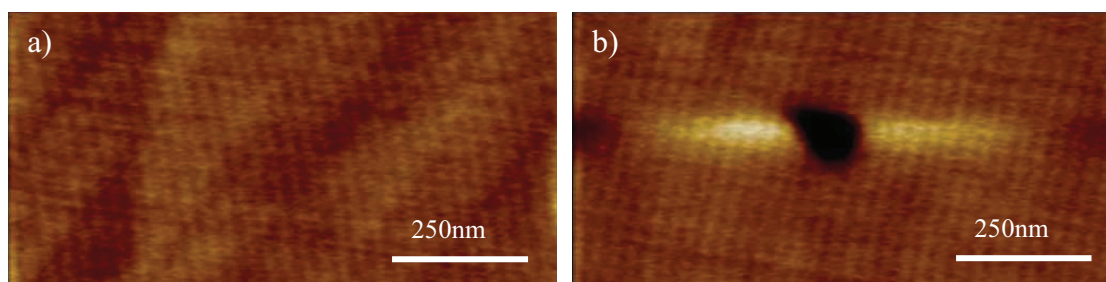
Figure 4.9: SPM images of nano-indentation at 35 µN. (a) without ultrasonic

excitation, (b) with ultrasonic excitation.

4.3 Raman Study on Hard Disks and Sliders

Raman spectroscopy is a spectroscopic technique used to study vibrational, rotational, and other low-frequency modes of atoms and molecules in material systems. The spectra can give information about bonding states in the carbon overcoat or oxidation states of metals. In this study, Raman spectroscopy was used to investigate the structural parameters of different carbon overcoats of commercially available hard disks and slider. A schematic of the Raman micro-spectrometer (Renishaw) as used in this study is shown in Figure 4.10. The Raman spectrometer uses a "Melles Griot" excitation laser. A monochromator eliminates the laser light side bands and the excitation wavelength of the system is 514.5 nm. The laser light is focused with the aid of an optical microscope on the specimen. The spatial resolution is 1 μm with a magnification of 100. The reflected light is send through a spectral grid to a charged coupled device (CCD) line for detection of the spectra. The spectral resolution is 1 cm^{-1} with a spectral range of 250 cm^{-1} to 4000 cm^{-1}.
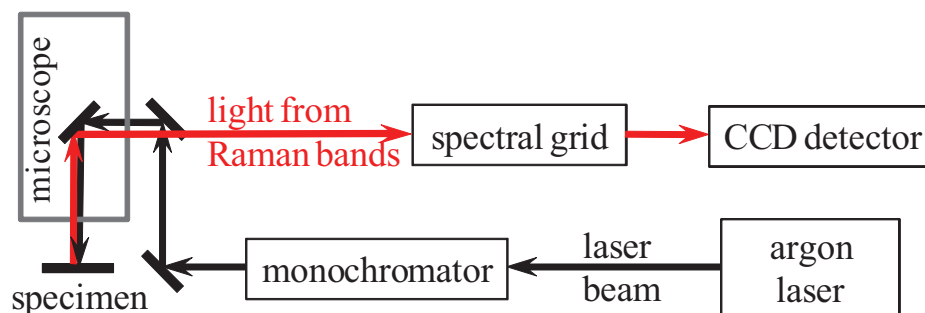
Figure 4.10: Schematic of the Raman spectrometer.

Figure 4.11 and Figure 4.12 shows Raman spectra for different commercially available disks and sliders from different vendors, respectively. The disk and sliders have a carbon overcoat thickness between 3 and 4 nm. From Figure 4.11 we observe that the Raman spectra for the disks evaluated are similar with defined G-band and D-band peaks at wavenumbers of 1560 cm^{-1} and 1389 cm^{-1}, respectively and an I(D)/I(G) ratio between 0.55 and 0.65. Therefore, a comparison with Figure 2.5 (from Chapter 2) suggests that the carbon is comprised of a high fraction of amorphous carbon (a-C) for the measured spectral profiles [2]. The variation in the overall spectral intensity of the curves for the disks is likely due to both laser beam misalignment and variation in the thickness of the carbon overcoats [3], [4]. In addition, the photoluminescence background [5] suggests that the nitrogen or hydrogen content is on the same order for all disks measured.

The Raman spectra of a number commercially available sliders are shown in Figure 4.12. We observe that the G-band is well defined for each spectrum and that the D-band peak is absent. This behavior is typical for a film with a tetrahedral amorphous structure with a high amount of sp^3-bonding. The sp^{-3}-bonding increases with an increase in wavenumber above 1520 cm^{-1}. This has been shown earlier in Figure 2.5 in Chapter 2 [6]. The position of the G-peak for the different sliders varies between 1522 cm^{-1} and 1560 cm^{-1}. An increase in sp^3-bonding due to for example an increase in hydrogen or nitrogen content in the carbon overcoat of the disks or the sliders can also add to the shift of the G-peak. This is also supported by the increased

slope of photoluminescence background if one compares the spectra of the sliders (Figure 4.12) with the spectra of the disks (Figure 4.11).

As a conclusion, the Raman spectra in Figure 4.11 and Figure 4.12 show differences in the amorphitization stage between the amorphous carbon films on the disks and the tetrahedral amorphous carbon films on the sliders. However, the difference between the individual disks is small and it is apparent that they are manufactured in a similar way. The same conclusion applies for the different sliders.
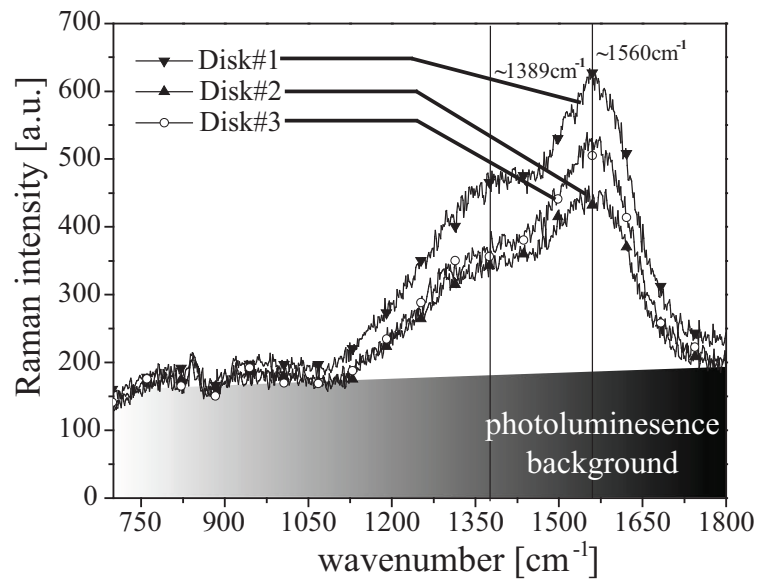
Figure 4.11: Raman spectra of different commercially available disks
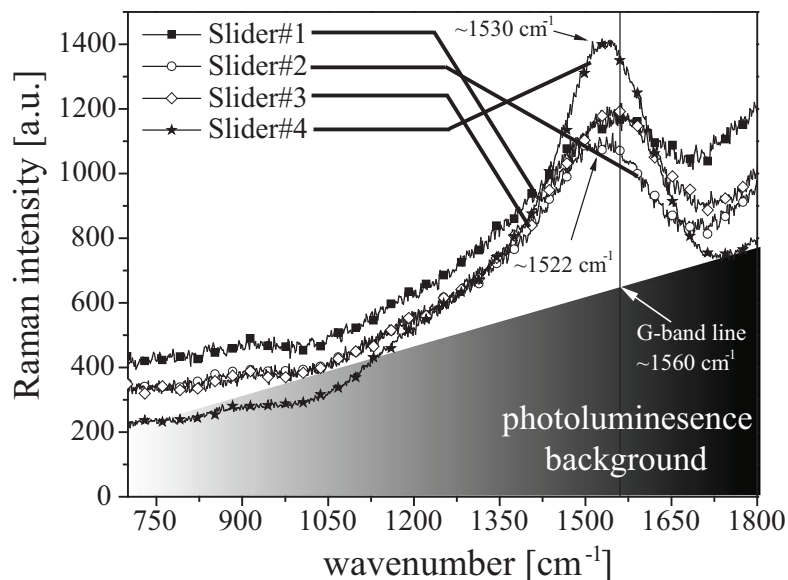
Figure 4.12: Raman spectra of different commercially available sliders

4.4 X-ray Photoelectron Spectroscopy on Hard Disks

X-ray photoelectron spectroscopy (XPS) is a quantitative spectroscopic technique to determine the composition, electronic state and chemical state of the elements in a material.   XPS spectra are obtained by measuring the kinetic energy and the number of electrons that escape from the sample surface after irradiating it with a beam of X-rays.   In this study X-ray photoelectron spectroscopy was used to determine material compositions on a typical hard disk. Figure 4.13 shows the XPS instrument that was used to study carbon coated and lubricated magnetic disks (Technical University of Ilmenau, Germany). X-rays were produced by $K\alpha$ electron transitions of magnesium with an energy of 1253.6eV. The X-rays were focused on the sample in the analytic ultra-high vacuum chamber. The electrons were captured in a half sphere analyzer to determine their kinetic energy as well as the binding energy.

Figure 4.14 shows an overview XPS spectrum of a carbon coated magnetic disk. The individual peaks and Auger transitions of the magnetic layer (Co 2p, Pt 4f, Cr 2p), the carbon overcoat (C 1s) and the lubricant (F 1s, C 1s, O 1s) are visible. From Figure 4.14 one can determine the materials in the sample and their composition. A more accurate scan with higher resolution can be performed for the peaks of interest to obtain further details, for example shifts in the spectrum due to defects or corrosion on the disk.
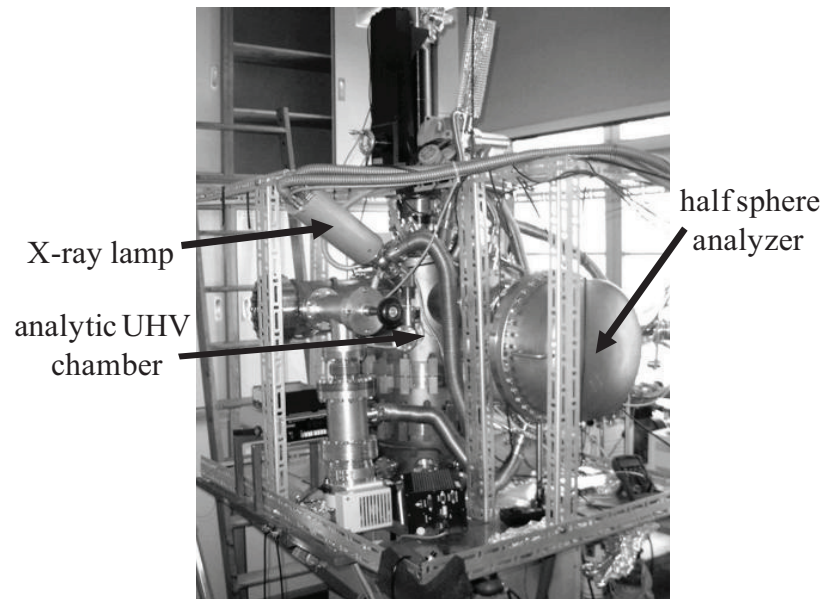
Figure 4.13: XPS instrument showing (Technical University of Ilmenau)

Figure 4.14 shows two XPS spectra, one of the initial disk surface and a second after 4 minutes of sputtering of the surface. The sputtering removed the

lubricant and carbon overcoat to expose the magnetic layer. As can be seen from the spectrum, the fluor peak (F 1s) disappeared, the carbon peak (C1s) is substantially reduced and the cobalt peak is enhanced. It can be seen from the spectrum overview after sputtering that the magnetic layer for this specific disk sample is an Co-Pt-Cr alloy.

Figure 4.15 shows the high resolution C1s spectrum of carbon on a smooth carbon coated magnetic disk. Using the high resolution spectra of the individual peaks one can determine peak shifts or changes of the intensity. This gives information about the bonding state of the atoms. In addition, due information about the carbon composition, film thickness, and even disk corrosion can be gathered.
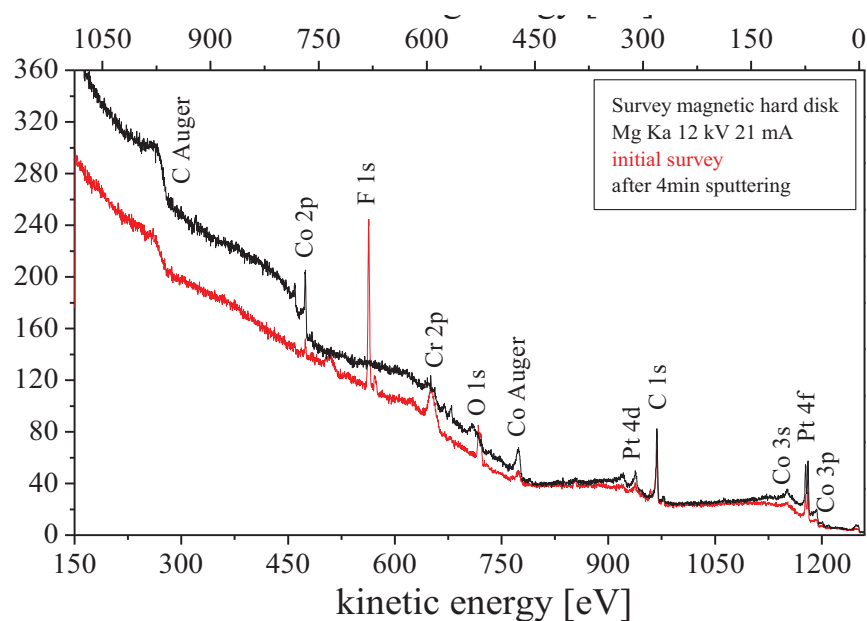
Figure 4.14: XPS survey spectrum of a carbon coated magnetic disk.
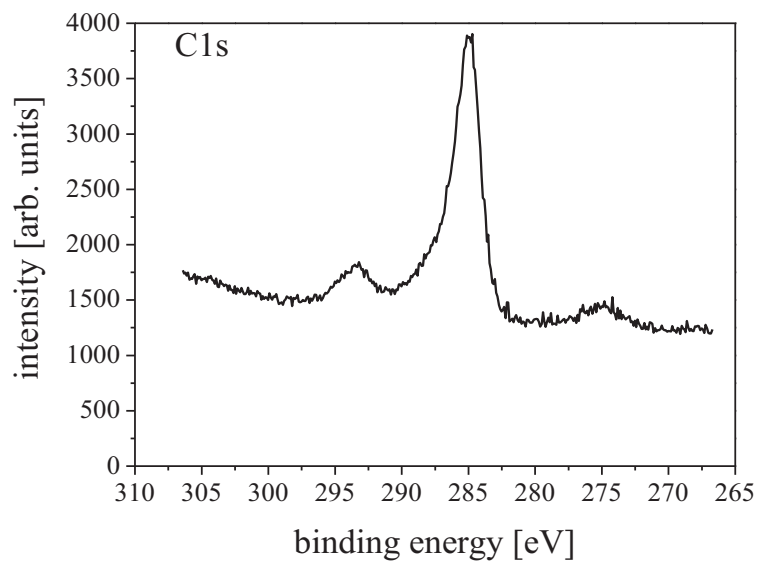
Figure 4.15: High-resolution scan of the C1s peak of carbon

The corrosion of a magnetic disk is associated with the coverage quality of the carbon overcoat and its thickness. For example, pinholes in the carbon overcoat, which increasingly appear at carbon thicknesses below 4 nm, allow oxygen to diffuse through the carbon and react with the metals in the magnetic layer (cobalt and chromium). Pinholes in the carbon overcoat can act as corrosion nuclei and damage the magnetic layer. XPS is very useful in the detection of oxidation of the underlying magnetic media. For example, cobalt (Co) 2p electrons can shift to higher binding energy when oxidized, which can be detected using XPS. As an example from the literature, Figure 4.16 shows cobalt (Co 2p) peaks [7] as a function of carbon coverage. A shift in their binding energy gives information about the corrosion state. For metallic cobalt, the Co $2p^{3/2}$ peak in the XPS spectrum was found at 778 eV

binding energy. An additional, broader peak at a higher binding energy of 782 eV appears when the carbon thickness decreases below 2.0 nm and cobalt starts to oxidize.
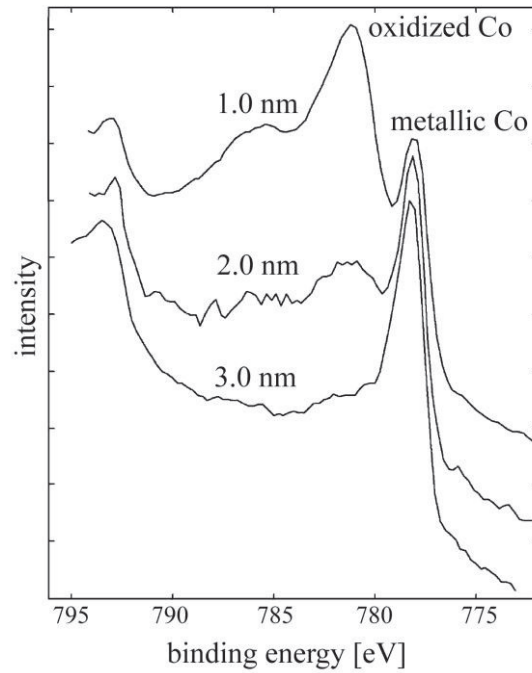
Figure 4.16: XPS spectra of the cobalt Co $2p^{3/2}$ peak for different carbon thicknesses [7]

X-ray photoelectron spectroscopy is a powerful tool to determine the properties of magnetic hard disks, from carbon coverage, lubricant thickness determination or materials combination of the magnetic layer.

Bibliography

[1] Y. Matsuda et al., "Nano-hardness testing with ultrasonic excitation," *Wear*, vol. 259, pp. 1497-1501, 2005.

[2] J. Robertson, "Diamond-like amorphous carbon," *Materials Science and Engineering*, vol. R 37, pp. 129-281, 2002.

[3] S.S. Varanasi, J.L. Lauer, F.E. Talke, G. Wang, and J.H. Judy, "Friction and wear studies of carbon overcoated thin films magnetic sliders: Application of Raman microspectroscopy," *Journal of Tribology*, vol. 119, p. 471, 1997.

[4] T.W. Scharf and I.L. Singer, "Thickness of diamond-like carbon coatings quantified with Raman spectroscopy," *Thin Solid Films*, vol. 440, pp. 138-144, 2003.

[5] M. Neuhaeuser, H. Hilgers, P. Joeris, R. White, and J. Windeln, "Raman spectroscopy measurements of DC-magnetron sputtered carbon nitride (a-C:N) thin films for magnetic hard disk coatings," *Diamond and Related Materials*, vol. 9, pp. 1500-1505, 2000.

[6] A.C. Ferrari, "Diamond-like carbon for magnetic storage disks," *Surf. and Coat. Tech.*, vol. 180, pp. 190-206, 2004.

[7] R. Ohr, B. Jacoby, M.v. Gradowski, C. Schug, and H. Hilgers, "Analytical and functional characterization of ultrathin carbon coatings for future magnetic storage devices," *Surf. Coat. Technol.*, vol. 174-175, pp. 1135-1139, 2003.

5 Spreading of a Small Droplet on a Smooth Solid Surface

In this chapter, the long time spreading of micro-droplets on a smooth solid surface is studied experimentally. An empirical expression is obtained for the spreading area as a function of time showing a final area when spreading stops. The mean film thickness of this final area appears to be independent of the initial volume of the droplet and of the spreading dynamics. A theoretical model is developed to predict this final uniform film thickness, based on volume conservation and the principle of minimum energy. Good agreement is found between the theoretical and experimental results.

5.1 Introduction

The spreading of liquid droplets on smooth solid surfaces has received much attention in the published literature over the last three decades [1], [2]. The dynamics of the spreading of macroscopic and microscopic-sized droplets on flat surfaces has been studied thoroughly, both experimentally [3], [4] and theoretically [5], [6]. A number of theoretical models have been developed to analyze the dynamics of spreading of a viscous micro droplet. The interface formation model by Decent [7], based on continuum mechanics and droplet volume conservation, is appropriate for systems with a film thickness of more than one monolayer. Molecular dynamics simulation and other numerical approaches were used by Cazabat et al. and de

134

Coninck et al. [**8**], [**9**], [**10**] for systems with film thicknesses on the order of one monolayer. The theory for thermodynamics of thin film wetting, which provides the physical insight for models of droplet spreading, can be found, for example, in Hough and White [**11**] from 1980. They computed the Hamaker constant for various materials and discussed the use of this constant in describing wetting phenomena.

Previous experimental studies focused on measuring the film thickness profile of the spreading droplet by using ellipsometry [**3**], [**10**]. De Coninck et al. [**10**], [**12**] used both numerical simulations and experimental measurements to study droplet spreading at time periods of up to 300 hours for which the radius of the droplet scales as the square root of time.

This chapter focuses primarily on the spreading of very small droplets of a perfluoropolyether having an initial volume on the order of pico-liters. These droplets, when spreading over a very long time, have a thickness on the order of less than one nanometer. This thickness value is typical for the lubricant thickness encountered on magnetic disks in a hard disk drive [**13**], [**14**].

We are interested in studying experimentally the spreading of a small droplet of fluid, on the order of pico-liters, on the surface of a smooth disk. In particular, we are interested in measuring the growth of the area wetted by the drop over a long time on the order of 2000 hours. For such long times the area wetted by the droplet can become large, resulting in a film thickness that is less than one molecular layer. In addition, we propose a model to predict this small film thickness using the principle of minimum energy.

5.2   Model for Lubricant Spreading

We consider the spreading of a liquid micro-droplet with an initial radius r_i and surface tension γ_{li} on a clean smooth surface of area A_s and surface energy $\gamma_s > \gamma_{li}$. We are interested in modeling the final thickness, h_f, after long spreading time in order to verify our experimental result that h_f is independent of the initial volume V_i. Prior to placing the droplet on the solid surface, the initial energy E_i of the system consists of the energy of the solid surface and the energy of the micro droplet, i.e.,

$$E_{si} = A_d \gamma_d + 4\pi r_i^2 \gamma_{li} \tag{5.1}$$

The principle of minimum energy will favor spreading of the droplet of lower surface energy γ_{li} over the solid surface with the higher surface energy γ_s in order to lower the energy level of the solid surface. During this process the surface energy of the spreading droplet increases. This process of energy exchange will continue as long as the energy level of the entire system is reduced. As the liquid micro-droplet spreads over the solid surface it covers a growing area A_l with surface energy $\gamma_l > \gamma_{li}$. Since we are interested in the spreading behavior after a long time, it is justifiable to assume that the wetted area A_l will have reached a uniform film thickness and hence, a state of uniform surface energy [15]. The energy level of the entire system at this stage of the spreading process is given by

$$E_s = (A_d - A_l)\gamma_d + A_l\gamma_l \qquad (5.2)$$

Figure 5.1 describes schematically the relevant areas of the system under consideration and their corresponding surface energies before and during spreading. Subtracting Eq. (5.2) from Eq. (5.1) gives the reduction in energy level of the system ΔE

$$\Delta E_s = E_{si} - E_s = A_l(\gamma_d - \gamma_l) + 4\pi r_i^2 \gamma_{li} \qquad (5.3)$$

where A_l is the wetted area, γ_s, γ_{li}, and γ_l are the surface energies of the bare solid surface, the bulk liquid and the wetted area, respectively. The associated energy increase of the droplet, ΔE_l, is

$$\Delta E_l = A_l\gamma_l - 4\pi r^2 \gamma_{li} \qquad (5.4)$$

The spreading process will continue as long as $\Delta E > \Delta E_l$. When $\Delta E = \Delta E_l$ the system reaches equilibrium and the spreading will end. At this stage the energy level of the entire system is at its minimum. The final wetted area is A_{lf} and its final surface energy is γ_{lf}.

droplet area: $4\pi r^2$ surface energy: γ_{li}	disk surface area: A_d surface energy: γ_d	wetted area: A_l surface energy: γ_l	disk surface area: $A_d - A_l$ surface energy: γ_d
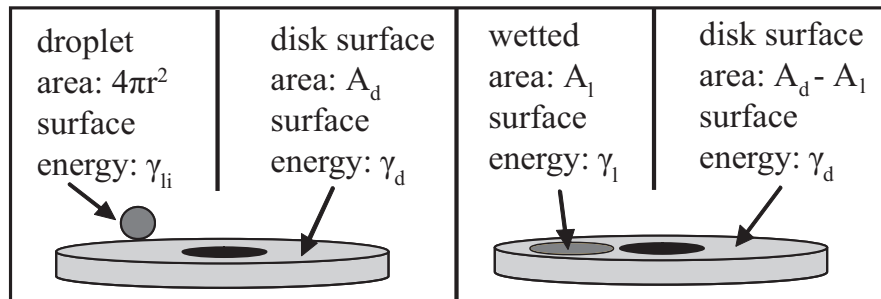
Figure 5.1: Schematic of the surface energy and area of the system

From Eqs. (5.3) and (5.4), the condition for termination of the spreading process is

$$A_{lf}(\gamma_d - \gamma_{lf}) + 4\pi r^2 = A_{lf}\gamma_{lf} - 4\pi r^2 \gamma_{li} \tag{5.5}$$

or

$$A_{lf}(2\gamma_{lf} - \gamma_d - 8\frac{\pi r^2}{A_{lf}}\gamma_{li}) = 0 \tag{5.6}$$

The final surface energy γ_{lf} of the wetted area is a function of the final film thickness h and can be approximated by (see e.g. [16])

$$\gamma_{lf} = \frac{C}{(h_f + d)^2} + \gamma_{li} \tag{5.7}$$

where C and d are constants that can be determined experimentally (see Appendix A and [17]). Noting that for $h_f = 0$ the surface energy γ_{lf} is that of the bare solid surface γ_s, Eq. (5.7) becomes

$$C = (\gamma_s - \gamma_{li})d^2 \tag{5.8}$$

Substituting C from Eq. (5.8) in Eq. (5.7) gives

$$\gamma_{lf} = \frac{d^2}{(h_f + d)^2}(\gamma_s - \gamma_{li}) + \gamma_{li} \tag{5.9}$$

Using Eq. (5.9) in Eq. (5.6) we derive the condition for termination of spreading as

$$2[\frac{d^2}{(h+d)^2}(\gamma_d - \gamma_{li}) + \gamma_{li}] - \gamma_d - 8\frac{\pi r^2}{A_{lf}}\gamma_{li} = 0 \tag{5.10}$$

For all practical matters the initial surface area of the droplet πr^2 is much smaller than the wetted area on the solid surface A_{lf}, i.e., $(\pi r^2 / A_{lf}) \ll 1$. Since γ_{li} is of the same order of magnitude as γ_s, the last term on the left hand side of Eq. (5.10) can be neglected resulting in

$$\frac{2d^2}{(h+d)^2}(\gamma_d - \gamma_{li}) = \gamma_d - 2\gamma_{li} \tag{5.11}$$

or

$$(h+d)^2 = 2d^2 \frac{\gamma_d - \gamma_{li}}{\gamma_d - 2\gamma_{li}} \tag{5.12}$$

We note that a solution of Eq. (5.12) exists only if $\gamma_d > 2\gamma_{li}$. Hence, a condition for

the spreading process to reach the stage of uniform film thickness is that the surface

energy of the smooth surface is at least twice that of the bulk of the liquid. This does

not mean that spreading will not take place if $\gamma_{li} < \gamma_s < 2\gamma_{li}$, but only that spreading

may stop before the uniform thickness state is reached. When $\gamma_s \gg 2\gamma_{li}$, spreading is

very favorable from an energy point of view and from Eq. (5.12) the film thickness of

the spread lubricant at the equilibrium stage becomes

$$h = (\sqrt{2} - 1)d \tag{5.13}$$

Equation (5.13) is the lower limit for h_f. For any other case for which $\gamma_s > 2\gamma_{li}$

$$h = [(2\frac{\gamma_d - \gamma_{li}}{\gamma_d - 2\gamma_{li}})^{1/2} - 1]d \tag{5.14}$$

In our experiments $\gamma_s = 52.3\,mJ/m^2$ and $\gamma_{li} = 17mJ/m^2$. Thus, the condition

$\gamma_s > 2\gamma_{li}$ was met. As can be seen from Eq. (5.14) the predicted final film thickness of

the spread droplet is independent of the initial droplet volume. The final film

thickness depends only on the surface energies of the solid surface γ_s, the initial

liquid droplet γ_{li}, and the constant d (see Appendix A). We also note that the final

film thickness is independent of the spreading rate coefficient C_2. Hence, our model

appears to be valid for any type of liquids regardless of the factors affecting its spreading dynamics.

5.3 Experimental Verification

5.3.1 Materials

A perfluoropolyether-type lubricant, Fomblin Z-Dol[TM], was used in this investigation. Z-Dol is a random copolymer of perfluoromethylene oxide and perfluoroethylene oxide repeat units with hydroxyl moieties on both ends

$$HO\text{-}CH_2\text{-} CF_2 \text{-}O\text{-}(CF_2 \ CF_2O)_p\text{-}(CF_2O)_q\text{-} CF_2\text{-}CH_2\text{-}OH \ .$$
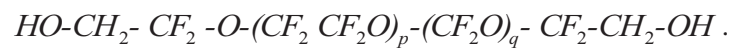
The molecular weight of Z-Dol in this experiment was 2000 amu and a polydisperisty of 1.07. The droplet was taken from a solution containing 0.006% Z-Dol in a solvent known as Vertrel XF[TM] $(CF_3\text{-}CFH\text{-}CHF\text{-}CF_2\text{-}CF_3)$. A motorized syringe from a contact angle instrument (AST VCA 2500XE) was used to place a droplet with an accurately measured volume on a smooth solid surface. This surface was coated by a top layer of nitrogenated carbon (CN_x) typically used in hard disk drives. The dispersive component γ_s^d and the polar component γ_s^p of the total surface energy γ_s of the CN_x surface were measured before the spreading experiments by contact angle goniometry using diiodomethane and DI water, respectively, as described in [13]. The total surface energy, which is the sum of dispersive and polar components, was 52.3 mJ/m^2. The RMS roughness of the CN_x surface was measured using an AFM. The roughness average (Ra) value was found to be 0.28 ± 0.03 nm. The dispersive and

polar components of the surface energy of Z-Dol are given in Refs. [13] and [18]. The sum of both components is 17 mJ/m^2. A summary of the various surface energy values is presented in Table 5.1.

Table 5.1: Surface energies of the materials used

Materials	γ^d [mJ/m^2]	γ^p [mJ/m^2]	γ^{total} [mJ/m^2]
Fomblin Z-Dol [13], [18]	15.5	1.5	17
CN$_x$ surface	38.7	13.6	52.3

5.3.2 Lubricant Spreading Experiment

Droplets of the lubricant-solvent solution (0.006% Fomblin Z-Dol lubricant in Vertrel XF solvent) with a total volume ranging between 0.1 μl and 1 μl where placed on the disk surface. The solvent of the lubricant/solvent solution (with 0.006% Z-Dol) evaporates, leaving behind pure Z-Dol micro droplets (with droplet radii on the order of 10 μm) to spread over the solid surface. The volume of the Z-Dol droplets after solvent evaporation was approximately 6, 18, 30, and 60 pl, respectively.

The area growth of the spreading droplets was measured as a function of time using a scanning reflectance analyzer (SRA). Measurements were taken at intervals of 24 hours over a period of approximately 11 weeks. The experiment was performed in a laboratory environment of approximately 25˚C and 60% relative humidity. Figure 5.2 shows an SRA image of the spreading droplets on the surface.

Figure 5.2: SRA image of four spreading droplets on a smooth CNx disk surface.

5.3.3 Results and Discussion

Figure 5.3 shows the spreading area as a function of time for the various droplet volumes used in this experiment. The spreading area follows an exponential decay curve saturating at a final value A_{lf}. The experimental results can be approximated by

$$A_l = A_0 + C_1(1 - e^{-C_2 t}) \qquad (5.15)$$

where A_0 is the droplet area at time $t = 0$ and C_1, C_2 are constants. In the limit $t \to \infty$, Eq. (5.15) yields $A_{lf} = A_0 + C_1$. Hence, C_1 is the droplet area growth after a very long time. The constant C_2 in Eq. (1) is a spreading rate coefficient, which may depend on structural and chemical properties such as polarity and molecular weight of the spreading liquid, interaction with the solid surface, and the presence of solvents or additives [18], [19], [20]. Interestingly, according to Eq. (1a) the final area of the droplet is independent of the spreading rate coefficient C_2. Table 5.2 presents the

values of the initial area A_0 and the constants C_1 and C_2 for the various initial

volumes V_i of the droplets used in this study.
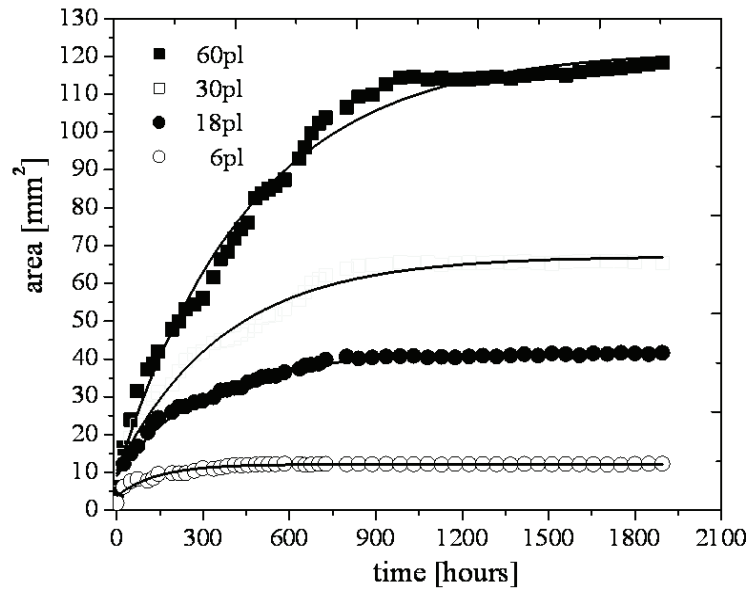
Figure 5.3: Area as a function of time.

At the initial stages of spreading, when time t is very small, the exponent in

Eq. (5.15)can be approximated by:

$$e^{-C_2 t} = 1 - C_2 t \qquad (5.16)$$

Thus, Eq. (5.15) becomes:

$$A_l = A_0 + C_1 C_2 t \qquad (5.17)$$

Equation (5.17) is in agreement with observations from previous experimental studies

[10], [12], [21] as well as molecular dynamic simulation [6], [22], where the radius of

the spreading area grows as $\sqrt{t}$ for short spreading times. Therefore, it seems that Eq. (5.17) and the previously reported observations represent a limiting case of the more general behavior provided by Eq. (5.15). A spreading rate behavior similar to that described by Eq. (5.15) was also observed in Ref. [8]. In these studies the diameter of the spreading area increased as a function of $\sqrt{t}$ for the first 400 hours and then started to decrease for the rest of the test that lasted up to about 2000 hours.

In our experiments we limited the spreading time to $t = t_f$, i.e., the time when the spreading rate has decreased to 1% of its value at $t = 0$. The spreading rate at time t is obtained by differentiation of Eq. (5.15) with respect to time, i.e.

$$\left(\frac{dA_l}{dt}\right)_{t=t_f} = C_1 C_2 e^{-C_2 t_f} = 0.01 C_1 C_2 \tag{5.18}$$

Hence, from the above requirement for the spreading rate at $t = t_f$, we have $C_1 C_2 e^{-C_2 t_f} = 0.01 C_1 C_2$, and the time t_f is

$$t_f = \frac{\ln 100}{C_2} \tag{5.19}$$

We have calculated the final time t_f and the corresponding final area A_{lf} of the spreading droplet using Eqs. (5.19) and (5.15), respectively. In addition, assuming volume conservation, the final average thickness of the droplet after spreading can be determined from

$$h_f = \frac{V_i}{A_{lf}} \tag{5.20}$$

The values of t_f, A_{lf} and h_f, are also listed in Table 5.2 for the different initial droplet volumes. Although the initial volume V_i varied by an order of magnitude, the final film thickness h_f varies only from 0.44 nm to 0.49 nm. Hence, it is justifiable to assume that h_f is independent of V_i. We also note that the final film thickness is less than the thickness of one monolayer of Zdol, which is about 1.5 nm [**23**].

Table 5.2: Summary of the parameters of Eq. (5.15) and the calculated final parameters of the spreading experiments.

	V_i [pl]	A_0 [mm^2]	C_1 [mm^2]	C_2 [h^{-1}]	t_f [h]	A_{lf} [mm^2]	thickness h_f [nm]
	60	9.5	112.2	0.0022	2132.02	121.70	0.49
CN$_x$	30	10.5	56.70	0.0027	1705.62	67.20	0.45
surface	18	9.1	32.20	0.0035	1315.76	41.30	0.44
	6	3.8	8.40	0.0070	657.88	12.20	0.49

Using Eq. (5.14) and the value of the constant d, which for Z-Dol 2000 was found to be 0.55 nm (see Appendix A), one can calculate the theoretical final film thickness to be h_f = 0.53 nm. This value is in good agreement with the mean value of 0.47 nm obtained from the spreading experiment (see Table 5.2). The final film thickness of Z-Dol is molecularly thin and less than one monolayer [**23**]. This small film thickness also justifies the use of Eq. (5.7) for the polar Zdol 2000 liquid.

It should be noted here that the experimental final film thickness was obtained from Eq. (5.20) by dividing the measured initial droplet volume by the measured final

spreading area, assuming volume conservation. It is possible, however, that continuum mechanics breaks down when the thickness of the spreading droplet is on the order of one monolayer. In this case volume conservation is questionable [6] and the density of the spreading droplet can become smaller than that of the bulk liquid. As a result the measured final area would be larger than the expected area for constant density. These factors may contribute to the lower film thickness obtained experimentally compared to that predicted by the model.

Current optical methods for measuring the thickness of thin liquid layers [24], [25] also assume that the density is constant (same as that of the bulk). Again, this assumption may be erroneous in the case of molecularly-thin films. Although outside the scope of the current work, it seems important to examine the assumption of constant density in future work.

5.3.4 Model Verification with a Dispersive Liquid

In order to verify the use of Eq. (5.14) of our model, i.e., that h_f is independent of the parameters affecting the spreading rate of a liquid, an additional experiment was performed with a dispersive liquid, pure Fomblin Z (15-cut fractionation) having a molecular weight of 2290 amu. Pure Z2290 consists of a random copolymer of perfluoromethylene oxide and perfluoroethylene oxide repeat units. Its dispersive surface energy is 16.2 mJ/m^2, as reported by the supplier. The pure liquid itself, without any solvents such as used previously with Zdol 2000, was

deposited onto the smooth surface with a micro pipette. The inner diameter of the pipette tip was on the order of 75 μm as shown in Figure 5.4.

150 μm
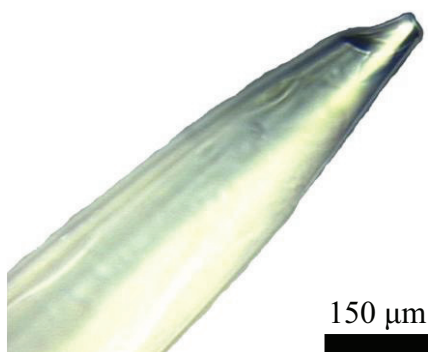
Figure 5.4: Micro-pipette tip

The tip was brought slowly into contact with the smooth surface and was then retracted immediately. A small amount of pure Z2290 with an initial volume of approximately 60 pico liter was transferred to the surface. This is the minimum volume that could be deposited by using the micro-pipette without resorting to the use of a solvent. The area growth of the spreading droplet was then measured as a function of time (see Figure 5.5) using the same method as used for Zdol 2000. Area measurements were taken every hour during the early stage of spreading and at increasing time intervals up to 36 hours as the spreading time increased and the area growth rate decreased.
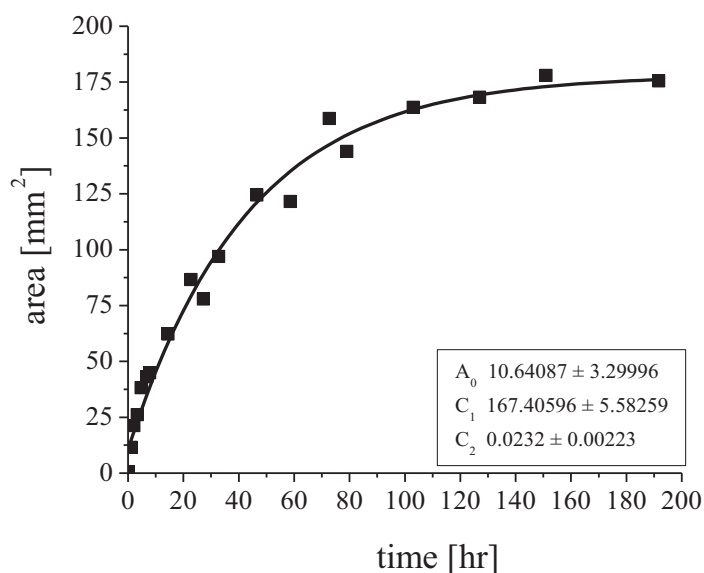
Figure 5.5: Area as a function of time for Z2290 dispersive liquid.

The spreading of Z2290 was much faster compared to Zdol 2000. This can be explained by the lack of polar end groups in Z2290 compared to Zdol 2000, i.e., polar end groups cause larger interaction with the carbon surface [23].

Figure 5.6 presents the profiles of the spreading Z2290 droplet measured by the HDI SRA across the center of the spreading area after 3 and 20 hours of spreading time and after approximately 200 hours. It is observed from Fig. 6 that the droplet thickness decreases and becomes more uniform as the area grows with increasing spreading time.
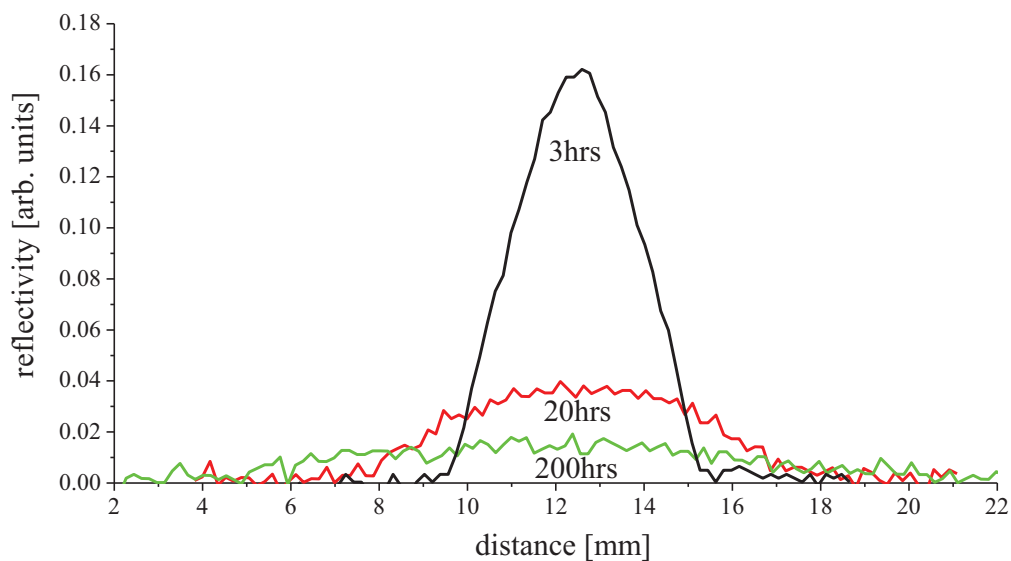
Figure 5.6: Droplet profiles of the Z2290 at various spreading stages, at the beginning

of spreading (3hrs), after 20 hours and after 200 hours.

Table 5.3 shows a summary of the parameters of Eq. (5.15) and the calculated

final parameters of the spreading experiment for Z2290. Comparing these parameters

for the 60 pico liter droplet of Z2290 with the values from Table 5.2 for Zdol 2000, we

find that the spreading coefficient C_2 is an order of magnitude higher for the dispersive

Z2290. We also note that the final time t_f for Z2290 to reach the spreading

equilibrium is an order of magnitude lower than for Zdol 2000. However, the final

area and final film thickness are on the same order of magnitude. This suggests that

our model is applicable for both purely dispersive and dispersive/polar liquids, as well

as for liquids deposited on the surface with or without a solvent.

Using Eq. (5.14) for Z2290 with $\gamma_{li} = 16.2\,\mathrm{mJ/m^2}$ and assuming values of the constant d between 0.25 nm and 0.69 nm as reported in [**26**], [**27**], we obtain that the theoretical final film thickness for Z2290 is between 0.23 nm and 0.62 nm. The experimentally obtained value of 0.34 nm for the final film thickness, h_f, of Z2290 (see Table 5.3) is within this range.

Table 5.3: Summary of the parameters of Eq. (5.15) and the calculated final parameters of the spreading experiment with Z2290 on CNx surface.

V_i [pl]	A_0 [mm^2]	C_1 [mm^2]	C_2 [hr^{-1}]	t_f [hr]	A_{lf} [mm^2]	thickness h_f [nm]
60	10.64	167.41	0.0232	198.50	176.37	0.34

5.4   Conclusion

The long time spreading of micron-size droplets on a smooth solid surface was studied experimentally. The spreading area was measured over a period of up to 2000 hours. A decreasing growth rate was observed and the spreading was found to terminate after long time. The best fit of the experimental results provided an empirical expression for the spreading area as a function of time. It was shown that the linear relation between spreading area and time, reported in the literature for short spreading times, is only a limiting case of the more general expression presented in

this work. The final area of the droplet was found to be independent of the spreading rate coefficient.

The average final film thicknesses of the measured final wetted areas were calculated from the known initial droplet volumes assuming volume conservation, and were found to be independent of the initial volume.

A theoretical model for the final film thickness was developed based on the principle of minimum energy. It was found that long time spreading, which yields uniform film thickness, requires that the surface energy of the solid is at least twice that of the liquid bulk material. The theoretically predicted final film thickness was found to be independent of the initial droplet volume and independent of the spreading dynamics in agreement with the experiments. The value of this theoretical final film thickness was in good agreement with the experimental results.

5.5 Acknowledgement

Bibliography

[1] P.G. de Gennes, "Wetting: Statics and dynamics," *Rev. Mod. Phys.*, vol. 57, pp. 827-863, 1985.

[2] M. Chung, Y.-C. Wu, and F.E. Talke, "Film thickness dependence of lubricant mobility," *Trib. Lett.*, vol. 32, no. 35, pp. 35-41, 2008.

[3] F. Heslot, A.M. Cazabat, P. Levinson, and N. Fraysse, "Experiments on wetting on the scale of nanometers: Influence of the surface energy," *Phys. Rev. Lett.*, vol. 65, pp. 599-602, 1990.

[4] F. Heslot, A.M. Cazabat, N. Fraysse, and P. Levinson, "Experiments on spreading droplets and thin films," *Adv. Coll. Interf. Sci.*, vol. 39, pp. 129-145, 1992.

[5] X. Li, Y. Hu, and H. Wang, "Modeling of lubricant spreading on a solid substrate," *J. Appl. Phys.*, vol. 99, p. 024905, 2006.

[6] J. de Conick, "Spreading of chain-like liquid droplets on solids," *Coll. and Surf. A*, vol. 114, pp. 155-160, 1996.

[7] S.P. Decent, "The spreading of a viscous microdrop on a solid surface," *Microfl. Nanofl.*, vol. 2, pp. 537-549, 2006.

[8] A.M. Cazabat, J. de Connick, S. Hoorelbeke, M.P. Valigant, and S. Villette, "Influence of substrate heterogeneities on the spread of a drop," *Phys. Rev. E*, vol. 49, pp. 4149-4153, 1994.

[9] A.M. Cazabat, M.P. Valignat, S. Villette, J. de Connick, and F. Louche, "The mechanism of spreading - A microscopic description," *Langmuir*, vol. 13, pp. 4754-4757, 1997.

[10] J. de Coninck, S. Hoorelbeke, M.P. Valignat, and A.M. Cazabat, "Effective microscopic model for the dynamics of spreading," *Phys. Rev. E*, vol. 48, pp. 4549-4555, 1993.

[11] D.B. Hough and L.R. White, "The calculation of hamaker constants from liftshitz theory with applications to wetting phenomena," *Adv. Colloid Interface Sci.*, vol. 14, no. 1, pp. 3-41, 1980.

[12] J. de Coninck, N. Fraysse, M.P. Valignat, and A.M. Cazabat, "A microscopic simulation of the spreading of layered droplets," *Langmuir*, vol. 9, pp. 1906-1909, 1993.

[13] G.W. Tyndall, T.E. Karis, and M.S. Jhon, "Spreading profiles of molecularly thin perfluoropolyether films," *Trib. Trans.*, vol. 42, pp. 463-470, 1999.

[14] S.K. Deoras, S.-W. Chun, G. Vurens, and F.E. Talke, "Spreading and mobility analysis of PFPE lubricants using a surface reflectance analyzer (SRA)," *Trib. Int.*, vol. 36, pp. 241-246, 2003.

[15] F. Brochard-Wyart, J.M. di Megilo, and P.G. de Gennes, "Spreading of nonvolatile liquids in a continuum picture," *Langmuir*, vol. 7, pp. 335-338, 1991.

[16] R.J. Waltman, "The interactions between Z-Tetraol perfuoropolyether lubricant and amorphous nitrogenated- and hydrogenated-carbon surfaces and silicon nitride," *J. Flu. Chem.*, vol. 125, pp. 391-400, 2004.

[17] R. Brunner, I. Etsion, and F.E. Talke, "A simple atomic force microscopy calibration method for direct measurement of surface energy on nanostructured surfaces covered with molecularly thin liquid films ," *Rev. Sci. Instrum.*, vol. 80, no. 5, p. 055109, 2009.

[18] R.J. Waltman, A. Khurshudov, and G.W. Tyndall, "Autophobic dewetting of perfluoropolyether films on amorphous-nitrogenated carbon surfaces," *Trib. Lett.*, vol. 12, no. 3, pp. 163-169, 2002.

[19] R.J. Waltman, G.W. Tyndall, G.J. Wang, and H. Deng, "The effect of solvents on the perfluoropolyether lubricants used on rigid magnetic media," *Trib. Lett.*, vol. 16, no. 3, pp. 215-230, 2004.

[20] T. Cheng, B. Zhao, J. Chaoa, S.W. Meeks, and V. Velidandeaet, "The lubricant migration rate on the hard disk surface," *Trib. Lett.*, vol. 9, no. 3-4, pp. 181-185, 2000.

[21] M. Voue, M.P. Valignat, G. Oshanin, A.M. Cazabat, and J. de Coninck, "Dynamics of spreading of liquid microdroplets on substrates of increasing surface energies," *Langmuir*, vol. 14, pp. 5951-5958, 1998.

[22] M. Voue and J. de Coninck, "Spreading and wetting at the microscopic scale," *Acta Mater.*, vol. 48, pp. 4405-4417, 2000.

[23] R.J. Waltman et al., "The effect of carbon overcoat thickness on the Zdol boundary lubricant film," *Trib. Lett.*, vol. 12, no. 1, pp. 51-60, 2002.

[24] M.F. Toney, M.C. Mate, A.K. Leach, and D. Pocker, "Thickness measurements of thin perfluoropolyether polymer films on silicon and amorphous-hydrogenated carbon with X-ray reflectivity, ESCA and optical ellipsometry," *J. Coll. Int. Sci.*, vol. 225, pp. 219-226, 2000.

[25] X. Ma, H. Tang, and J. Gui, "Temperature effect on spreading of perfluoropolyethers on amorphous carbon films," *Trib. Lett.*, vol. 10, pp. 203-209, 2001.

[26] R.J. Waltman, B.K. Yen, and R.L. White, "The adhesion of monomolecular hydroxyl-terminated perfluoropolyether liquid films on the sputtered silicon nitride surface as a function of end group acidity and mobility," *Trib. Lett.*, vol. 20, no. 1, pp. 69-81, 2005.

[27] R.J. Waltman, G.W. Tyndall, and J. Pacansky, "Computer-modeling study of the interactions of Zdol with amorphous carbon surfaces," *Langmuir*, vol. 15, pp. 6470-6483, 1999.

6 Surface Energy, Adhesion and Friction between Surfaces Separated by Molecularly-thin Perfluoropolyether Films

The relationship between the adhesion of surfaces separated by a molecularly-thin liquid film and the surface energy of the film was investigated. AFM-based force distance curves were measured on a series of carbon surfaces coated with hydroxyl-terminated perfluoropolyether (PFPE) films. The surface energy of the PFPE films was varied by altering either the total film thickness or the bonding ratio of the film by changing the concentration of the PFPE film in the solution and/or the pull-rate during dip-coating. A linear relationship between adhesion force and surface energy was observed. Furthermore, adhesion was found to vanish at non-zero values of surface energy. The experimental results indicate that the adhesive force between macroscopic bodies separated by molecularly-thin liquid films is linearly proportional to the excess surface energy of the film.

6.1 Introduction

The adhesion between two solid surfaces in the presence of a molecularly-thin liquid film is of both academic interest and of extreme importance to numerous technological applications [1], [2]. The relationship between adhesion and surface energy between two macroscopic bodies has been studied in detail for the case of bulk

155

materials. In the classical view of adhesion theory, the force required to separate two surfaces is linearly proportional to the work required to form two interfaces [3].

When a molecularly-thin liquid film is applied to a solid surface, the surface energy of the film can vary significantly due to interaction of the liquid with the underlying surface [4], [5], [6]. For example, the dispersive interactions between a surface and a completely wetting liquid film will result in a free energy that rapidly increases as the film thickness is decreased [7]. The thickness dependence of the dispersive surface energy $\gamma^d(h)$ can be expressed in terms of the free energy of the bulk material γ^d_{bulk} as

$$\gamma^d(h) = \gamma^d_{bulk} + \Delta\gamma^d(h) \qquad (6.1)$$

where $\Delta\gamma^d(h)$ is termed the excess surface energy, which scales inversely as the square of the film thickness [3], [7].

In addition to the van der Waals interactions, molecular-specific interactions, such as hydrogen-bonding, dipole-dipole interactions, or covalent bonding can develop between the applied liquid film and the solid substrate. The presence of these adhesive interactions, which are absent in the bulk liquid, will be manifested as a change in the polar surface energy of a molecularly-thin film. In the case of hydroxyl-terminated perfluoropolyether (PFPE) films, the adhesive interaction strength, and hence the polar surface energy, is sensitive to the relative level of bonding between the polar end-groups of the PFPE lubricant and the polar sites on the carbon surface. The number of lubricant end-groups that are bonded to the carbon surface can be increased

by exposure to elevated temperature. As the bonding ratio is increased, the polar surface energy component decreases. It is therefore possible in these systems to vary both the dispersive and polar surface energy components by altering the film thickness and/or bonding ratio. Thus, these films allow a quantitative investigation of the relationship between adhesion and the total surface energy. Furthermore, the ability to independently manipulate surface energy components, as well as the magnitude of the excess surface energy, could yield additional information. Specifically, this allows us to determine how the adhesion scales with the total surface energy γ^{T}, the individual surface energy components γ^{d} and γ^{p}, and the excess surface energy components $\Delta\gamma^{\mathrm{d}}$, $\Delta\gamma^{\mathrm{p}}$.

6.2 Theoretical Background

6.2.1 Friction and Surface Energy

The study of friction between two surfaces is a subject of intense research, however, a solution for friction force between two macroscopic bodies must be found empirically. As described in Chapter 3, the types of lubrication and the resulting friction coefficient can be divided into three basic types: i) hydrodynamic lubrication which describes the case when two surfaces are separated by a "thick" lubricant layer, ii) mixed lubrication between solid surfaces, and iii) boundary lubrication. The term boundary friction, introduced by Hardy et al. [8], refers to the friction generated when two surfaces are sheared in the presence of molecularly-thin lubricant films.

Centuries before that, Leonardo da Vinci studied the tribology in a wide variety of problems and found a relationship between friction force, F, and the normal load, L, which was later formulated by Amonton as follows

$$F = \mu L \tag{6.2}$$

where μ is the friction coefficient. Eq. (6.2) shows, that the friction force is directly proportional to the applied load and is independent of the area of contact. Amonton's law was modified by including an additional adhesive term to take in account attractive interactions that develop in the contact area between two surfaces [9], [10]. Bowden and Tabor [9] developed a model to describe the connection between friction force and the real area of contact A_r

$$F = \mu L + A_r S \tag{6.3}$$

where S is the shear strength. The heuristic value of this expression lies in its ability to account for the non-zero frictional force displayed by many systems when the external load vanishes. Therefore, attractive interactions in the contact area A between two surfaces need to be considered. No fundamental relationship has yet been established that links the frictional force between two surfaces at zero external load to the adhesive force between these surfaces.

In this chapter we will determine the friction force between an AFM tip and a lubricated carbon coated hard disk at zero normal load and investigate the contribution

of adhesion on the friction force. An AFM is used to address the relationship between the friction force F_F and the surface energy γ.

6.2.2 Adhesion and Surface Energy

Adhesion between two macroscopic bodies covered with a bulk liquid has been thoroughly investigated [3]. Derjaguin's approximation [11] expresses the adhesive force F_{adh} between two flat surfaces as the product of a geometric factor g and the work of adhesion W_{adh} [3], [11]

$$F_{adh} = gW_{adh} \tag{6.4}$$

For contact between two curved surfaces, the geometric factor g is given by

$g = 2\pi\left(\dfrac{R_1 R_2}{R_1 + R_2}\right)$, where R_1 and R_2 are the radii of curvature of the two surfaces. For the case of a sphere of radius R contacting a flat surface, the geometric factor reduces to $g = 2\pi R$.

The work of adhesion is defined by the Dupré equation [3]

$$W_{adh} = \gamma_1 + \gamma_2 - \gamma_{12} \tag{6.5}$$

where γ_1 and γ_2 are the free energies of the separated surfaces, and γ_{12} is the interfacial free energy. For bulk materials, the interfacial energy can be expressed as [3]

$$\gamma_{12} = \gamma_1 + \gamma_2 - 2(\gamma_1\gamma_2)^{1/2} \tag{6.6}$$

When the two surfaces are identical $(\gamma_1 = \gamma_2)$, the interfacial energy term vanishes, $\gamma_{12} = 0$, and the work of adhesion is given by $W_{adh} = 2\gamma$. This leads to the Bradley equation [12] for the adhesive force F_{adh} between two identical surfaces,

$$F_{adh} = 4\pi R \gamma \qquad (6.7)$$

This functional form of the adhesive force, which is also known as the Derjaguin, Muller and Toporov (DMT) model [13], is applicable to the adhesion between two rigid surfaces with high surface energy. When the contacting surfaces are elastic, the adhesive force is well approximated by the Johnson, Kendall and Roberts (JKR) model as [14]

$$F_{adh} = 3\pi R \gamma \qquad (6.8)$$

Comparing Eqs. (6.7) and (6.8), we observe that both equations predict a linear dependence of the adhesive force on the total surface energy. The difference between these two models leading to the equations is the form of the geometric factor, i.e., $g = 4\pi R$ for the DMT model and $g = 3\pi R$ for the JKR model.

In the case of two solid surfaces separated by a bulk liquid, the adhesive force increases as a result of meniscus formation [9]. The Laplace pressure generated in the liquid meniscus requires additional work to separate the surfaces. The Laplace pressure contribution to the adhesive force is given by [3]

$$F = g\gamma \cos\theta \qquad (6.9)$$

where θ is the angle made between the liquid film and the solid surfaces. Therefore, the total adhesive force required to separate two solid surfaces in the presence of a meniscus can be written as

$$F = g\gamma(1+\cos\theta) \tag{6.10}$$

In the present work, we measure simultaneously the surface energy γ of a carbon surface coated with a molecularly thin perfluoropolyether (PFPE) film and the adhesive force F_{adh} with an AFM tip (single asperity contact) as shown in Figure 6.1. From these data we can therefore determine, whether the theoretical relationships between adhesion force and surface energy are applicable for the case of surfaces separated by molecularly-thin liquid films.
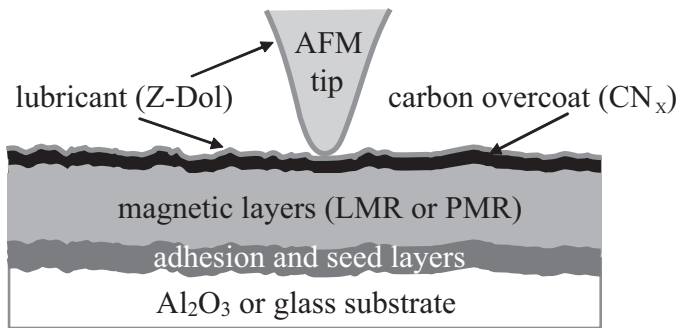
Figure 6.1: Schematic of the contact of an AFM tip on a flat, carbon coated magnetic disk surface separated by a molecularly thin lubricant film.

6.3   Experimental Procedure

6.3.1 Materials and Chemical Composition

The measurements were conducted on perfluoropolyether (PFPE)-lubricated magnetic recording disks comprised of an AlMg substrate, a cobalt-based magnetic film and a 3nm carbon (CN_X) overcoat. The RMS roughness of these surfaces was measured to be 0.27nm $\pm$ 0.03nm. The carbon surfaces were coated with hydroxyl-terminated perfluoropolyether (PFPE-OH), commercially known as Fomblin Z-Dol. This material is a random copolymer of perfluoromethylene oxide and perfluoroethylene oxide repeat units terminated on both ends by hydroxyl moieties,

$$HO\text{-}CH_2\text{-} CF_2 \text{--}O\text{-}(CF_2 CF_2O)_p\text{-}(CF_2O)_q\text{-} CF_2\text{-}CH_2\text{-}OH.$$
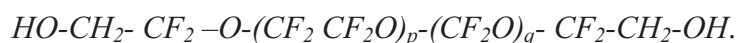
The PFPE-OH was fractionated prior to usage. Nuclear magnetic resonance spectroscopy was used to characterize the average molecular weight (2540amu) and polydispersity (1.07) of the PFPE-OH sample. Films were applied to the amorphous carbon surface via dip coating in dilute solutions of the PFPE-OH dissolved in perfluorohexane solvent [**15**].

Two different sets of samples were produced. In the first set, the PFPE-OH film thickness applied to the carbon surface was varied between 0.16nm and 2.31nm. The thickness was controlled by varying the PFPE-OH concentration in the perfluorohexane solution, the pull-rate, or both. The applied film thickness was determined using Fourier transform infrared spectroscopy (FTIR). The thickness values obtained from FTIR spectroscopy where calibrated with measurements made using X-ray reflectivity [**16**], an accurate method for determine film density and

thickness. All samples studied in this work were at thicknesses below the "critical de-wetting" thickness [17], [18], which was determined to be 2.3nm ± 0.1nm for the materials used.

A second set of samples was prepared in which the bonding ratio of the total PFPE-OH film was varied between 15% and 93% at a constant film thickness. These samples were prepared in the following way. After the dip-coating of the disks, the bonding of the PFPE-OH films on the disk surface was increased via annealing at elevated temperatures (typically 90˚C) for different times. Thereafter, the target film thickness was determined using FTIR [16]. The target thickness was on the order of 1.05nm ± 0.05nm. Solvent extraction was used on one of the disks each time to remove the mobile component of the PFPE-OH film from the surface. Subsequently, the film thickness of the remaining bonded film was measured. The bonding ratio is defined the thickness of the bonded PFPE-OH film divided by the total film thickness [7].

6.3.2 Surface Energy Measurements

The surface energy of the PFPE-OH coated carbon surfaces was determined using contact angle goniometry [3], [4], [6] (VCA Optima – AST Products, Inc.). The dispersive and polar surface energy components of the PFPE films, γ_s^d and γ_s^p, were obtained from contact angle measurements performed using hexadecane $\left(\gamma_L^d = 27.5\,mJ/m^2\right)$ and water $\left(\gamma_L^d = 21.8\,mJ/m^2, \text{ and } \gamma_L^p = 51.0\,mJ/m^2\right)$ as the

reference liquids [5], [7]. The following experimental procedure was used. First, a droplet of the reference liquid was placed on the surface and an image of the droplet was captured immediately using a CCD camera. Then, the contact angle was determined and the results were averaged over four measurements.

6.3.3 AFM Friction Measurements

The determination of friction on the micro- and nano-scale is of importance for micro/nano electro-mechanical systems (MEMS, NEMS) [19], [20], [21] and magnetic recording devices [22]. The atomic force microscope (AFM) can be used as a friction force apparatus on the nano-scale [23].

Friction force measurements were performed with a commercially available atomic force microscope (Pacific Nanotechnology). The friction force F_F was determined from the magnitude of the cantilever torsion generated during sliding the AFM tip back and forth (trace and retrace) on the sample surface coated with a molecularly-thin PFPE lubricant film. The AFM tip was brought into contact with the surface and kept at a distance just below the "snap into contact" point, where the tip is first in contact with the surface. Therefore, no normal force was applied.

Since torsion calibration of an AFM cantilever is very complex and would not contribute to this study, the friction force was measured in arbitrary units as a cantilever torsion signal. Figure 6.2 shows a friction loop where the friction force (in arbitrary units) was plotted against the displacement in a trace and retrace motion.

The solid lines show the average friction value for the trace and the retrace in arbitrary units. The friction values were averaged over four measurements conducted on different areas.
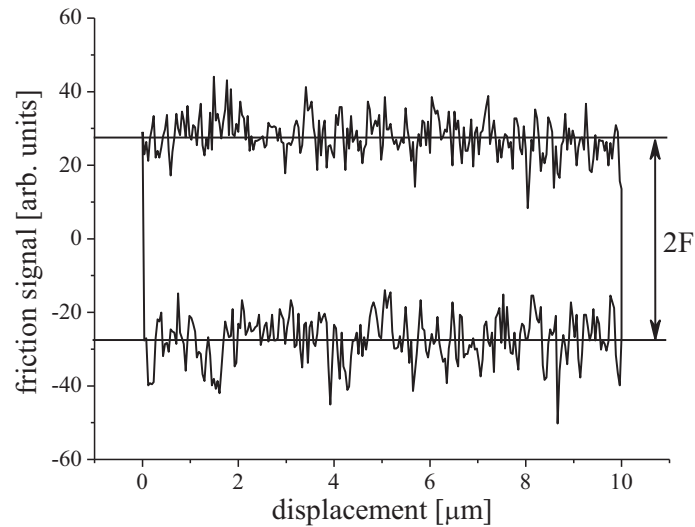
Figure 6.2: Friction loop to measure friction signal in arbitrary units

6.3.4 AFM Adhesion Measurements

Force-distance measurements with an atomic force microscope (Nanosurf, Mobile S) were used to measure the adhesive force between the PFPE lubricated carbon surface and the AFM tip. A typical force-distance measurement is shown in Figure 6.3 where an approach and retract cycle of the AFM tip is performed: During a measurement, the AFM tip is first brought into close proximity to the surface (line 1)

by lowering the cantilever towards the sample surface. At point (2), the AFM tip "snaps" into contact with the sample surface due to attractive van der Waals forces, deflecting the cantilever downward. Further approach results in an upward cantilever deflection and a small normal force applied to the sample surface (3). Subsequently, the cantilever is retracted from the sample surface (4). The AFM tip stays initially in contact with the sample surface due to adhesion forces, bending the cantilever downward. The AFM tip separates when the pull-off force exceeds the adhesion force between tip and surface (point 5). At point (6) the AFM is fully detached from the surface and the cantilever shows zero deflection. The magnitude of the cantilever deflection at point (5) is proportional to the adhesive force. The adhesion force values were determined by averaging the results of four force-distance measurements and multiplying the cantilever deflection with the cantilever spring constant of 0.2 N/m.
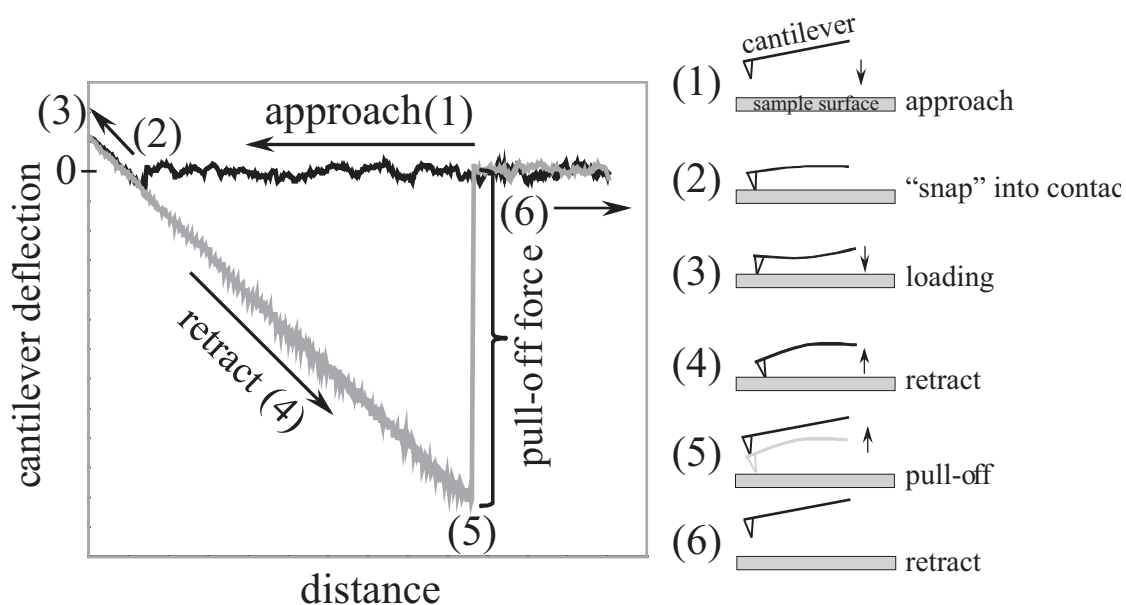
Figure 6.3: Typical data from a force-distance measurement.

Prior to all adhesion measurements, the AFM tip was brought into contact with the surface for a period of approximately 15 minutes to allow the tip to come into equilibrium with the PFPE-OH coated surface.

6.4 Results and Discussion

6.4.1 Surface Energy

The results of the surface energy measurements conducted on the PFPE-OH films of varying thickness are summarized in Figure 6.4a) and b). As shown in Figure 6.4a), the dispersive surface energy component of the PFPE-OH coated surface γ_S^d depends strongly on the applied PFPE-OH film thickness. In addition, we observe that the dispersive surface energy decreases monotonically with increasing film thickness, asymptotically approaching the value of the bulk PFPE-OH liquid $\gamma_{bulk}^d = 15.6 \, \text{mJ/m}^2$, for the thickest films studied. The dependence of the dispersive surface energy on film thickness $\gamma^d(h)$ was shown in Eq. (6.1) [7]. It is apparent that the minimum surface energy is equal to that of the bulk value (γ_{bulk}^d) of Z-Dol [17]. The thickness dependence of this quantity, which we termed the excess surface energy $\Delta\gamma^d(h)$, can be described using [6], [24]

$$\Delta\gamma^d(h) = \frac{A^*}{12\pi(h+d)^2}$$

(6.11)

where A^* is the effective Hamaker constant, and d is a constant. The fit to the data presented in Figure 6.4a) was obtained using $\gamma_{bulk}^d = 15.6\,\text{mJ/m}^2$, $A^* = 4.8\,\text{x}\,10^{-20}$ J and $d = 0.17\text{nm}$. These results are consistent with those previously reported elsewhere [24].

The dependence of the polar surface energy component γ^p on PFPE-OH film thickness is shown in Figure 6.4b). We observe that the polar surface energy also decreases with increasing film thickness, approaching a minimum of 5.5 mJ/m^2 for the thickest films studied. This dependence is very similar to previous results on PFPE-OH films in which a minimum in the value of the surface energy is observed at a thickness corresponding to one monolayer [4], [5].
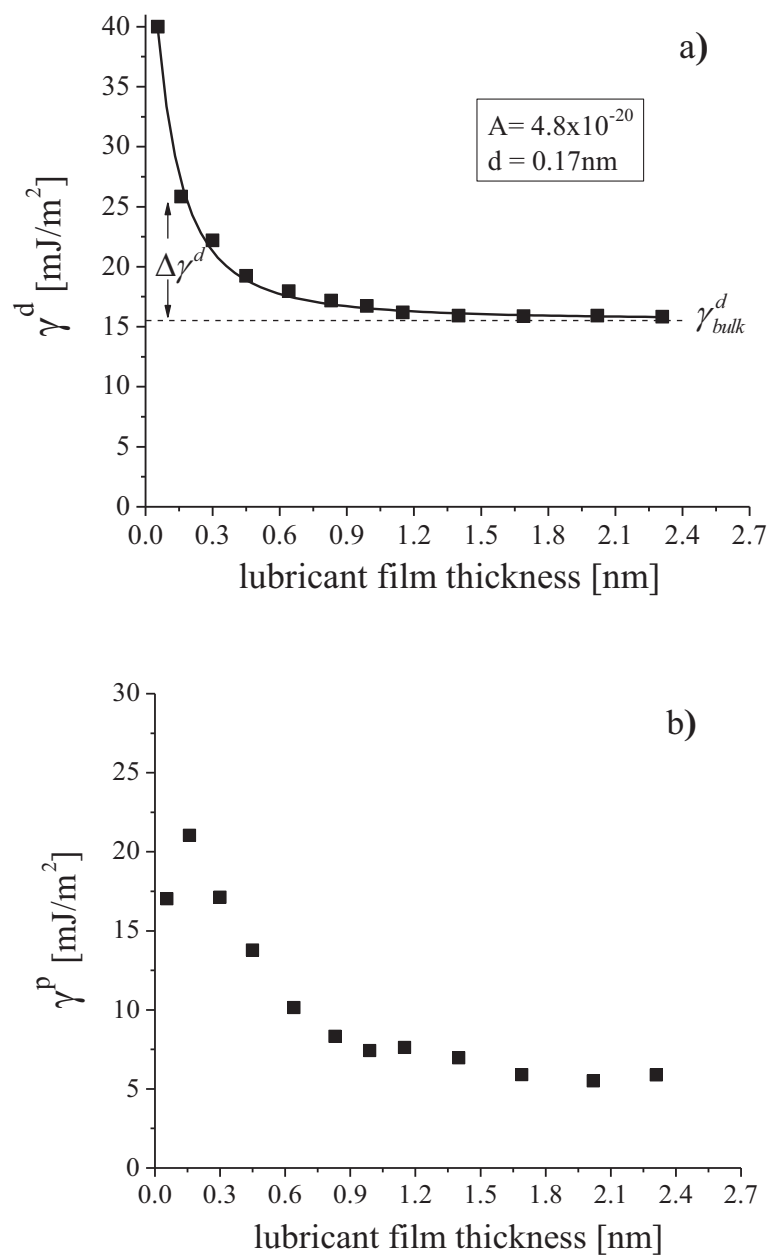
Figure 6.4: a) Dispersive surface energy component, γ^d, for Z-Dol 2450 on a carbon

coated surface as a function of Z-Dol film thickness. Solid line fit to the data is based

on Eq. (6.11) using an effective Hamaker constant of $A^* = 4.8 \times 10^{-19}$J. The dashed

line at 15.6mN/m^{-2} denotes the bulk value of the dispersive surface energy, γ_{bulk}^{d}. b)

Polar surface energy, γ^{p}, as a function applied Z-Dol film thickness.

The dependence of the surface energy components on the PFPE-OH bonding ratio was also investigated. These results are shown in Figure 6.5a) and b). As shown in Figure 6.5a), the dispersive surface energy component is found to be nearly independent of the bonding ratio. The polar component of the surface energy (Figure 6.5b), however, decreases rapidly with increasing bonding ratio and approaches $\gamma_{\min}^{p} = 0.5 \pm 0.5 mJ / m^{2}$ at 100% bonding of the film. The drop in γ^{p} with increasing bonding ratio has been interpreted by Waltman et al. [4] in terms of attractive hydrogen-bonding between the hydroxyl end-groups and the polar sites on the carbon surface. In particular, they suggested that an increase in the bonding ratio results in a reduction of the number of "free", or non-interacting, hydroxyl end-groups of the PFPE lubricants as well as the number of polar surface sites. This neutralization of polar sites in the lubricant and on the carbon surface appears to be responsible for the experimentally observed reduction in the polar surface energy component.
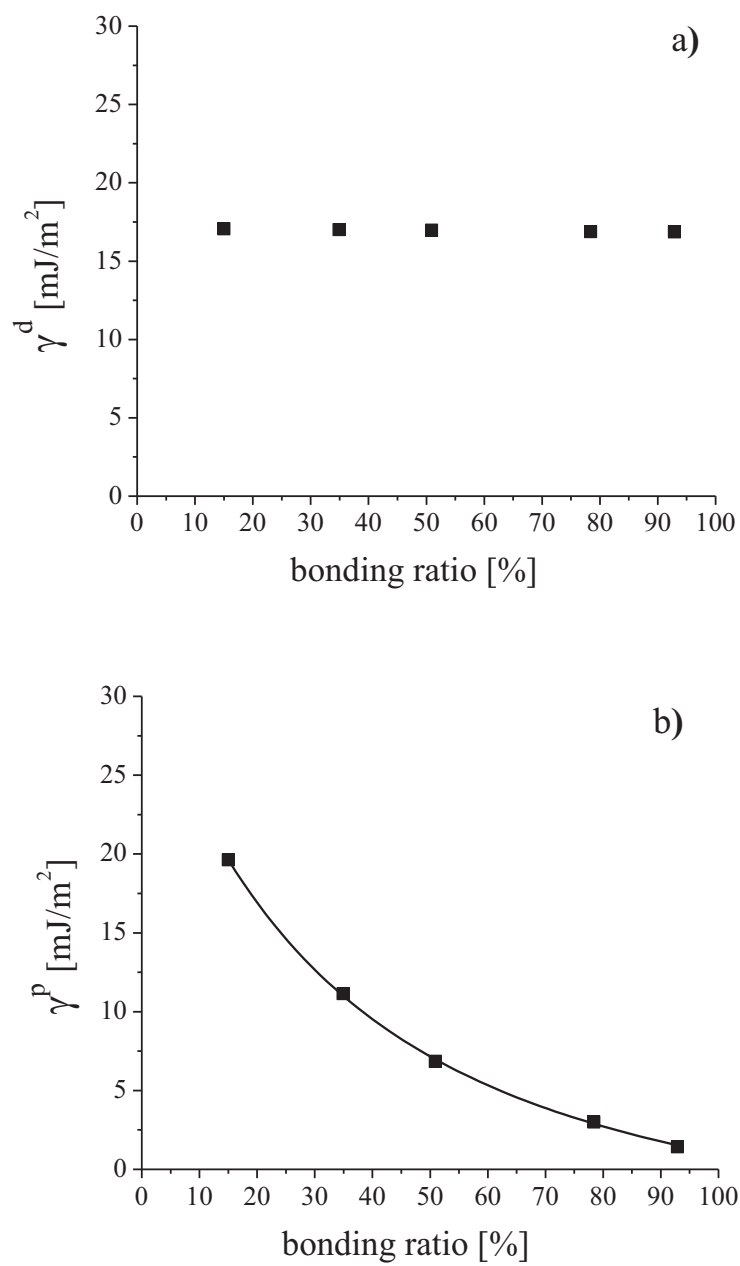
Figure 6.5: The dispersive (a) and polar (b) surface energy components as a function

of bonding ratio for 1nm Z-Dol 2540 films.

In analogy to Eq. (6.1), we can express the total polar surface energy as:

$$\gamma^p = \gamma^p_{min} + \Delta\gamma^p \qquad (6.12)$$

where γ^p_{min} corresponds to the carbon-PFPE system at complete saturation of the polar sites (100% bonding of the film). Based on our experimental measurements, this results in a minimum polar surface energy of $\gamma^p_{min} = 0.5 \pm 0.5 mJ/m^2$ i.e., γ^p_{min} is negligible in comparison to $\Delta\gamma^p$. Thus, Eq. (6.12) becomes $\gamma^p = \Delta\gamma^p$.

6.4.2 Adhesion

Force-distance measurements were conducted on both sets of PFPE coated surfaces. The magnitude of the cantilever deflection at the point of separation from the surface was found to be strongly dependent on both the PFPE-OH film thickness and the bonding ratio. The dependence of adhesion on film thickness is shown in Figure 6.6a), and the dependence of adhesion on the bonding ratio is shown in Figure 6.7a). As is apparent from these figures, the adhesion between the AFM tip and the coated surface decreases with both increasing PFPE-OH film thickness and increasing bonding ratio. The adhesion results are qualitatively compared with the corresponding total surface energies (the sum of the polar and dispersive surface energy component) in Figure 6.6b) for film thickness and Figure 6.7b) for bonding ratio.
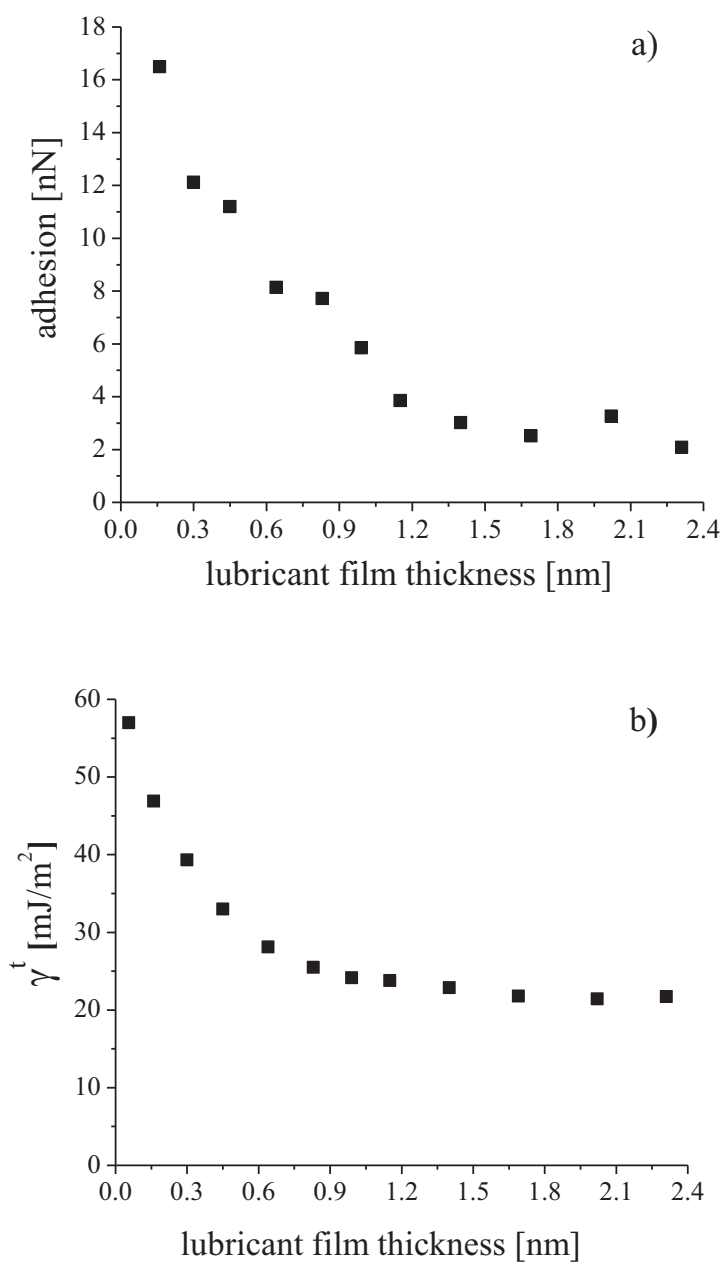
Figure 6.6: (a) Adhesion force compared to (b) the total surface energy γ^t (sum of dispersive and polar component) as a function of the applied film thickness of Z-Dol 2540.
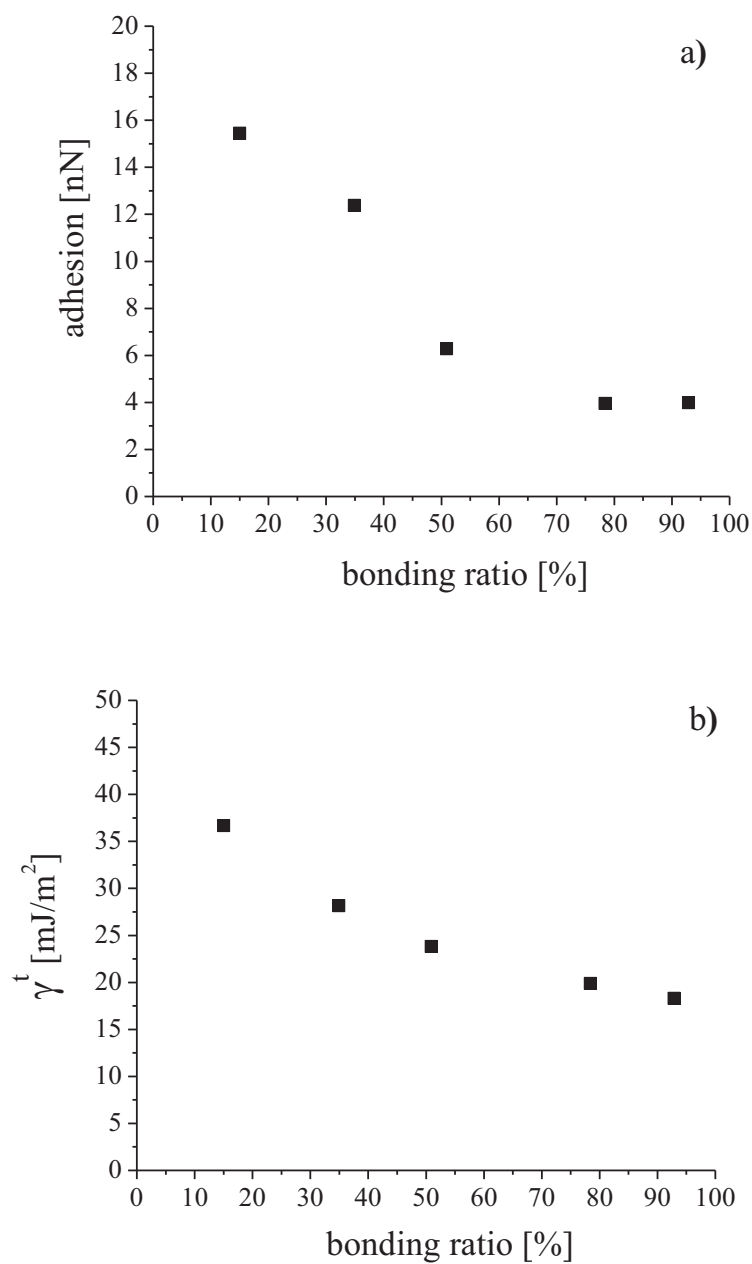
Figure 6.7: The adhesion force (a) compared to the total surface energy γ^t (b) (sum of dispersive and polar component) as a function of the bonding ratio for 10Å Z-Dol 2540 films.

The results indicate a strong correlation between the surface energy of the PFPE-OH coated surfaces and the adhesion measurements.

The dependence of adhesion force on total surface energy of the film is shown in Figure 6.8 for both sets of PFPE films (lubricant thickness and bonding ratio) studied. We observe a nearly linear dependence between adhesion force and total surface energy. We note that the slope of the line for the PFPE-OH bonding ratio data is approximately 30% steeper than that for the thickness data. We believe that this result is related to the difference in the radii of the AFM tips that were used for the two experiments. In particular, the AFM tip radius that was used to collect the adhesion data of the PFPE-OH bonding ratio samples was approximately 30% larger (which results in a 30% increase in the geometric factor g) than that used for the PFPE-OH thickness samples.

While the observed linear relationship between surface energy and adhesion is consistent with that predicted by adhesion theory, the results of the present work illustrate that adhesion between surfaces separated by molecularly-thin PFPE films vanishes at a finite value of the surface energy (Figure 6.8). This observation differs from the predictions obtained using the theoretical results from the DMT model or the JKR model. In particular, the DMT and JKR models both predict that adhesion vanishes only when the surface energy goes to zero. This is shown schematically by the dashed line in Figure 6.8.
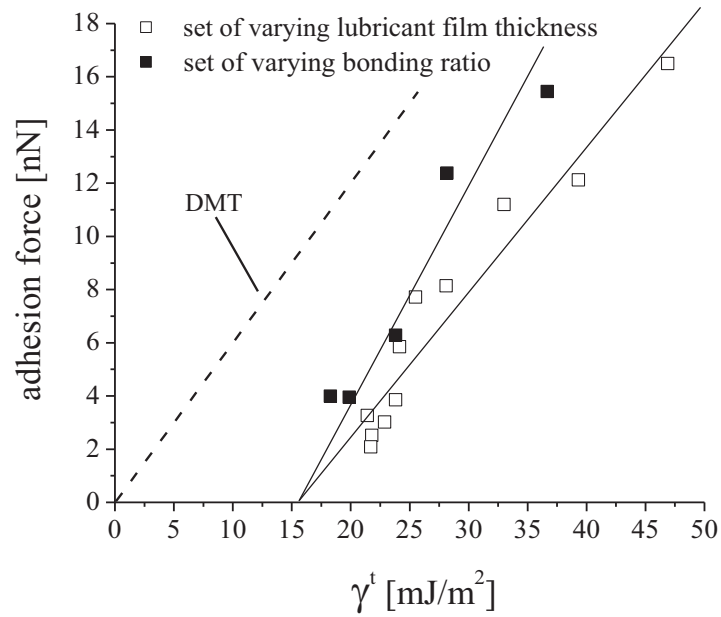
Figure 6.8: Adhesion force vs total surface energy for varying film thickness (□), and

varying bonding ratios (■) of Z-Dol 2540 films. The dashed line illustrates an

example of the DMT or JKR model.

The results provided in Figure 6.8 indicate that the adhesion in molecularly-

thin films does not scale with the total surface energy γ^T. Extrapolation of the

experimental data indicates that the adhesive force between the AFM tip and the

PFPE-OH coated surface vanishes at approximately $15-16\,mJ/m^2$. This value is

nominally equivalent to $\gamma_{bulk}^d + \gamma_{min}^p$. Consequently, our data suggests that the adhesive

force scales as the excess surface energy $\Delta\gamma = \Delta\gamma^d + \Delta\gamma^p$. This can be shown by

plotting the adhesion versus $\Delta\gamma$. As shown in Figure 6.9, the adhesion decreases

linearly with decreasing $\Delta\gamma$, approaching zero as the excess surface energy vanishes.

We note that the quantity F_{adh}/g was normalized arbitrarily with the highest value of adhesion measured. These results indicate that the adhesion between two surfaces separated by a molecularly-thin PFPE-OH film can be described by the following relationship:

$$F_{adh} = g\Delta\gamma \tag{6.13}$$

where $\Delta\gamma$ is the total excess surface energy $(\Delta\gamma = \Delta\gamma^{d} + \Delta\gamma^{p})$ of the molecularly thin PFPE lubricant.
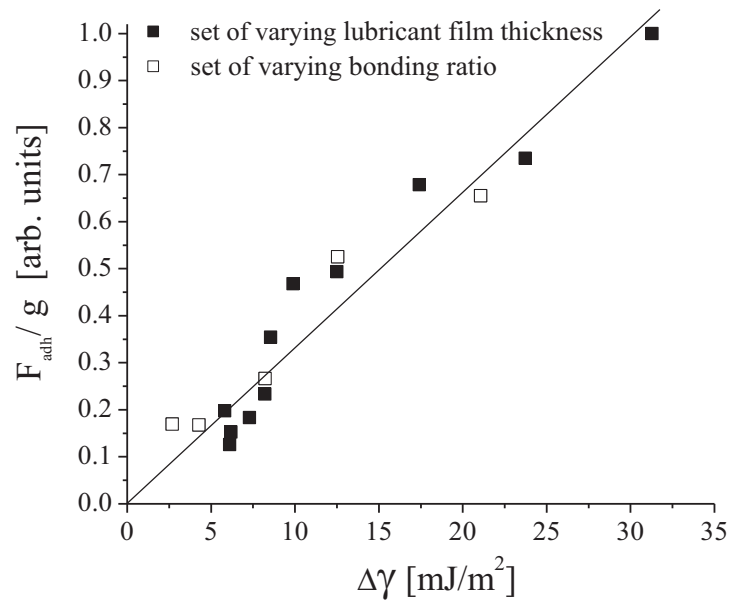
Figure 6.9: The quantity F_{adh}/g was normalized arbitrarily to 1 for the highest adhesion measured as a function of the sum of the excess surface energy of the dispersive and polar component, $\Delta\gamma^{d} + \Delta\gamma^{p}$.

6.4.3 Friction

The dispersive and polar surface energy components were compared to the friction value obtained from the cantilever torsion during contact measurements. Figure 6.10 shows the friction force (in arbitrary units) at zero external normal load as a function of a) lubricant thickness and b) bonding ratio. A strong dependence exists between the friction force and the film thickness and between friction force and film bonding ratio.

The friction force (in arbitrary units) is plotted versus the total surface energy $\gamma = (\gamma^d + \gamma^p)$ in Figure 6.11. The graph includes the data from disks where the total Z-Dol film thickness applied to the disk was changed, and the disks where the bonding ratio of the Z-Dol film was varied. We observe from

Figure 6.11, that a linear dependence of friction versus total surface energy exists for all experimental data. Extrapolation of the linear least squares fit of the data is shown as solid lines. We find that the friction goes to zero at a finite value of the surface energy. The value of the surface energy at this point is nominally 15 ± 1 mJ/m^2. Within an experimental error of approximately 25%, the observed value is linear dependent on the sum of the surface energy in excess of the bulk $\gamma^d_{bulk} + \gamma^p_{min}$. Figure 6.12 shows the friction signal normalized against the highest friction measured as a function of the excess surface energy.
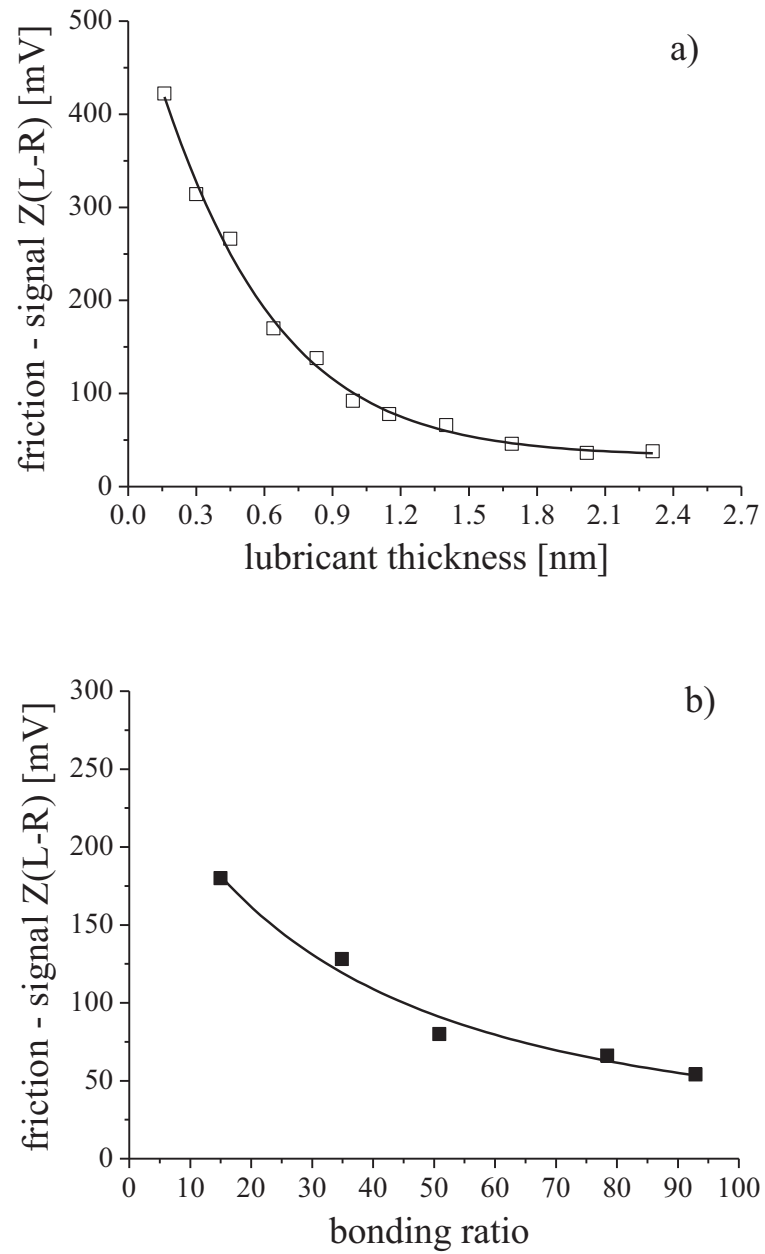
Figure 6.10: Friction signal vs. film thickness (a) and bonding ratio (b)

We observe from Figure 6.12 that the friction force in molecularly-thin boundary lubricant films depends linearly on the excess surface energy as

$$F_F = g * (\Delta\gamma^d + \Delta\gamma^p) \tag{6.14}$$

where $g*$ is a constant. The form of Eq. (6.14) describing the friction force at zero load is analogous to that previously derived for the adhesion between two surfaces separated by a molecularly thin film. In both cases the parameter governing adhesion and friction is the excess surface tension.
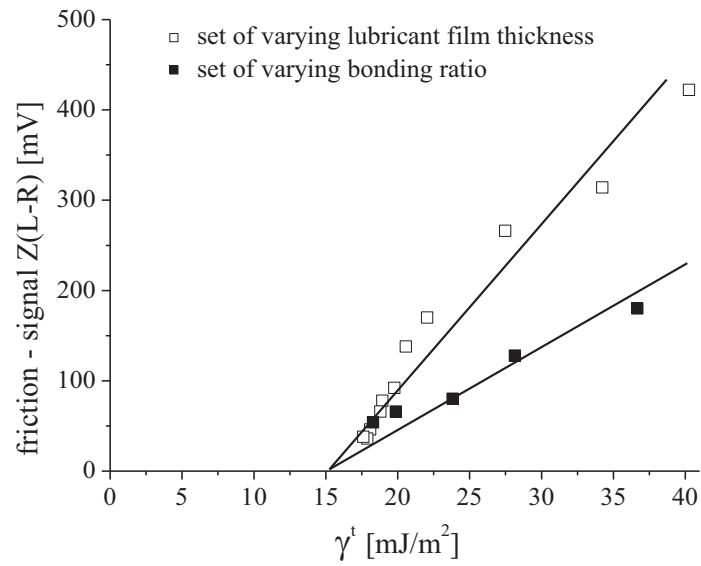
Figure 6.11: Friction signal vs. total surface energy for both sets of disks at varying lubricant film thickness and bonding ratio
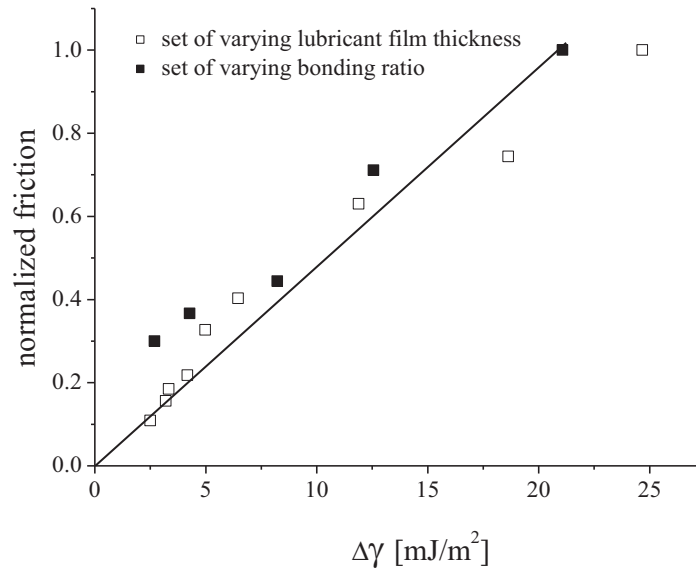
Figure 6.12: Normalized friction signal vs. excess surface energy $\Delta\gamma$ for disk with varying film thickness and lubricant bonding ratio

6.5 Conclusions

A number of conclusions concerning adhesion and friction between surfaces separated by molecularly thin films can be drawn from the experimental results shown in this section. The measurements show that there is no evidence for meniscus formation at the contact. The pull-off force curve (as shown in Figure 6.3) does not show meniscus formation. This is consistent with previous surface force apparatus results on molecularly-thin PFPE films [25], [26], [27] where no evidence of meniscus formation was found.

Another conclusion that immediately follows from Eqs. (6.13) and (6.14) is that the magnitude of adhesive force does not depend upon the work required to form two interfaces. An explanation for this phenomenon is as follows. The lubricant is distributed uniformly over the entire disk surface with a film thickness h and is thermodynamically stable, i.e., the disjoining pressure in the lubricant equilibrates over the entire surface. During the initial contact of the AFM tip with the lubricated surface (for a duration of approx. 15 min), lubricant material was slowly transferred from the surface to the AFM tip until the free surface energies of both surfaces are equal. This is driven by the disjoining pressure in the lubricant. Therefore, the lubricant film thickness at the contact is $2h$ (twice the lubricant film thickness of Z-Dol on the disk surface) between the AFM tip and the surface. At separation of the AFM tip, we assume that the lubricant thickness is h on both the disk and the AFM tip due to conservation of mass and the principle of minimum energy. At separation, the molecules of the lubricant on both surfaces interact only on one side (away from the surface) with their neighbors. Interfaces normal to the surfaces are shown in Figure 6.13a). When the surfaces are brought together the normal interfaces start to disappear due to interactions between the lubricant molecules on the tip and on the surface. At the same time, an energy gradient in the transverse direction around the contact starts to form which eventually creates an interface in the transverse direction (see Figure 6.13b). Upon contact, each surface interacts with the molecularly-thin PFPE film on the counter-surface, and generates overlapping surface forces [3], [11]. The interface in normal direction disappears and interfaces in transverse direction are formed due to the gradient of interaction between the lubricant molecules inside the

contact and outside the contact (see Figure 6.13b). Once the surfaces are separated, no net work is required to form new normal interfaces. However, work is needed to overcome the overlapping surface forces at separation. This work can be approximated by the integral of the disjoining pressure, where the boundaries are the lubricant thickness in the contact ($2h$) and the film thickness on each surface after separation (h),

$$W = 2 \int_{2h}^{h} \Pi(l) dl = -2 \int_{2h}^{h} \frac{A*}{6\pi l^3} dl = \frac{3A*}{24\pi h^2} \tag{6.15}$$

Eq. (6.15) shows a direct relation between the work of adhesion (due to the overlapping surface forces) and the dispersive excess surface energy $\Delta\gamma^d(h)$ (compare to Eq. (6.12)). Using Eq. (6.12), one can estimate the work required to separate the two surfaces, which would be on the order of $W = 3\Delta\gamma^d(h)$. In addition, interactions between the solid surface of the disks and the AFM tip may be present; however, these interactions are negligible compared to the interaction of the lubricant.
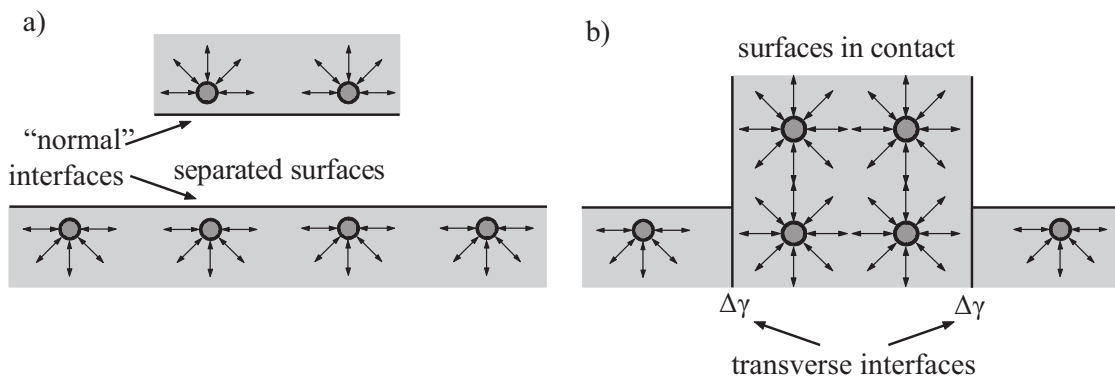
Figure 6.13: Interaction of molecules at surface interfaces for a) separated surfaces, b) surfaces in contact

It is shown that the excess surface energy dictates the work of adhesion of two surfaces separated by a molecularly-thin film. The friction at zero normal load and adhesion between two surfaces separated by a molecularly-thin boundary layer films differ from that expected on the basis of classical theories, such as DMT and JKR. The experimental results reported suggest that a modification of the classical adhesion theory is necessary to describe the adhesion between surfaces separated by molecularly-thin liquid films. Specifically, we find that the friction at zero normal load and the adhesion are dictated by the excess surface energy $\Delta\gamma$ and not the total surface energy γ^T.

6.6 Acknowledgement

This chapter is a partial reprint of material as it appears in:

"Adhesion between surfaces separated by molecularly-thin perfluoropolyether films", by R. Brunner, G.W. Tyndall, R.J. Waltman, F.E. Talke, submitted for publication to Tribology Letters (2009).

The dissertation author was the primary researcher and author and the co-authors listed in this publication directed and supervised the research which forms the basis for this chapter.

Bibliography

[1] B. Bhushan, *Nanotribology and nanomechanics – an introduction*. Heidelberg: Springer, 2005.

[2] Y. Shinji and J. Israelachvili, "Friction and adhesion hysteresis of fluorocarbon surfactant monolayer-coated surfaces measured with the surface forces apparatus," *J. Phys. Chem. B*, vol. 102, pp. 234-244, 1998.

[3] J.N. Israelachvili, *Intermolecular and surface forces, 2nd edition*. London: Academic Press, 1991.

[4] R.J. Waltman, D.J. Pocker, and G.W. Tyndall, "Studies on the interactions between ZDOL perfluoropolyether lubricant and the carbon overcoat of rigid magnetic media," *Trib. Lett.*, vol. 4, pp. 267-275, 1998.

[5] G.W. Tyndall, P.B. Leezenberg, R.J. Waltman, and J. Castenada, "Interfacial interactions of perfluoropolyether lubricants with magnetic recording media," *Trib. Lett.*, vol. 4, pp. 103-108, 1998.

[6] R.J. Waltman, "The interactions between Z-Tetraol perfluoropolyether lubricant and amorphous nitrogenated- and hydrogenated-carbon surfaces and silicon nitride," *J. Fluo.Chem.*, vol. 125, pp. 391-400, 2004.

[7] R.J. Waltman, B.K. Yen, and R.L. White, "The adhesion of monomolecular hydroxyl-terminated perfluoropolyether liquid films on the sputtered silicon nitride surface as a function of end group acidity and mobility," *Trib. Lett.*, vol. 20, no. 1, pp. 69-81, 2005.

[8] W.B. Hardy, "Problems of the Boundary State," *Phil. Trans. Roy. Soc. A*, vol. 230, p. 1, 1931.

[9] F.P. Bowden and D. Tabor, *The friction and lubrication of solids*. Oxford: Oxford University Press, 1950.

[10] A. Berman, C. Drummond, and J. Israelachvili, "Amonton's law at the molecular level," *Trib. Lett.*, vol. 4, p. 95, 1998.

[11] B.V. Derjaguin, "Untersuchungen über die Reibung und Adhäsion, IV: Theorie des Anhaftens kleiner Teilchen," *Kolloid Z.*, vol. 69, pp. 155-164, 1934.

[12] R.S. Bradley, "The cohesive force between solid surfaces and the surface energy of solids," *Phil. Mag.*, vol. 13, p. 853, 1932.

[13] B.V. Derjaguin, V.M. Muller, and Y.P. Toporov, "Effect of contact deformations

on adhesion of particles," *Coll. Int. Sci.*, vol. 53, p. 314, 1975.

[14] K.L. Johnson, K. Kendall, and A.D. Roberts, "Surface energy and contact of elastic solids," *Proc. Roy. Soc. London, Ser. A*, vol. 324, p. 301, 1971.

[15] C. Gao, Y.C. Lee, J. Chao, and M. Russak, "Dip-coating of ultra-thin liquid lubricant and its control for thin-film magnetic hard disks," *IEEE Trans. Magn.*, vol. 31, no. 6, pp. 2982-2984, 1995.

[16] M.F. Toney, C.M. Mate, and K.J. Pocker, "Calibrating ESCA and ellipsometry measurements of perfluoropolyether lubricant thickness," *IEEE Trans Magn.*, vol. 34, no. 4, p. 17741776, 1998.

[17] R.J. Waltman, A. Khurshudov, and G.W. Tyndall, "Autophobic dewetting of perfluoropolyether films on amorphous-nitrogenated carbon surfaces," *Trib. Lett.*, vol. 12, no. 3, pp. 163-169, 2002.

[18] R.J. Waltman, "The stability of ultra-thin perfluoropolyether mixture films on the amorphous nitrogenated carbon surface," *J. Coll. Int. Sci.*, vol. 313, pp. 608-611, 2007.

[19] H. Liu and B. Bhushan, "Nanotribological characterization of molecularly thick lubricant films for applications to MEMS/NEMS by AFM," *Ultramicroscopy*, vol. 97, pp. 321-340, 2003.

[20] B. Bhushan, *Principles and applications of tribology*. New York: Willey, 1999.

[21] B. Bhushan and A.V. Kulkarni, "Effect of normal load on microscale friction measurement," *Thin Solid Films*, vol. 278, pp. 49-56, 1996.

[22] C.M. Mate et al., "Dynamics of contacting head-disk interfaces," *IEEE Trans. Magn.*, vol. 40, no. 4, pp. 3156-3158, 2004.

[23] C.M. Mate, G.M. McClelland, R. Erlandsson, and S. Chiang, "Atomic-scale friction of a tungsten tip on a graphite surface," *Phys. Rev. Lett.*, vol. 59, pp. 1942-1945, 1987.

[24] R.J. Waltman, G.W. Tyndall, and J. Pacansky, "Computer-modeling study of the interactions of Zdol with amorphous carbon surfaces," *Langmuir*, vol. 15, pp. 6470-6483, 1999.

[25] M. Ruths and S. Granick, "Rate-dependent adhesion between opposed perfluoropoly(alkyl ether) layers: dependence on chain-end functionality and chain length," *J. Phys. Chem. B*, vol. 102, pp. 6056-6063, 1998.

[26] H.M. Stanley, I. Etsion, and D.B. Bogy, "Adhesion of contacting rough surfaces in the presence of sub-boundary lubrication," *J. Trib. Trans. ASME*, vol. 112, pp. 98-104, 1990.

[27] R.J. Waltman and G.W. Tyndall, "Lubricant and overcoat systems for rigid magnetic recording media," *J. Magn. Soc. Jap.*, vol. 26, no. 3, pp. 97-108, 2002.

7 Surface Energy of Nano-structured Discrete Track Recording Media

Surface energy of discrete track recording (DTR) media with a molecularly-thin perfluoropolyether film was determined on the nano-scale from pull-off force measurements using atomic force microscopy (AFM). The method is based on correlating pull-off forces measured in arbitrary units on a nano-structured surface with pull-off forces measured on macroscopically smooth dip-coated gage surfaces with known surface energy. The method avoids the need for complex calibration of the AFM cantilever stiffness and the determination of the radius of curvature of the AFM tip. Both of the latter measurements are associated with indirect and less accurate measurements of surface energy based on various contact mechanics adhesion models.

7.1 Manufacturing of Patterned Media

First, the manufacturing process of patterned media using nano-imprint lithography (NIL) technology is explained. This process uses a master template or replica to transfer the pattern onto the magnetic disk. Nano-imprint lithography can be used for both discrete track recording and bit-patterned media.

7.1.1 Master Fabrication

Nano-imprint lithography requires the manufacturing of a master disk using E-beam lithography [**1**]. Figure 7.1 shows two examples for the fabrication of a master disk on a six inch diameter quartz wafer. Depending on the manufacturing of replicas and the final magnetic disks, there are two types of master "polarities", a pillar (a) and a hole (b) structure.

For the pillar structure (a), a conducting layer (for example tantalum (Ta)) and a negative photo resist (HSQ) are deposited on the wafer. Then, a pattern is written into the photo resist using e-beam lithography. The unexposed HSQ negative photo resist is removed (I). Reactive ion etching (RIE) is used to etch into the conducting layer of Ta (II). In a second step, Ta is used as the hard mask and the quartz wafer is etched, resulting in a pillar master (III). Finally, the Ta mask is removed from the wafer (IV) by wet etch processes, which leaves less contamination on the surface compared to RIE.

For the hole structure (b), a hard mask layer (for example chrome (Cr)) and a positive resist (ZEP) are applied to the substrate. The pattern is written into the positive resist using E-beam lithography. Then, the exposed positive photo resist is removed (I) and the hard mask layer of Cr is etched via RIE (II). Finally, the quartz substrate is etched, and the remain positive photo resist is removed (III). In the end, the Cr hard mask layer is removed (IV) and the hole master is produced.

substrate
(for example quartz)

conducting layer (for example: Ta)
or hard mask layer (for example: Cr)

deposition of HSQ or ZEP +
E-beam patterning

E-beam

a)

negative resist:
remove unexposed HSQ

etching Ta layer
remove exposed HSQ

etching substrate

pillar master

remove Ta layer

I

II

III

IV

b)

positive resist:
remove exposed ZEP

III

hole master

etching into
Cr hard mask
layer

etching into
substrate
and remove
ZEP

remove Cr

side view

I

II

IV

IV

Figure 7.1: Fabrication process of a) pillar master and b) hole master (after [**1**]).

The pillar or hole master can be used for nano-imprint lithography of either a replicate or prototype magnetic disk, respectively. In either way, the master controls the subsequent nano-imprint process. Therefore, the quality of the master is a key factor in the disk manufacturing process. As the size of the pattern decreases, more manufacturing problems appear and great care is needed to minimize defects.

7.1.2 Nano-imprint Lithography of Discrete Track Recording Media

The master that is used for the samples in this chapter has discrete tracks and grooves for the manufacturing of discrete track recording media. The process begins

with a substrate that is coated with a soft magnetic under layer (SUL), an interlayer, and the CoCrPt recording layer, similar to continuous perpendicular magnetic recording, described in Chapter 1. A transfer-layer is applied on top of the magnetic layer by spin coating. The transfer layer is a monomer with very low viscosity that hardens under UV exposure. The master template is coated with a release layer.

After the appropriate coatings are applied, the master is pressed uniformly onto the magnetic recording disk (see Figure 7.2a). The transfer layer fills the patterned structure of the master and is cured by exposing to UV light (b). Then, the master template is removed from the disk (c). The release layer ensures a residue free lift-off of the master template. The structured monomer provides a hard mask for the reactive ion etching process of the magnetic layer (d). The grooves etched into the recording layer have to be deep enough to separate the tracks magnetically and physically to eliminate transition noise from adjacent tracks to overcome the super paramagnetic effect [2], [3]. The monomer thickness is also reduced during the etching process and the remains are subsequently removed. The process is finalized after a carbon overcoat is applied to the entire disk (f).
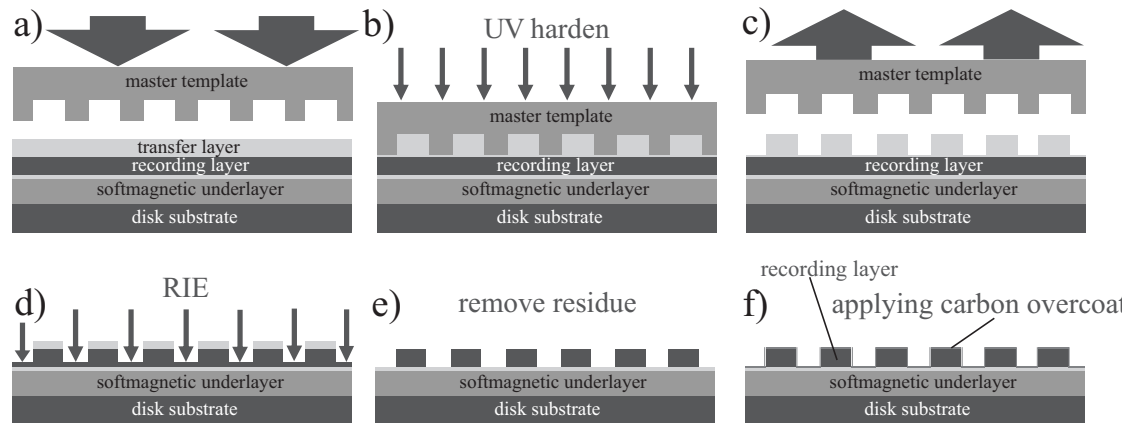
Figure 7.2: Process flow of the nano-imprint manufacturing of discrete track recording media (after [**4**])

7.1.3 Challenges of Discrete Track Recording

Patterning of the magnetic recording layer of a hard disk is difficult but offers great advantages in the magnetic properties which include the following [**4**], [**5**]. The separation of bits or tracks via grooves or island structure enhances the signal to noise ratio [**6**]. The so-called cross-talk of adjacent tracks is smaller than in continuous media. In addition, the write poles can be wider than the written track or bit, thus reducing transition noise in the recording layer. Figure 7.3 shows an SEM image of a discrete track recording medium. The light area is the land and the dark area is the groove. However, defects that connect two adjacent tracks or bits can distort the surrounding area and make it unusable for magnetic recording. These defects can possibly originate from remains of the transition layer in the master or impurities on the disk. In Figure 7.3 a typical defect is visible on the right.

In addition to magnetic difficulties, discrete track recording (as well as patterned media) is a technology with great tribological challenges [7]. Furthermore, lubricant spreading, surface energy variations and corrosion of the media are of concern. Planarization of the media to simulate the topography of continuous media is desirable for stable flying characteristics of the slider [8], [6]. In addition, intermolecular forces between the slider and the land areas of discrete track recording media become increasingly more important with a reduction in flying height and must be considered in the design of the head/disk interface. Intermolecular forces in the groove and land areas are very important with respect to lubricant migration and lubricant spin-off.
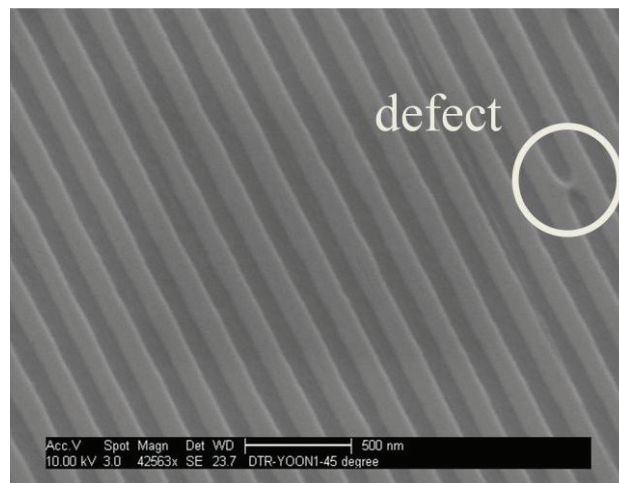
Figure 7.3: SEM image of a discrete track recording medium

Fukuzawa et al. **[9]** investigated the lubricant thickness distribution of layered surfaces used in DTR disks. Considering planarization of DTR disks, they explained non-uniform lubricant distribution by differences in the intermolecular interactions between the lubricant and the materials in the land and groove areas. The surface energy of DTR media is affected by the thickness of the carbon overcoat and the lubricant layer. Changes in the carbon overcoat thickness or lubricant migration from the land to the groove area are of great tribological concern and need to be evaluated. Surface energy measurements in the groove and land area are important for the prediction of lubricant migration and can give information about carbon overcoat and lubricant characteristics.

7.2 Surface Energy Measurement on Nano-structures

Surface energy and intermolecular forces play an important role in the dynamics of micro- and nano-electromechanical systems (MEMS, NEMS) as, for example, in micro-accelerometers, digital micro-mirror devices, bio-mimetic, nano-imprinting and self-assembled monolayers and pattern media for data storage [**10**], [**11**], [**12**], [**13**]. The surfaces of many electromechanical systems are naturally or intentionally covered with thin liquid films, such as water from the humidity of the air or lubricants for wear and corrosion protection. Intermolecular forces can cause strong adhesion and friction and are increasingly more important for MEMS and NEMS applications [**12**], [**13**] as well as discrete track recording media [**7**].

The measurement of surface energy is generally performed by determining the contact angle of a small drop of liquid on a surface (contact angle measurement), and using Young's and Dupré's equations [14] to calculate the surface energy as described in Chapter 3. In the case of nano-machined surfaces, such as the nano-sized patterning on a magnetic hard disk, the contact angle is affected by the surface nano-structure. Droplets on the order of one micro-liter have a diameter of approximately 1mm and would cover thousands of elements of the nano-structure as shown in Figure 7.4. Thus, surface energy on features of nano-structured surfaces cannot be obtained correctly using conventional contact angle goniometry.

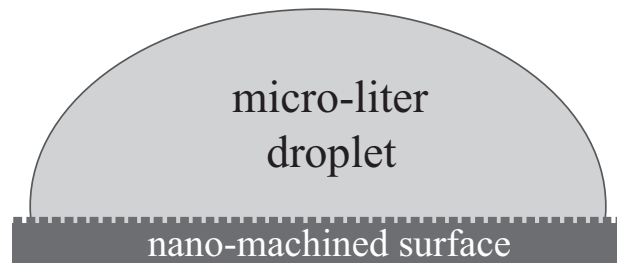
Figure 7.4: Droplet on a nano-machined surface covering multiple nano-structures.

Different techniques have been proposed in the literature to measure work of adhesion and/or surface energy on the micro- and nano-scale using atomic force microscopy (AFM), or equipment such as the surface force apparatus, the microtriboapparatus, or the cantilever beam array [15], [16]. Of all these techniques

the most commonly used one is the AFM pull-off force measurement method [**17**], [**18**], [**19**], [**20**], [**21**]. The derivation of surface energy from pull-off force measurements is usually based on contact mechanics adhesion models and has been described in the previous chapters.

A general equation of adhesion F as a function of surface energy γ for different adhesion models is

$$F = g\gamma \tag{7.1}$$

where g is the geometric factor [**14**]. Different forms of Eq. (7.1), where the geometric factor g can vary between $3\pi R$ and $4\pi R$, were proposed by Derjaguin, Muller and Toporov [**22**], Johnson, Kendall and Roberts [**23**] and by Maugis [**24**]. Equation (7.1) is valid only when the AFM tip and the sampled surface have identical surface energies. Otherwise, only the work of adhesion can be calculated. Large variations of up to 50% have been reported for the determination of surface energy from pull-off force measurements using Eq. (7.1) [**18**], [**20**].

To overcome this deficiency and ensure equal surface energy values, Beach et al. [**18**] coated both the AFM tip and the smooth silicon surface with gold and added a self-assembled monolayer of 1-Hexadecanethiol on top of it. They then measured the AFM tip radius and the cantilever stiffness, for which complex and difficult procedures are required. Finally, they calculated the surface energy using both the DMT and the JKR approximations. They compared their results with macroscopic contact angle measurements and found a good correlation with the DMT approximation. However, the JKR approximation resulted in an overestimation of

approximately 30%. In both cases, large variations in surface energy values reaching 20% of the mean value were encountered even when a large number of repetitions were made.

Zong et al. [20] determined the surface energy of gold contacts in micro-switch structures using AFM pull-off force measurements. Their AFM tip was also coated with gold for equal surface energies. The MD approximation was used to calculate the surface energy and large variations in surface energy reaching 25% of the mean value were observed during repeated measurements.

In order to calculate the surface energy from AFM pull-off force measurements using contact mechanics adhesion models, an accurate measurement of the cantilever stiffness and the AFM tip radius is essential. Noel et al. [21] used a very elaborate calibration method to determine the AFM cantilever stiffness and tip radius. They implemented a compensation of the AFM tip tilt in order to improve the accuracy of the pull-off force measurements. They calculated the surface energy from AFM pull-off force measurements using the DMT approximation. The sample surfaces were silicon wafers functionalized with two different polar end groups (OH and CH_3) resulting in different surface energies. The results were compared with surface energy values obtained from macroscopic contact angle measurements on similar functionalized silicon wafers. The AFM tip was coated with gold and then grafted with the same end-groups as those used for the silicon wafers to provide equal surface energies which allows the use of the DMT model. It was stated in Noel et al. [21] that very accurate AFM calibration methods and determination of the AFM tip radius are

necessary to minimize the error in surface energy values obtained from AFM pull-off force measurements.

From the above literature review, it becomes apparent that current methods of surface energy measurement on nano-structured surfaces that are based on contact mechanics adhesion models such as the JKR, DMT or MD model are not only complex but also likely to be inaccurate (see also Drelich et al. [19]). A simple, direct, and more accurate method is therefore highly desirable. It is the goal of this paper to present such a method, which avoids the complexity and inaccuracy involved in the calibration of the AFM cantilever stiffness and in determining the accurate dimensions of the AFM tip. Furthermore, the method described here circumvents the uncertainties related to the use of the JKR, DMT or MD approximations.

7.2.1 Variation of Surface Energy on Discrete Track Media

Variations in the carbon overcoat thickness or local changes in the material properties in the land and groove areas can affect the lubricant distribution and the value in surface energy. Discrete track recording media consists of three different regions – the land area, the sidewalls, and the bottom of the groove. Figure 7.5 shows a model and individual material layers such as lubricant, carbon overcoat, magnetic layer, and under layer. Clearly, different material properties or thickness differences of these layers will cause variations in lubricant thickness and surface energy of each region.
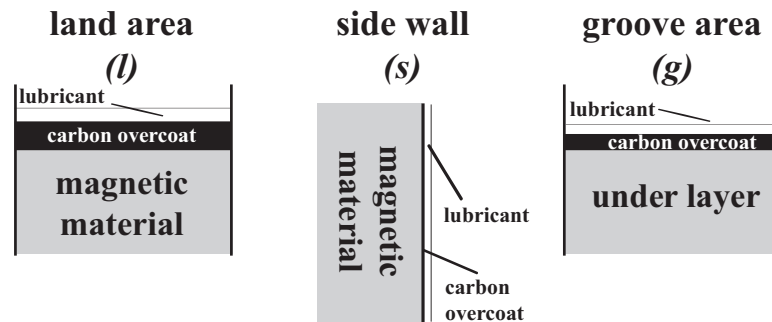
land area
(l)

side wall
(s)

groove area
(g)

lubricant

carbon overcoat

magnetic material

magnetic material

lubricant

carbon overcoat

lubricant

carbon overcoat

under layer

Figure 7.5: Materials differences between, land (*l*), sidewall (*s*), and groove area (g)

It is likely that the carbon film thickness is smaller at the bottom of the groove and the sidewalls than in the land area, due to non-uniform deposition of materials during the vapor deposition process. In particular, the deposition of carbon is directed normal to the surface of the DTR disk. However, deposition of carbon atoms occurs also at the side walls, reducing the number of carbon atoms deposited at the bottom of the grooves compared to the land area. Therefore, the thickness of the carbon overcoat at the bottom and the sidewalls of the grooves is likely to be smaller than the thickness of the carbon overcoat in the land area. A smaller carbon thickness would cause a change in surface energy in the groove area because of increased interactions with the under layer on which the carbon is deposited. It is justifiable to postulate that the Hamaker constant is different in the land area compared to that in the groove area. The land and the sidewall regions include the recording layer, while the under layer in the groove is the soft magnetic under layer. The latter materials together with the different carbon thickness can change the Hamaker constant for each individual area

and cause differences in lubricant film thickness which can cause higher surface energy in the groove area.

7.3   Theoretical Modeling

The spreading characteristics of thin lubricant films over DTR media are not fully understood. In the case of a pore in an otherwise smooth media, the lubricant thickness distribution at equilibrium can be obtained from the balance between the disjoining pressure in the flat region and the capillary pressure in the pore. Here, disjoining pressure represents the interaction energy per unit volume between molecules in a liquid film near a solid in comparison to the interaction energy experienced by the same molecules in a bulk liquid surface [25]. The disjoining pressure Π is given by [26]

$$\Pi = \frac{A}{6\pi h^3} \tag{7.2}$$

where A is the Hamaker constant for the material used, and h is the local lubricant film thickness. As can be seen from Eq. (7.2), the disjoining pressure increases rapidly with decreasing film thickness, resulting in a higher surface energy compared to that of the bulk liquid. The capillary pressure P in the pore is given by the Laplace equation

$$P = \frac{\gamma}{R} \tag{7.3}$$

where R is the local radius of curvature of the lubricant film in the pore and γ is the local surface energy.

In the case of DTR media, a groove is present instead of a cylindrical pore. The meniscus for a bulk amount of lubricant has a symmetrical shape along the side walls inside the groove as shown in Figure 7.6a). Fukuzawa et al. [27] used Eq. (7.3) to describe the surface radius of the meniscus formed by the bulk lubricant in the groove of a lubricated grooved solid surface. When the lubricant film is in equilibrium, the sum of the capillary pressure P and disjoining pressure Π must be constant at any arbitrary point x on the surface, i.e.

$$P(x) + \Pi[h(x)] = const. \tag{7.4}$$

where h(x) is the lubricant film thickness at point x. Therefore, at equilibrium when the pressure components of the land (l) and the groove (g) area are in equilibrium, one obtains

$$\underbrace{\frac{A_l}{6\pi h(x_l)^3} + \frac{\gamma}{R(x_l)}}_{\text{land area}} = \underbrace{\frac{A_g}{6\pi h(x_g)^3} + \frac{\gamma}{R(x_g)}}_{\text{groove area}} \tag{7.5}$$

The capillary pressure in the land area is negligible since $R(x_l)$ goes to infinity on a flat surface. On the other hand, the disjoining pressure of the lubricant in the groove can be neglected compared to the capillary pressure in the groove provided that $h(x_g)$ is large enough. In this case Eq. (7.5) can be simplified to

$$\frac{A_l}{6\pi h(x_l)^3} = \frac{\gamma}{R(x_g)} \tag{7.6}$$

where x_l and x_g denote horizontal distances in the land and groove area, respectively (see Figure 7.6).
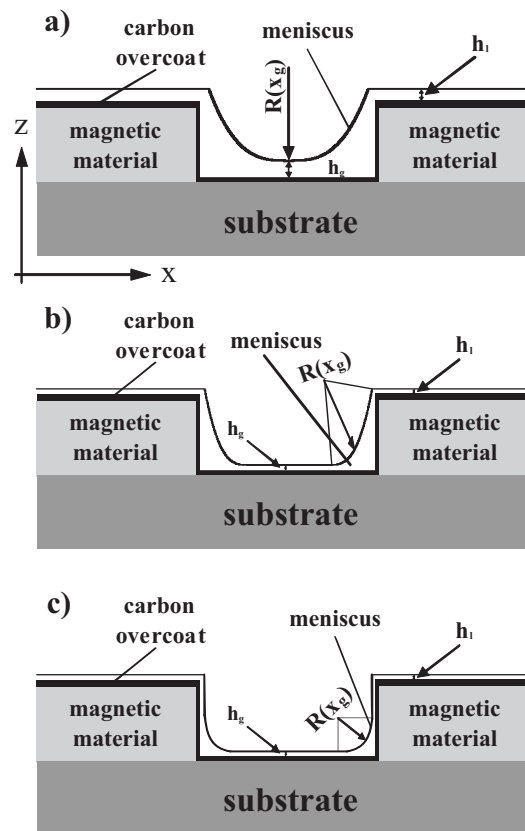

Figure 7.6: Meniscus formation in a groove. a) Lubricant thickness exceeds the diameter of gyration and forms one meniscus, b) less lubricant and formation of two menisci on each side wall with radius of curvature outside the groove, c) meniscus formation at the edges of the groove and side wall with radius of curvature inside the groove.

Fukuzawa et al. [27] discussed that Eq. (7.6) is applicable if the lubricant film thickness on the disk is greater than the diameter of gyration of the lubricant molecule. It is assumed that if the lubricant film thickness is smaller than the diameter of gyration, the profile of the lubricant shows a flat at the bottom of the groove as shown in Figure 7.6 b) and c) since the amount of lubricant available is not sufficient to form a meniscus.

Zhang et al. [28] proposed different models for the lubricant distribution on grooved surfaces based on the balance between disjoining pressure and capillary pressure. For the case that the lubricant film is uniform in the center of the groove and that the thickness of the film is less than the diameter of gyration of the lubricant, they proposed that two separate arcs of a meniscus would form inside the groove at the corners with the side walls (Figure 7.6b). The lubricant thickness in the center of the groove would be equal to that on the land area, if the land and groove have the same material characteristics. Depending on the amount of lubricant present, the center of curvature of the meniscus at each corner of the groove is either outside (Figure 7.6b) or inside the groove (Figure 7.6c). However, for a very thin lubricant film on DTR media it is unclear if a meniscus will form at the corners of the land, the side walls and the grooves.

The above models describe a situation where the land, the groove and the side walls consist of the same material. Fukuzawa et al. [9] modeled the lubricant on planarized DTR media filled with a dielectric material as a four-layered structure. They modified Eq. (7.2) to

$$\Pi[h] = \frac{A_1}{6\pi h^3} + \frac{A_2}{6\pi(h+T)^3} \tag{7.7}$$

where h and T are the thicknesses of the lubricant and the carbon overcoat, respectively; A_1 is the Hamaker constant for the interaction between the lubricant and the surface while A_2 is the Hamaker constant for the interactions between the lubricant and the carbon overcoat with the surface. Equating the disjoining pressure of the lubricant film in the land area with the planarized groove area (suffixes l and g) gives;

$$\underbrace{\frac{A_{1l}}{6\pi h_l^3} + \frac{A_{2l}}{6\pi(h_l + T_l)^3}}_{\text{land region}} = \underbrace{\frac{A_{1g}}{6\pi h_g^3} + \frac{A_{2g}}{6\pi(h_g + T_g)^3}}_{\text{groove region}} \tag{7.8}$$

Using Eq. (7.8), one is able to predict the thickness distribution of the lubricant on the planarized DTR media. The lubricant has different molecular interactions with the different surface materials in the groove and land region. Therefore, the lubricant thicknesses may differ in the two regions due to the required pressure balance.

For the case under investigation, a model is required to describe the lubricant film thickness in a non-planarized DTR media for which the material properties of the sidewalls, the land and the groove areas are different from each other (See: Figure 7.5). In equilibrium, a balance of disjoining and capillary pressure must exist for the land, the side walls and the groove areas. Thus, recalling the previously discussed lubricant distribution in grooved media, we can write the following expression for the three different areas

$$\underbrace{\underbrace{\frac{A_{1l}}{6\pi h_l^3} + \frac{A_{2l}}{6\pi(h_l + T_l)^3}}_{\text{disjoining pressure}} + \underbrace{\frac{\gamma}{R(x_l)}}_{\text{capillary pressure}}}_{\text{land region}}$$

$$= \underbrace{\frac{A_{1s}}{6\pi h_s^3} + \frac{A_{2s}}{6\pi(h_s + T_s)^3} + \frac{\gamma}{R(x_s)}}_{\text{side wall}} \tag{7.9}$$

$$= \underbrace{\frac{A_{1g}}{6\pi h_g^3} + \frac{A_{2g}}{6\pi(h_g + T_g)^3} + \frac{\gamma}{R(x_g)}}_{\text{groove area}}$$

where $A_{1\,l,s,g}$ and $A_{2\,l,s,g}$ are the Hamaker constants for a four-layered structure. Eq. (7.9) represents the most general case for the balance of disjoining and capillary pressure for each region. It indicates that because of possible variations of the Hamaker constant due to material differences as well as different carbon film thickness, variations in lubricant film thickness between the land, groove and side wall areas can occur. It is likely that the carbon overcoat and lubricant film are thinner in the groove area and, consequently, the surface energy there is larger compared to the land area.

7.4 Properties of the DTR Media

The discrete track recording (DTR) disks, obtained for this study, were manufactured by nano-imprint lithography as described previously. Several disks with groove depths of 33 nm, 40 nm, and 53 nm, respectively, were studied. Figure 7.7 shows a schematic of the dimensions of the discrete track recording media. In addition, the AFM tip is drawn to scale and has a tip-radius of approximately 15 nm.

The track pitch for all disks is approximately 380 nm and the land to groove ratio is approximately 2:1. An SEM image of a section of a typical discrete track recording medium is shown in Figure 7.8.
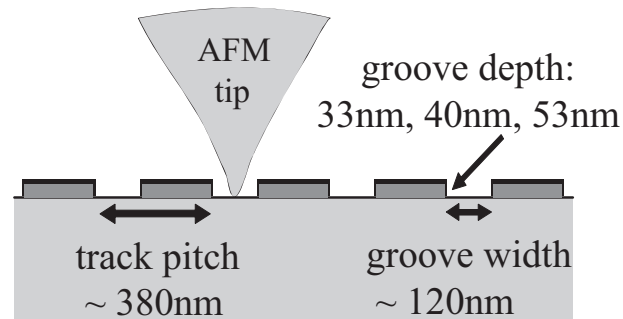

Figure 7.7: Dimensions of discrete track recording media. The AFM tip has a tip radius of approximately 15nm and is drawn to scale.
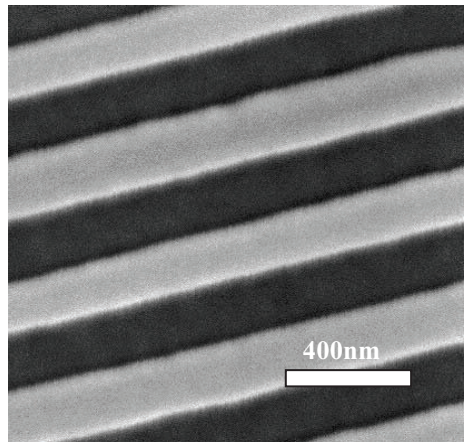

Figure 7.8: SEM image of DTR disk with 40nm groove depth and 380 nm track pitch. The dark part is the groove area and the bright part is the land area.

The DTR disks were coated with a thin carbon overcoat of approximately 3 nm thickness which was deposited on the disks after etching the discrete tracks into the magnetic film. At that carbon thickness, the underlying magnetic layer should have no effect on the surface energy measurement [29]. The DTR disks were dip-coated in Z-Dol lubricant solution at a fixed pull rate. It is not easy to measure the exact PFPE film thickness on the land or groove area of a DTR disk. Hence, it is commonly assumed that the lubricant thickness on DTR disks is comparable with that on smooth disks [28] at the same pull-rate and solvent solution. Using ellipsometry and accounting for light diffraction caused by the presence of the grooves, Zhang et al. [28] found that the average lubricant thickness for a grooved surface is equal to that of an equivalent smooth surface. However, their results show a non-uniform lubricant distribution on grooved surfaces at equilibrium. An average lubricant film thickness of approximately 1.2 nm was determined on "smooth" disks dip-coated under the same conditions and is assumed to be the same for the DTR disks. This film thickness is well below the monolayer thickness of approximately 2.5 nm for Z-Dol [30].

7.5 Surface Energy Measurement on Nano-structured Surfaces

The surface energy and pull-off force measurements on nano-structured surfaces were performed in the same way as described in Chapter 5. The relationship

between pull-off force in arbitrary units and the surface energy of the smooth gage disk surfaces observed in the previous chapter was used in this study. The range of the Z-Dol film thickness was chosen to be between 0.5 and 2.31 nm. This range was selected to avoid meniscus formation associated with thick films. Clearly, meniscus formation would complicate the calibration procedure by adding an unknown component to the pull-off force [31], [32], [33]. The force-distance curve in Figure 7.9 a) shows an actual measurement on a dip-coated smooth gage surface covered with a 1.3 nm thick film of Z-Dol. The AFM tip separates abruptly from the surface and no evidence of meniscus formation is observed. For comparison, Figure 7.9 b) shows a force-distance measurement obtained with the same AFM tip on a gage surface covered with a Z-Dol film thickness of approximately 10 nm. In this case, there is enough mobile lubricant available to form a meniscus, as can be seen from the delayed separation in the force-distance measurement during the pull-off period. This comparison proves that no meniscus is formed between the AFM tip and the surface in the range of film thicknesses used in this study.
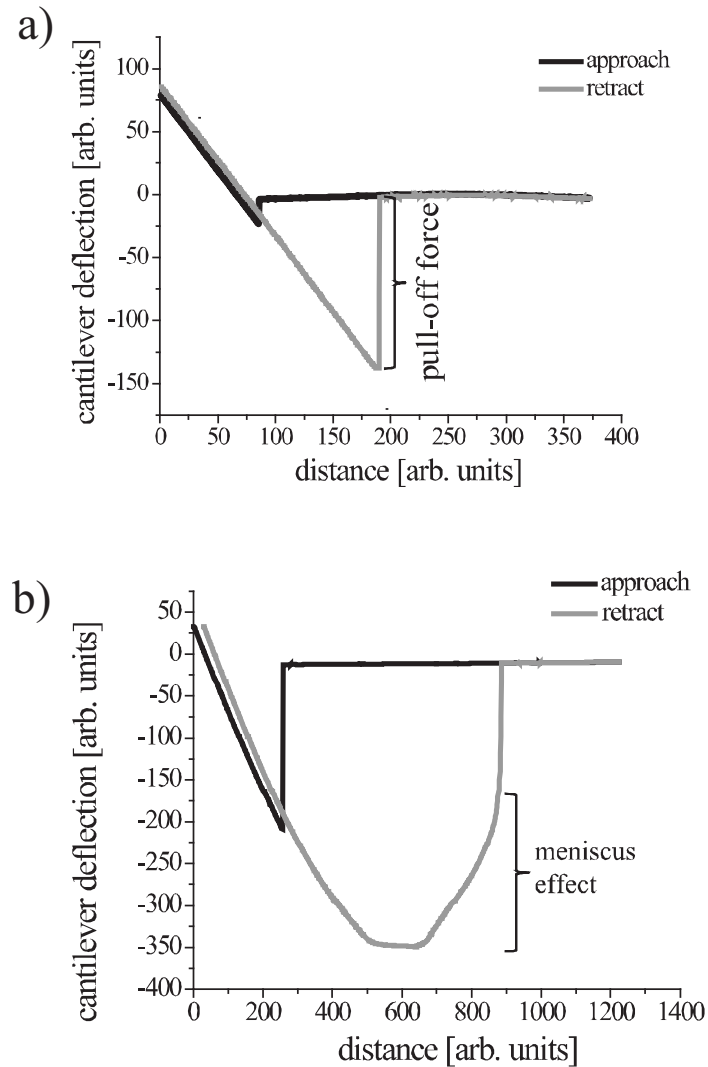
Figure 7.9: a) AFM force-distance measurement to determine AU pull-off force on a smooth dip-coated surface with a 1.3 nm thin Z-Dol film. b) AFM force-distance measurement for a Z-Dol film thickness of approximately 100nm, where a meniscus is formed.

Figure 7.10 shows the pull-off force in arbitrary units (AU) measured on the various dip-coated gage surfaces versus the film thickness of Z-Dol. Similar to the measurements in Chapter 6 of this dissertation, the pull-off force decreases with

increasing Z-Dol film thickness. The results shown in Figure 7.10 are the average of
at least four repetitions. The maximum variation from the mean (not shown in the
figure) was less than 10%.
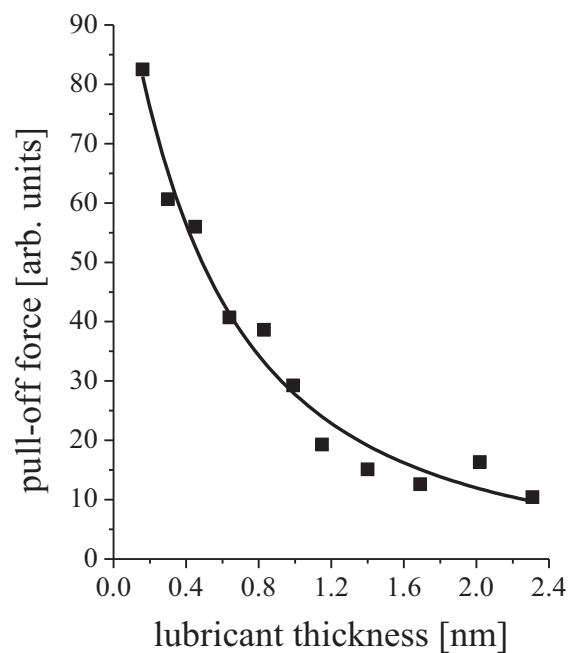
Figure 7.10: AU pull-off force as a function of lubricant film thickness on the smooth
dip-coated gage surfaces.

Figure 7.11 is a cross-plot to establish a direct relationship between the pull-off
force of the AFM tip and the surface energy of the dip-coated gage surfaces (similar to
the results from chapter 6). We observe that the pull-off force is linearly related to the
surface energy in the range of interest. The calibrated tip can now be used to measure

surface energy on nano-structured surfaces covered with the same Z-Dol lubricant. The same calibration method can be used whenever a different liquid is of interest. However, a new clean AFM tip is needed every time to avoid contamination.

Figure 7.11: Calibration curve of pull-off force in arbitrary units versus surface energy for an AFM tip.

After the measurement of the adhesion, the calibrated tip was used to determine the surface energy. Figure 7.12 shows the surface energy values of the land and groove areas of the discrete track recording media for three different groove depths. We observe that the surface energy values in the land area are between 20.3

and 22.4 mJ/m^2. In the groove area the surface energy is somewhat higher, between

30.8 and 34.5 mJ/m^2. The results shown in Figure 7.12 are the average of at least four

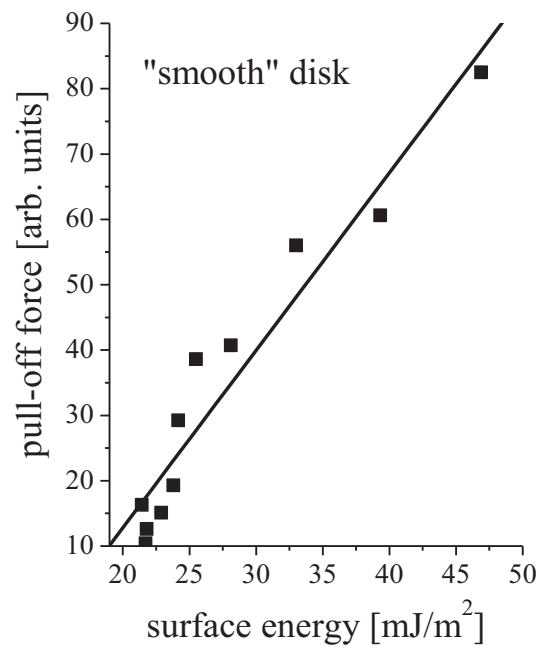repetitions. The maximum variation from the mean (not shown in the figure) was less
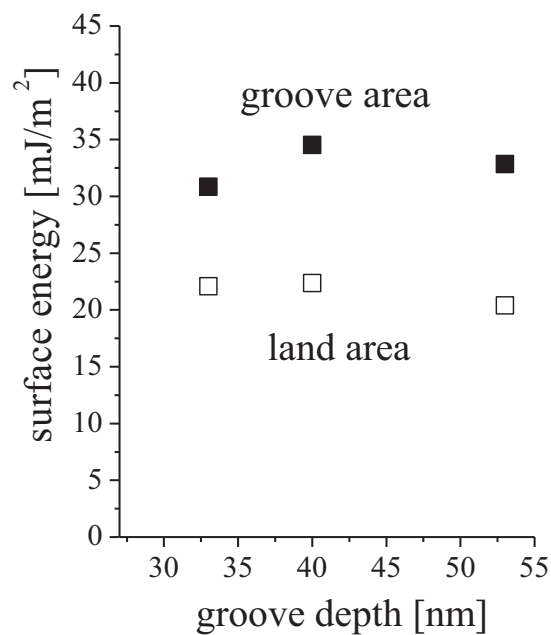
than 10%.

Figure 7.12: Surface energy of nano-machined, lubricated discrete track recording media with different groove depths.

From the results shown in Figure 7.12 one can observe that the surface energy

and, hence, the Z-Dol lubricant film thickness, on the land area remains nearly

constant regardless of the depth of the grooves. It seems that the lubricant strongly

adheres to the land area and does not migrate into the grooves in spite of the difference in surface energy between land and groove. This phenomenon can be explained with reference to Eq. (7.9). The disjoining pressure in the lubricant film on the land area, as well as the lubricant film thickness will be the same for the disks with the four different groove depths used in this study. This would result in the same surface energy value for the land areas of the disks regardless of groove depth.

In addition, one can predict that if lubricant gets displaced from the land area, the surface energy over that area will increase, therefore, disjoining pressure will move lubricant back into the depleted area until the sum of disjoining and capillary pressure for the land, the side-walls, and the groove areas are the same. The gradient in disjoining pressure creates a driving force inside the lubricant film, which moves lubricant from the area with larger lubricant thickness (lower disjoining pressure) to the area with smaller lubricant thickness (higher disjoining pressure) until it is balanced.

In [9] and [28] a non-uniform distribution of lubricant in discrete track recording media was predicted for the case that material differences are present in the land and groove areas. The present experimental results are in agreement with those predictions.

7.6 Conclusion

A simple AFM calibration method for direct measurement of surface energy on nano-structured surfaces covered with molecularly-thin liquid films was presented. This method eliminates the need for complex calibration of the cantilever spring constant or measurement of the AFM tip curvature to determine surface energy based on contact mechanics theoretical adhesion models such as the DMT or the JKR approximations.

The calibration of the AFM tip was accomplished by using pull-off force measurements on dip-coated gage surfaces with known surface energy. A calibration curve of the AFM tip showing a linear relationship between pull-off force and surface energy was obtained. This calibration curve was subsequently used for the evaluation of the surface energy on a nano-structured surface covered with the same molecularly-thin liquid film.

7.7 Acknowledgement

The dissertation author was the primary researcher and author and the co-authors listed in this publication directed and supervised the research which forms the basis for this chapter.

Bibliography

[1] X.-M. Yang, Y. Xu, C. Seiler, L. Wan, and S. Xiao, "Toward 1 Tdot/in.2 nanoimprint lithography for magnetic bit-patterned media: Opportunities and challenges," *J. Vac. Sci. Technol. B*, vol. 26, no. 6, pp. 2604-2610, 2008.

[2] D. Wachenschwanz et al., "Design of manufacturable discrete track recording medium," *IEEE Trans. Mag.*, vol. 41, no. 2, pp. 670-675, 2005.

[3] Y. Soeno et al., "Feasibility of discrete track perpendicular media for high track density recording," *IEEE Trans. Magn.*, vol. 39, no. 1, pp. 1967-1971, 2003.

[4] B.D. Terris and T. Thomson, "Nanofabricated and self-assembled magnetic structures as data storage media," *J. Phys. D: Appl. Phys.*, vol. 38, pp. R199-R222, 2005.

[5] B.D. Terris, T. Thomson, and G. Hu, "Patterned media for future magnetic recording data storage," *Microsyst. Technol.*, vol. 13, pp. 189-196, 2007.

[6] K. Hattori, K. Ito, Y. Soeno, M. Takai, and M. Matsuzaki, "Fabrication of discrete track perpendicular media for high recording density," *IEEE Trans. Magn.*, vol. 40, no. 4, pp. 2510-2515, 2004.

[7] S. Suzuki, P. Dorsey, and M. Duwensee, "Discrete track recording media and its tribological challenges in head/disk interface," *J. Jap. Soc. of Trib.*, vol. 52, no. 6, pp. 406-411, 2007.

[8] M. Duwensee, S. Suzuki, J. Lin, D. Wachenschwanz, and F.E. Talke, "Simulation of the head disk interface for discrete track media," *Microsyst. Technol.*, vol. 13, pp. 1023-1030, 2007.

[9] K. Fukuzawa, T. Muramatsu, H. Amakawa, S. Itoh, and H. Zhang, "Nonuniform distribution of molecularly thin lubricant caused by inhomogeneous buried layers of discrete track media," *IEEE Trans. Magn.*, p. in print, 2008.

[10] B. Bhushan, "Nanotribology and nanomechanics in nano/biotechnology," *Phil. Trans. R. Soc. A*, vol. 366, pp. 1499-1537, 2008.

[11] B. Bhushan, "Nanotribology and nanomechanics of MEMS/NEMS and BioMEMS/BioNEMS materials and devices," *Microelectronic Engineering*, vol. 84, pp. 387-412, 2007.

[12] N.S. Tambe and B. Bhushan, "Scale dependence of micro/nano-friction and adhesion of MEMS/NEMS materials, coatings and lubricants," *Nanotech.*, vol. 15, pp. 1561-1570, 2004.

[13] Y.-P. Zhao, L.S. Wang, and T.X. Yu, "Mechanics of adhesion in MEMS - a review," *J. Adhesion Sci. Tech.*, vol. 17, no. 4, pp. 519-546, 2003.

[14] J.N. Israelchvili, *Intermolecular and surface forces, 2nd edition*. London: Academic Press, 1991.

[15] M.P. de Boer and T.A. Michalske, "Accurate method for determining adhesion of cantilever beams," *J. Appl. Phys.*, vol. 86, no. 2, pp. 817-827, 1999.

[16] B. Bhushan, "Adhesion and stiction: Mechanism, measurement techniques and method for reduction," *J. Vac. Sci. Tech. B*, vol. 21, no. 6, pp. 2262-2296, 2003.

[17] A. El Ghzaoui, "Determination of surface energyof polymers by force microscopy," *Appl. Phys.*, vol. 85, pp. 1231-1233, 1999.

[18] E.R. Beach, G.W. Tormoen, and J. Drelich, "Pull-off force measured between hexadecanethiol self-assembled monolayers in air using an atomic force microscope: Analysis of surface free energy," *J. Adh. Sci. Tech.*, vol. 16, no. 7, pp. 845-868, 2002.

[19] J. Drelich, J. Tormoen, and E.R. Beach, "Determination of solid surface tension from particle-substrate pull-off forces measured with the atomic force microscope," *J. Colloid Interf. Sci.*, vol. 280, pp. 484-497, 2004.

[20] Z. Zong, Y. Cao, N. Rahbar, and W. Soboyejo, "Nano- and microscale adhesion energy measurement for Au-Au contacts in microswitch structures," *J. Appl. Phys.*, vol. 100, no. 10, p. 104313, 2006.

[21] O. Noel, H. Awada, G. Castelein, M. Brogly, and J. Schultz, "Force curve measurements with the AFM: Application to the in situ determination of grafted silicon-wafer surface energies," *The Journal of Adhesion*, vol. 82, pp. 649-669, 2006.

[22] B.V. Derjaguin, V.M. Muller, and Y.P. Toporov, "Effectof contact deformations on adhesion of particles," *J. Colloid. Interf. Sci.*, vol. 53, pp. 314-326, 1975.

[23] K.L. Johnson, K. Kendall, and A.D. Roberts, "Surface energy and contact of elastic solids," *Proc. Roy. Soc. London Ser. A*, vol. 324, p. 301, 1971.

[24] D. Maugis, "Adhesion of spheres - The JKR-DMT transition using a dugale model," *J. Colloid Interf. Sci.*, vol. 150, pp. 243-269, 1992.

[25] C.M. Mate, "Application of disjoining and capillary pressure to liquid lubricant films in magnetic recording," *J. Appl. Phys.*, vol. 72, pp. 3084-3090, 1992.

[26] C.M. Mate and J. Novotny, "Molecular conformation and disjoining pressure of polymeric liquid films," *J. Chem. Phys.*, vol. 94, pp. 8420-8427, 1991.

[27] K. Fukuzawa, J. Kawamura, T. Deguchi, H. Zhang, and Y. Mitsuya, "Disjoining pressure measurements using a microfabricated groove for a molecularly thin polymer liquid film on a solid surface," *J. Chem. Phys.*, vol. 121, no. 9, pp. 4358-4363, 2004.

[28] H. Zhang, Y. Mitsuya, M. Yamada, and K. Fukuzawa, "Measurement of spreading characteristics of molecularly thin lubricant films over grooved solid surfaces based on diffraction simulations," *Microsyst. Technol. 13, 895-904 (2007)*, vol. 13, pp. 895-904, 2007.

[29] R.J. Waltman et al., "The effect of carbon overcoat thickness on the Zdol boundary lubricant film," *Trib. Lett.*, vol. 12, no. 1, pp. 51-60, 2002.

[30] R.J. Waltman, A. Khurshudov, and G.W. Tyndall, "Autophobic dewetting of perfluoropolyether films on amorphous-nitrogenated carbon surfaces," *Trib. Lett.*, vol. 12, no. 3, pp. 163-169, 2002.

[31] F.W. DelRio, M.L. Dunn, and M.P. de Boer, "Capillary adhesion model for contacting micromachined surfaces," *Scripta Materialia*, vol. 59, pp. 916-920, 2008.

[32] M. Ruths and S. Granick, "Rate-dependent adhesion between opposed perfluoropoly(alkyether) layers: Dependence on chain-end functionality and chain length," *J. Phys. Chem. B*, vol. 102, pp. 6056-6063, 1998.

[33] H.m. Stanley, I. Etsion, and D.B. Bogy, "Adhesion of contacting rough surfaces in the presence of sub-boundary lubrication," *J. Trib. Trans. ASME*, vol. 112, pp. 98-104, 1990.

8   Summary and Conclusions

Surface energy and molecular forces in the head/disk interface are important for achieving stable flying height at distances below 5 nm. In this dissertation the properties of the carbon overcoat and the perfluoropolyether lubricant were investigated and their correlation to surface energy and intermolecular forces was analyzed.

Different methods of depositing carbon on the magnetic disk and the compositional analysis of the film were described. Raman spectroscopy and X-ray photoelectron spectroscopy were used to determine the composition and amorphitization stage of the film, respectively. Topographical and mechanical properties were determined using atomic force microscopy and nano-scratch tests for different overcoats on various disks and sliders.

Perfluoropolyether lubricant films and additives used for wear protection play a key role in the head/disk interface. Their spreading properties have been analyzed by placing micro-droplets of different PFPE lubricants on a carbon-coated disk surface. An empirical expression for the spreading as a function of time is presented. Using the principle of minimum energy and volume conservation, a model for determining the average film thickness as a function of the initial surface energies of the liquid and the smooth, solid surface was provided. In addition, the model shows that in order for the lubricant to spread, the surface energy of the smooth, solid surface

has to be twice of that of the liquid. The model holds for both dispersive and polar liquids.

A modification of the relationship between surface energy and adhesion as well as friction was presented in Chapter 6. The surface energy of carbon coated hard disks can be varied by either altering the total PFPE film thickness or the bonding ratio of the PFPE film onto the surface. Using atomic force microscopy pull-off force measurements, it was found that the adhesion vanishes at non-zero values of surface energy. It was shown that only the excess surface energy $\Delta\gamma(h)$ of the lubricant film above the bulk value γ_{bulk} dictates the work of adhesion as well as the friction of two surfaces separated by a molecularly-thin PFPE films.

A simple AFM calibration in terms of surface energy can be established using a set of disks with molecularly-thin PFPE films at various thicknesses. The cantilever deflection (in arbitrary units) was measured on this set of smooth disks. This gives a calibration curve for the AFM cantilever as a function of surface energy. This method to determine surface energy is not based on contact mechanics models (DMT or JKR). The complex measurement of the AFM tip curvature and calibration of the cantilever spring constant is omitted by this procedure.

The calibrated tip was then used to determine the surface energy on nano-structured discrete track recording media. The results show that there are variations in surface energy between the land and the groove area of the discrete tracks. This

difference in surface energy may be caused by different carbon overcoat thickness or lubricant thickness variations.

This dissertation summarizes the interaction between the carbon overcoat and lubricant used in modern hard disk drives and their influence on intermolecular forces. In addition, it shows a simple method to determine surface energy on the nano-scale which has been a challenge for nano-structured surfaces.

Appendix A

The constants C and d in Eq. (5.7) can be determined from surface energy measurements as a function of film thickness as described in [1]. The final film thickness of Z-Dol 2000 and Z2290 is on the order of one molecular layer and in this range the total surface energy is declining exponentially [2], [3].

The results for the total surface energy, $\gamma_l^{total} = \gamma_l^d + \gamma_l^p$, of the Z-Dol wetted smooth solid surfaces are shown in Figure A1. The total surface energy decreases with increasing film thickness and approaches the surface energy of the bulk Z-Dol γ_{li} which is approximately 17 mJ/m². The total surface energy was fitted using Eq. (5.7). The values of the constants $C = 1.5 \cdot 10^{-20} J$ and $d = 0.55 nm$ were found from the best fit with $\gamma_{li} = 17 mJ/m^2$.
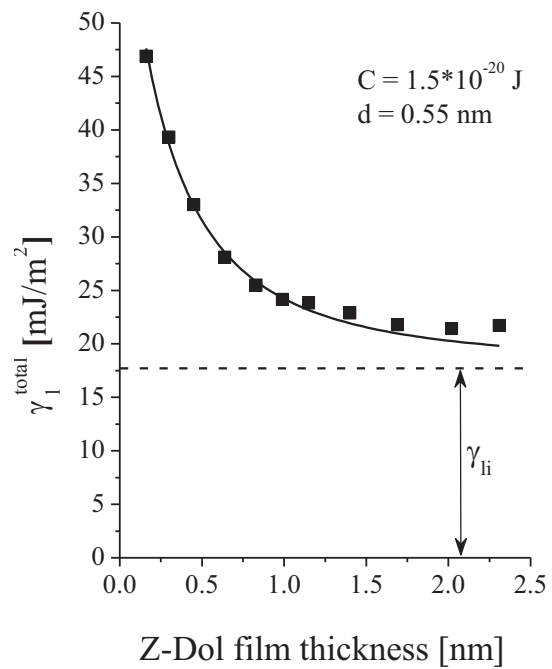
Figure A1: Total surface energy γ_l^{total} as a function of Z-Dol film thickness.

Bibliography

[1] R. Brunner, I. Etsion, and F.E. Talke, "A simple atomic force microscopy calibration method for direct measurement of surface energy on nanostructured surfaces covered with molecularly thin liquid films ," *Rev. Sci. Instrum.*, vol. 80, no. 5, p. 055109, 2009.

[2] R.J. Waltman, A. Khurshudov, and G.W. Tyndall, "Autophobic Dewetting of Perfluoropolyether Films on Amorphous-nitrogenated Carbon Surfaces," *Trib. Lett.*, vol. 12, no. 3, pp. 163-169, 2002.

[3] G.W. Tyndall, P.B. Leezenberg, R.J. Waltman, and J. Castenada, "Interfacial interactions of perfluoropolyether lubricants with magnetic recording media," *Trib. Lett.*, vol. 4, pp. 103-108, 1998.